TECHNISCHE
UNIVERSITÄT
WIEN

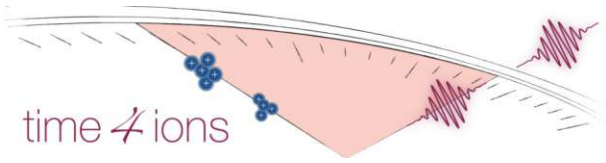

DIPLOMARBEIT

Erosion of metallic nano-islands with slow highly charged ions and investigation of swift heavy ion tracks

zur Erlangung des akademischen Grades

Diplom-Ingenieur

im Rahmen des Studiums

Technische Physik

eingereicht von

Helmut Muckenhuber

Matrikelnummer: 01326615

Ausgeführt am Institut für Angewandte Physik an
der Technischen Universität Wien

unter der Anleitung von

Assistant Prof. Dr.rer.nat. Richard A. Wilhelm,
Projektass. Dipl.-Ing. Gabriel L. Szabo

October 20, 2022

Helmut Muckenhuber

Richard A. Wilhelm

Abstract

Nowadays the use of ions is a common method to alter semiconductors or insulators on the nanometer scale. This can range from the creation of nano-hillocks and craters on the surface to melting of these materials. These effects can be triggered by either the kinetic energy or the potential energy of an ion in the case of insulating and semiconducting targets. For metallic targets, kinetic effects were measured, but potential energy effects were not observed until now, because free electrons in the conduction dissipate the energy fast enough to prevent permanent material damage. We performed irradiations of gold (Au) nano-islands on a molybdenum disulfide (MoS_2) monolayer with highly charged ions (HCIs) and found that erosion of metallic targets is possible, if they are produced on the nanometer scale. This erosion manifests itself in height loss of these Au nano-islands and was therefore measured with an atomic force microscope (AFM). Furthermore, we found a charge-state dependent height loss, where the Au nano-islands decreased more in their height with increasing charge state. Additionally, a one-to-one measurement was performed, where the same Au nano-islands were compared before and after irradiation. In this way, a volume threshold was found, where these Au nano-islands seem to be more effected by the potential energy in terms of height loss.

HCIs were also used to alter bismuth nano-clusters on calcium fluoride (CaF_2) and silicon dioxide (SiO_2), but the measured height loss was too small to be attributed to the potential energy of the HCI, because the nano-clusters were produced too dense.

The second part was the investigation of swift heavy ions (SHIs) in insulating materials, such as titanium dioxide (TiO_2) and aluminium oxide (Al_2O_3). A SHI impinging an insulating or semiconducting target creates an energy density spike in the electronic system, which results in a trail of damage. This latent track consists of two parts, namely a conical damage profile and a discontinuous part, where amorphisation occurs. Transmission electron microscopy (TEM) was used to visualise these parts of the latent track. Although it was able to resolve the conical damage profile with different (TEM-) techniques, the discontinuous part could not be resolved. Furthermore, a TEM analysis showed, that these conical damage profiles are empty or voids.

Kurzfassung

Heutzutage werden Ionen verwendet, um Halbleiter und Isolatoren auf der Nanometerskala zu verändern. Dies umfasst die Erschaffung von Nano-hillocks, Kratern und gezieltes Aufschmelzen dieser Materialien. Diese Effekte können entweder durch die kinetische oder potentielle Energie des Ions ausgelöst werden, wenn es sich um einen Isolator oder Halbleiter handelt. Bei Metallen wurden zwar Effekte der kinetischen Energie gemessen, aber potentielle Energieeffekte wurden bis jetzt nicht beobachtet, da Metalle die gewonnene potentielle Energie über freie Elektronen im Leitungsband schnell genug dissipieren um permanenten Schaden zu hinterlassen. Wir haben Gold Nanoinseln auf einer Molybdändisulfid Monolage mit hochgeladenen Ionen bestrahlt und haben die Erosion von diesen Nanoinseln beobachtet, wenn diese auf einer Nanometerskala gefertigt werden. Die Erosion der Gold Nanoinseln äußert sich in einem Höhenverlust und wurde daher mit einem Rasterkraftmikroskop vermessen. Außerdem wurde eine ladungszustandsabhängiger Höhenverlust gefunden, wo Nanoinseln mehr an Höhe verlieren, wenn der anfängliche Ladungszustand des Ions steigt. Zusätzlich konnte durch eine Eins-zu-eins-Auswertung ein Schwellwert für das Volumen gefunden werden, unter dem die Gold Nanoinseln durch die potentielle Energie stärker beeinflusst sind im Hinblick auf Höhenverlust.

Hochgeladene Ionen wurden auch verwendet, um Bismuth Nano-cluster auf Isolatoren wie Kalziumfluorid und Siliziumoxid zu bestrahlen. Der gefundene Höhenverlust war aber zu gering um dies auf die potentielle Energie des Ions zurückzuführen, da die Nano-cluster zu dicht auf dem Substrat deponiert wurden.

Der zweite Teil dieser Arbeit war die Untersuchung von latenten Spuren in Isolatoren wie Titandioxid und Aluminiumoxid, die durch die Bestrahlung mit schnellen, schweren Ionen ausgelöst wurden. Diese Art von Ionen führt in Isolatoren oder Halbleitern zu Energiespitzen im elektronischen System, welche dann zu einer Spur aus Schaden am Material führt. Diese latente Spur besteht aus zwei Teilen, dem konischen Schadensprofil und einem diskontinuierlichem Teil, wo eine Amorphisierung des Materials auftritt. Ein Transmissionselektronenmikroskop wurde verwendet, um diese latenten Spuren aufzulösen. Mit diesen Techniken war es möglich das konische Schadensprofil aufzulösen, aber der diskontinuierliche Teil blieb verborgen. Desweiteren zeigte eine Analyse, dass diese konischen Schadensprofile leer sind, wo kein Material zurückblieb.

Contents

1 State of the art and perspectives

Ion-solid interaction is a main field of today's research and much effort has been put into it, to understand the mechanisms when ions interact with solids. The applications of ions traverse doping of semiconductors [1], medical treatment for cancer patients [2], nano lithography [3], ion milling machines for sample preparation [4] just to name a few examples. The mentioned applications focus mainly on the kinetic energy of the impinging ion in insulating, semiconducting and metallic targets. In contrast to the kinetic energy, an ion can carry a large amount of potential energy, when many electrons are removed and is then called a highly charged ion (HCI). Potential energy effects of HCIs were found to induce permanent surface damage in insulating and semiconducting materials [5, 6]. However, in metals these surface modifications by the potential energy were not observed up to now. The motivation behind this research topic will be discussed in the following subsection.
Besides HCIs, swift heavy ions (SHIs) are used for inducing permanent damage in insulating and semiconducting materials, too [7, 8]. SHIs are characterised by a high kinetic energy and high mass. The interplay between charge state and kinetic energy loss is not considered in model descriptions. In this thesis I want to investigate the possible influence of the charge state on permanent damage in insulators.

1.1 Motivation

HCIs were found to alter insulating and semiconducting materials. The high potential energy, brought into the target's system, creates nano-hillocks, craters and melting. In the case of metals, potential energy effects on material erosion have not been observed up to now and only kinetic energy effects were observed [9–11]. When the potential energy of a HCI gets transferred to the electronic system of a metallic target, the large amount of free charge carriers in the conduction band dissipate the gained energy before any coupling to the lattice occurs. Therefore, the idea was to produce small metallic targets, which „store“ the gained energy long enough to trigger lattice atom movement and subsequently permanent material damage. In this work, a geometric confinement was realised experimentally, where the metallic gold (Au) nano-islands have a small volume of a few hundred to about 5000 nm^3.

Additionally, the kinetic energy of the HCI gets transferred to the lattice via elastic ion-nuclei scattering and results in heating and sputtering. Due to the combination of potential energy and kinetic energy effects and the cross-correlation between these, the nano-islands shall be eroded and a reduction in height will be measured with an atomic force microscope (AFM) in order to clearly show potential energy driven nano-engineering of metallic materials and to support existing model descriptions.

The irradiation of insulating and semiconducting materials with SHI leaves damage trails behind, where the track consists of two parts, namely the conical damage profile and a discontinuous tail along which amorphisation occurs. The goal was to visualise the discontinuous part of the track, where it either may recrystallise or leave some damage behind, eg. vacancies, defects, amorphous structure etc [12]. This part can reach micrometers deep into the target, according to simulations with TRIM [13] and can be seen in figure 1.1 (a). In figure 1.1 (b) the energy to recoils is shown and they gain the most energy at the end of the trajectory. Since the SHI is not in it's equilibrium charge state, the low initial charge state increases, because the ion strips off more electrons at high velocities when impinging the target [14]. This enhances the electronic stopping power when penetrating the target's surface. In this way, a threshold for the stopping power may be found, where no track occurs, but the charge state of the SHI enhances the stopping power up to a point where a latent track is created.

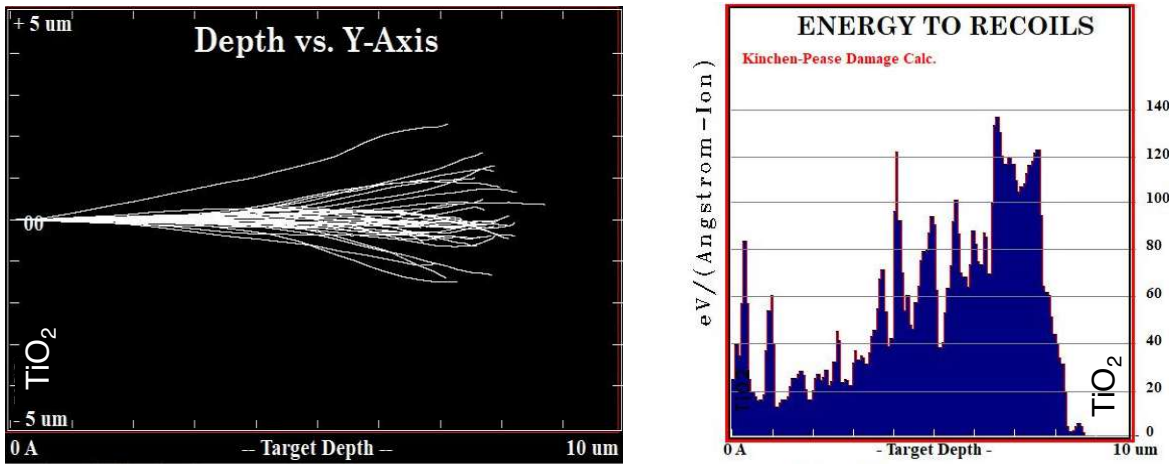

(a) (b)

Figure 1.1: In (a) the trajectories of 23 MeV I in TiO_2 is shown. The mean projected range is 7.5 µm and the mean lateral straggle is 542 nm. In (b) the energy transferred to the recoils is shown. This simulation was obtained with TRIM [13].

1.2 Ion-solid interaction

The ion-solid interaction undergoes many processes that occur on different time scales during the interaction [15]. The slowing down process of the ion is characterised by the stopping power S, which is the transferred energy from the ion to the target per path length dx of the ion's trajectory when passing through the target

$$S = -\frac{dE}{dx}. \tag{1.1}$$

The stopping power splits up into two different physical contributions, namely the nuclear stopping S_n and the electronic stopping S_e

$$S = -\frac{dE}{dx} = S_n + S_e. \tag{1.2}$$

The stopping power for xenon ions on gold (Au) is visible in figure 1.2. The energy transfer starts with the energy deposition from the ion to the target electrons on a timescale of 10^{-17} to 10^{-15} seconds followed by electron cascades. This is the regime of electronic stopping. This interaction includes the coulomb interaction between the ion and the target's electrons via inelastic collisions, that e.g. excites and ionises the target's electrons, forms electron-hole pairs and generates plasmons. [5].

Due to the interaction of the impinging ion with the electrons of the target atoms, the deflection of the ion is negligible and the trajectory maintains a forward movement [16]. The electronic stopping slows down the ion, which corresponds to a loss of energy, until it reaches the next regime, namely the nuclear stopping regime.

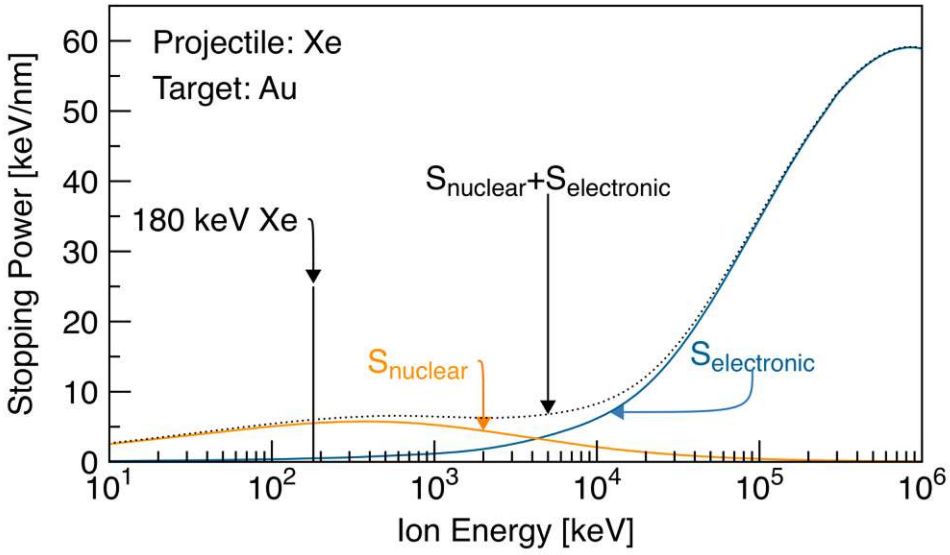

Figure 1.2: The stopping power simulated with SRIM [17]. The simulation only contains kinetic energy effects contributing to the stopping power. Multiple charge states were not considered.

At about 10^{-13} to 10^{-11} seconds the energy transfer from the excited electronic system to the lattice sets is, which includes electron-phonon coupling. The subsequent part are lattice processes, like the cooling of the thermal spike induced by the ions energy transfer. In contrast to electronic stopping, nuclear stopping is the direct energy transfer from the impinging ion to the nuclei of the target's atoms via collision cascades. This excites lattice vibrations (phonons) and is the main cause for displacements, local heating/melting, sputtering and structural modifications [18]. An overview of the mechanisms and timescales of the ion-solid interaction is given in figure 1.3.

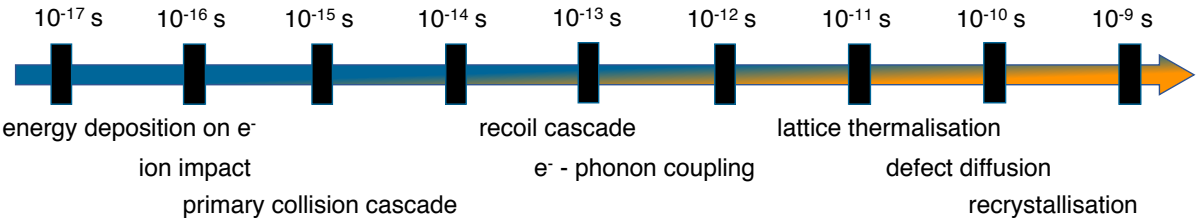

Figure 1.3: The different time scales of the energy deposition. Starting from the left with the excitation of the target electrons, which then couple to the lattice via electron-phonon coupling and creating a thermal spike/heating of the lattice.

The processes described above focus mainly on the effect of the kinetic energy of the ion, but in addition the potential energy can cause structural modifications too [5–7, 19, 20].

In our experiments, the incident ion is not in it's equilibrium charge state, it catches and strips off electrons until it's charge state gets stabilized. A first approach to calculate the effective charge of an ion is given by Bohr's formula [7]:

$$Z_{eff} = \frac{v}{v_0} \cdot Z^{1/3} \tag{1.3}$$

with v the velocity of the impinging ion, v_0 Bohr's velocity, which amounts to $2.19 \cdot 10^6 \frac{m}{s}$ and Z the atomic number of the impinging ion. The difference between the initial charge state and the equilibrium charge state can enhance the stopping power [21]. The differences of the potential energy effects for HCIs and SHIs are discussed in the chapters below.

1.3 Slow highly charged ions

Besides the kinetic energy of an ion, the potential energy needs to be considered for altering materials. The potential energy is given by the number of missing electrons q, in the electronic shell of an ion and can amount up to several hundred keV in modern research facilities such as HITRAP [22]. If many of these electrons are missing, the ion is called a highly charged ion (HCI) and the term „slow“ refers to a velocity of the ion smaller than the bohr's velocity in equation (1.3). In figure 1.4 the potential energy of a xenon ion can be seen as function of the potential energy.

Slow HCIs typically have low kinetic energy or velocity, so that the electronic stopping is suppressed compared to the nuclear stopping regime and electronic excitation processes of the target via the potential energy are dominant. Furthermore, the penetration depth is limited by the low kinetic energy and hence, surface interactions via the potential energy are dominant. A scheme of the interaction and the subsequent processes is shown in figure 1.5. The potential energy of the HCI gets transferred into the electronic subsystem of the target and dissipates there. Although the interaction starts above the surface [23], the total potential energy gets deposited in the first 1-3 layers of the target [24]. If the target is an insulator or semiconductor, the lack of free electrons causes the gained energy to dissipate in the lattice via electron-phonon coupling. This results in local heating and melting, if the heat of fusion threshold of the target is exceeded. Subsequently, so-called nano-hillocks or craters (pits) are formed on top of the surface or below it, respectively when the material cools down [25].

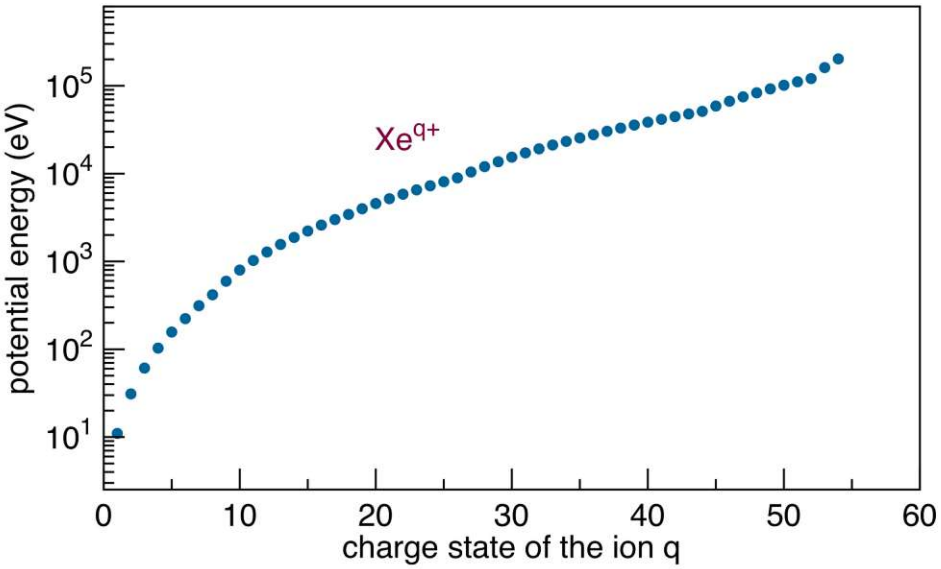

Figure 1.4: The potential energy in dependence of the charge state q. The potential energy can exceed the kinetic energy for slow HCI and can amount up to about 200 keV, which corresponds to a fully ionised xenon atom with q = 54.

1.4 Swift heavy ions

In contrast to slow HCIs, swift heavy ions (SHI) have a high kinetic energy in the order of MeV or GeV and thus, mainly electronic stopping is dominant for the deceleration of the SHI. Nuclear stopping becomes more significant at the end of the SHI's trajectory, when the kinetic energy is in the range of keV, because the (nuclear) stopping cross section (σ_n) increases there ($\sigma_n \propto \frac{1}{E^2}$). For insulators and semiconductors, the excitation of the electronic system can also induce features, like nano-hillocks on top of the surface and latent tracks below the surface.

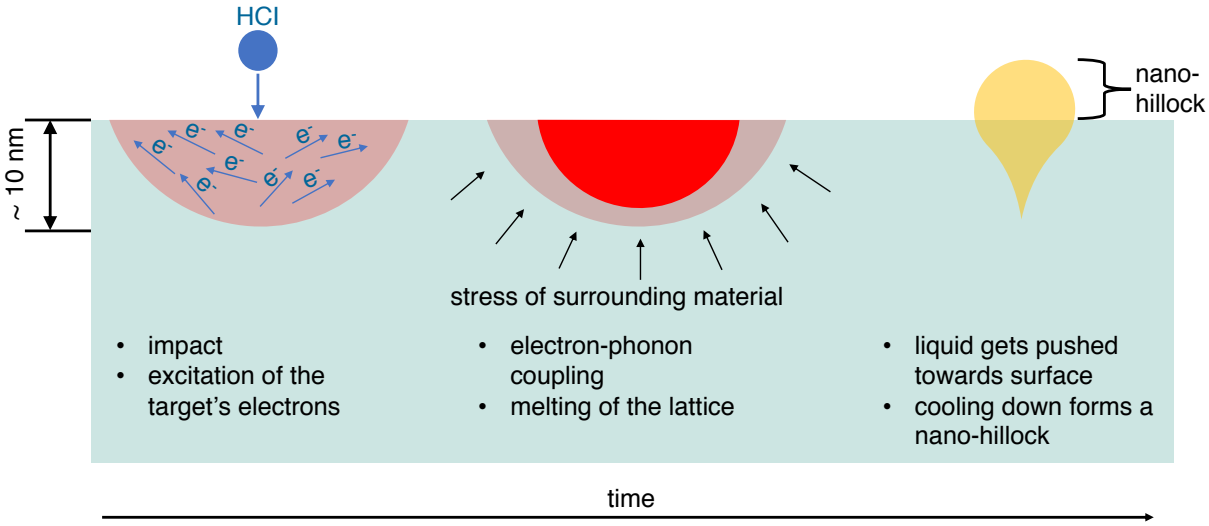

Figure 1.5: A scheme of the interaction process of a HCI impinging an insulator or semiconductor. The three main stages of this interaction include approaching the surface, excitation processes and melting/cooling down.

Since insulators and semiconductors do not have free electrons, compared to metals, the energy dissipates from the electronic system to the lattice, where these features are generated via electron-phonon coupling and local heating. This process can be described with different models. In this work the inelastic thermal spike model (i-TS model) will be discussed, since it is a promising model to describe track formation of a SHI [26]. Further information about other models like Coulomb explosion, the Bond Weakening model or the Exciton self-trapping model can be found in [15].

A scheme of the energy transfer progress is given in figure 1.6. First, the impinging ion transfers it's energy to the electronic system of the target atoms. Then the excited electronic subsystem couples to the lattice, or atomic subsystems, via electron-phonon coupling. The generated phonons heat up the area around the ion's trajectory, resulting in a phase shift from solid to liquid when the deposited energy exceeds the heat of fusion. The trajectory and impact area is mainly cylindrical and melting occurs on a straight line due to the collision, or interaction, of the SHI with the electrons of the target [7]. The stress of the surrounding material pushes the liquid towards the surface, where it cools down and forms a nano-hillock. Beneath the nano-hillock a „latent track“ can be observed, that represents the damage done to the target. This area has a conical shape due to the absence of the molten liquid that gets pushed across the surface and leaves mainly empty space behind, that will be shown and discussed in chapter 3.

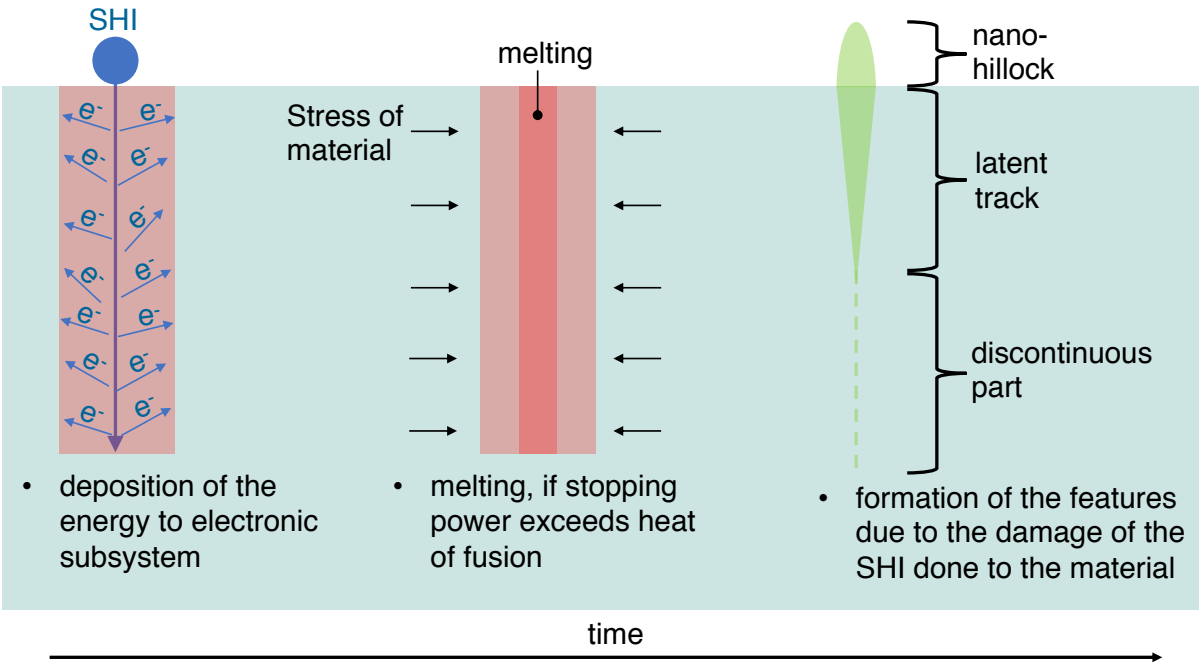

Figure 1.6: A scheme of the process of an SHI interacting with a solid. The energy transfer starts with the excitation of the electronic subsystem to the lattice, where finally melting occurs and features are generated when cooled down.

2 Experimental Setup

Since potential energy effects of HCIs may alter the height of the metallic nano-islands, an observation with atomic force microscopy (AFM) is of essence. Additionally, scanning electron microscope (SEM) measurements were accomplished to investigate changes in the lateral elongation. To observe such small features as latent tracks made from SHIs, a transmission electron microscope (TEM) and the associated measurement methods were used. All of the experiments were performed at the Applied Physics Institute and University Service Centre for Transmission Electron Microscopy (USTEM) at the TU Wien, with the exception of the SEM measurements, that were obtained by the Jagiellonian University in Poland.

2.1 Atomic force microscopy (AFM)

To measure the small height changes due to the irradiation with ions, an AFM (Asylum Research Cypher Scanning Probe Microscope) was used. The advantage of AFM is that insulating and conducting surfaces can be measured on a nanometer scale [27]. For this purpose, the motion of a tip with regards to the sample surface is measured. The deflection of the tip is proportional to the force acting between the tip and the surface, which is determined by the Lennard-Jones potential, shown in figure 2.1 [28].

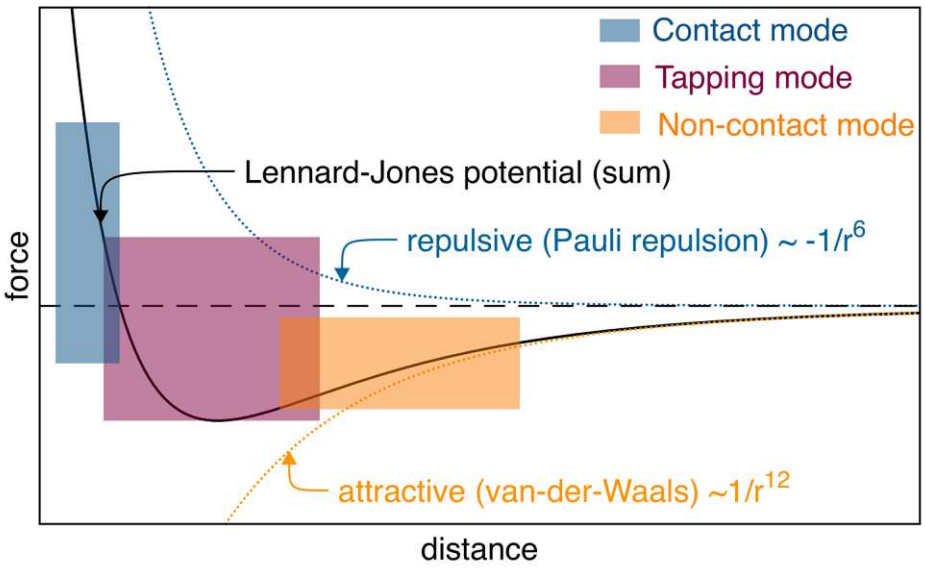

Figure 2.1: Interaction potential between the tip and the surface, resulting from two different contributions into the Lennard-Jones potential.

A laser hits the cantilever and the reflection of it gets measured by a four quadrant photo diode. In this way the actual height of the tip gets detected and is used for generating the z-coordinates. The sample gets scanned in x- and y-direction and by combining these three coordinates, a 3D picture of the sample is obtained. AFM usually moves the sample in the lateral directions via piezo elements. The working principle and main parts of an AFM are shown in figure 2.2.

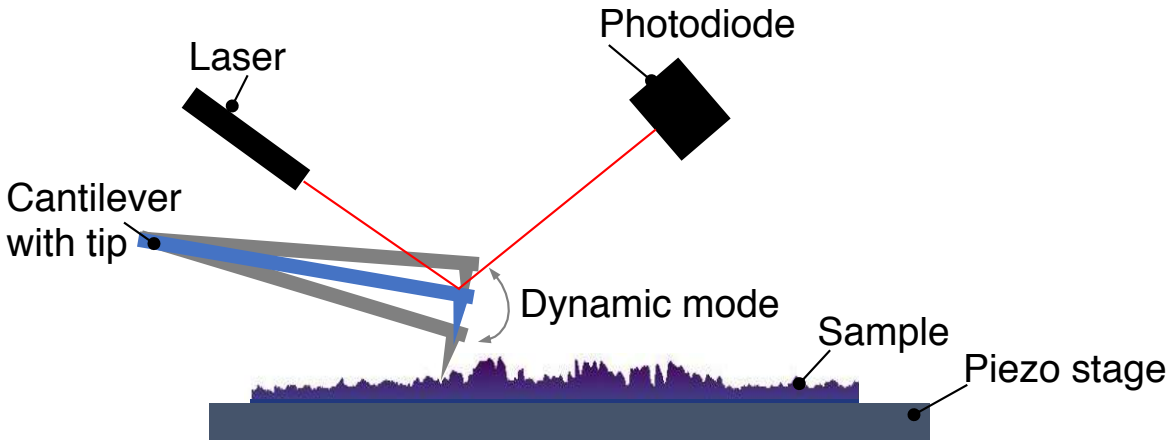

Figure 2.2: Working principle of an AFM. In this thesis, only tapping mode was used and thus, only this mode (dynamic mode) is shown in the scheme.

The AFM can be operated in different modes, including contact-mode, non-contact mode and tapping mode. In this thesis tapping mode was used. In this mode the cantilever gets excited at or near it's resonance frequency and taps softly on the surface of the sample, while a feedback loop maintains a constant force between the tip-surface interface. Tuning the tip near the resonance frequency ($f_{Resonance}$ in figure 2.3) maintains a linear relation for the interaction between the tip and surface, according to Hooke's law. The dispersion and phase of the tip can be seen in figure 2.3. Tapping mode is also used to avoid the stick-slip effect, where the tip is stuck on the surface due to attractive adhesion forces. To obtain images with reliable information the operating parameters, such as setpoint, drive amplitude, integral gain and scan speed have to be set properly. The setpoint is a constant value with which the current amplitude is compared and the difference is fed into the feedback loop, where the z-piezo adjusts the height. The drive amplitude is set by tuning the cantilever and refers to the amplitude of the cantilever, when it's not interacting with the surface. How fast the device reacts to topographical changes is determined by the integral gain. A limiting factor of the AFM is an artefact that influences the lateral size of the measured features of a sample. This is due to the finite radius of the tip, where the edge of the tip begins to measure the object instead of the lowermost part of the tip. This offset of the measurement point results in a bigger lateral length of the object. A scheme of this artefact is given in figure 2.4. However, the height information is not influenced.

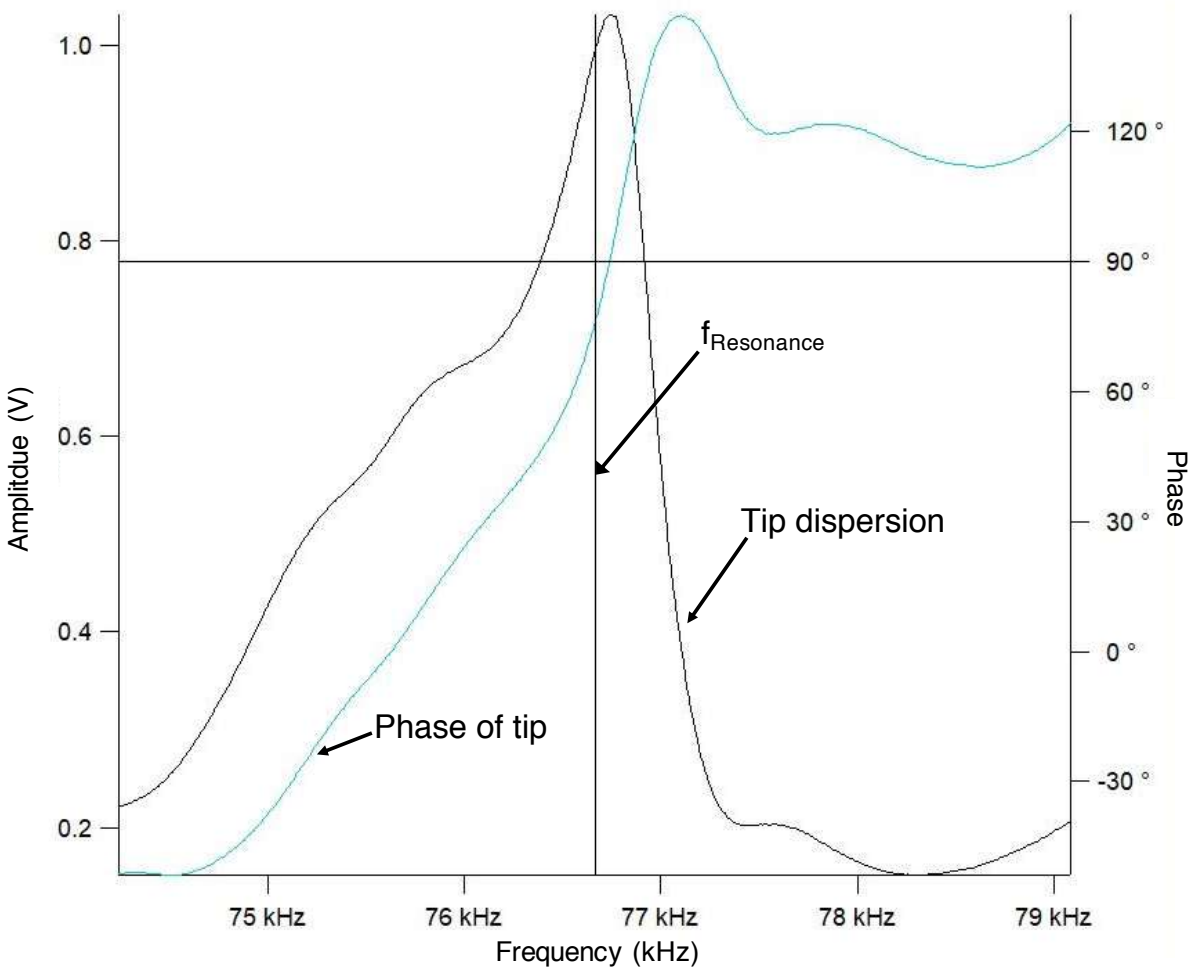

Figure 2.3: The black line is the dispersion of the tip itself when tuned. The teal line is the associated phase of the tip.

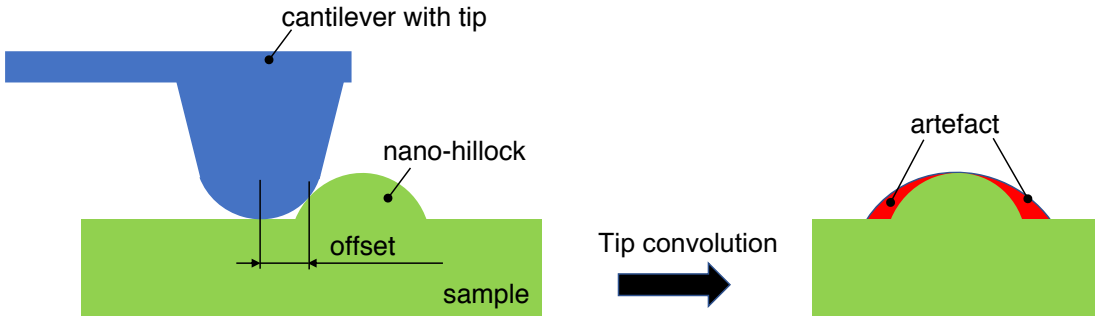

Figure 2.4: Scheme of the tip convolution. The finite tip radius lets the nano-hillocks appear bigger than they are, resulting in more volume and larger edge length. The height measurement is not influenced by this artefact.

For this thesis tips with a radius < 7 nm and a spring constant of 2 N/m (*Olympus micro cantilever, 240AC-NA*) and super sharp tips with a radius of 2 nm and a spring constant of 0.5-9.5 N/m (*Nanosensors, SSS-FM-20)* were used and can be seen in figure 2.5 (a) and (b), respectively.

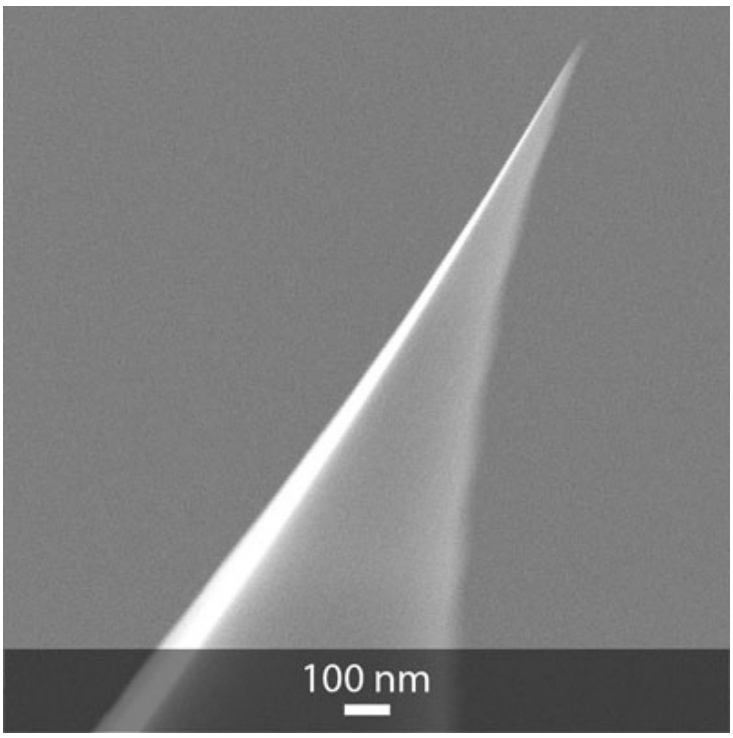

(a)

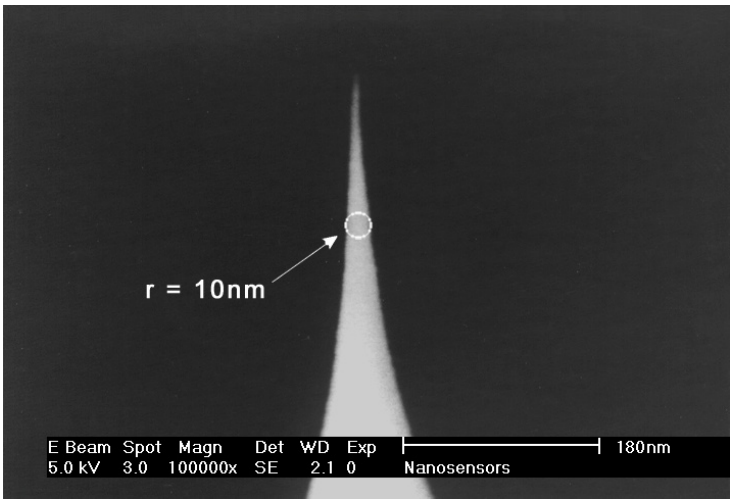

(b)

Figure 2.5: In (a) a standard tip can be seen and in (b) the supersharp tip. Images were obtained with SEM. Images taken out of [29] and [30], respectively.

2.2 Electron beam ion source (EBIS)

An EBIS can generate highly charged ions by electron impact ionisation. The EBIS used for the irradiations can be seen in figure 2.7. In case of xenon, that is used for the irradiations in this thesis, a charge state of q = 32, that corresponds to a potential energy of 19.1 keV, was achieved. At first, low charged ions are produced via electron collisions and stored in a potential trap, that is generated by three drift tubes. Once the ions are trapped, further collisions with the electron beam ionise more and more electrons of the target ions, generating high charge states.

The kinetic energy of the ions is defined by the charge state q, the potential of the third drift tube U_b and the bias of the source in terms of the beamline $U_{beamline}$:

$$E_{kin} = q \cdot (U_b - U_{beamline}). \tag{2.1}$$

The different potentials and parts contributing to the kinetic energy, namely the third drift tube U_b and bias of the source to $U_{beamline}$, can be seen in figure 2.6.

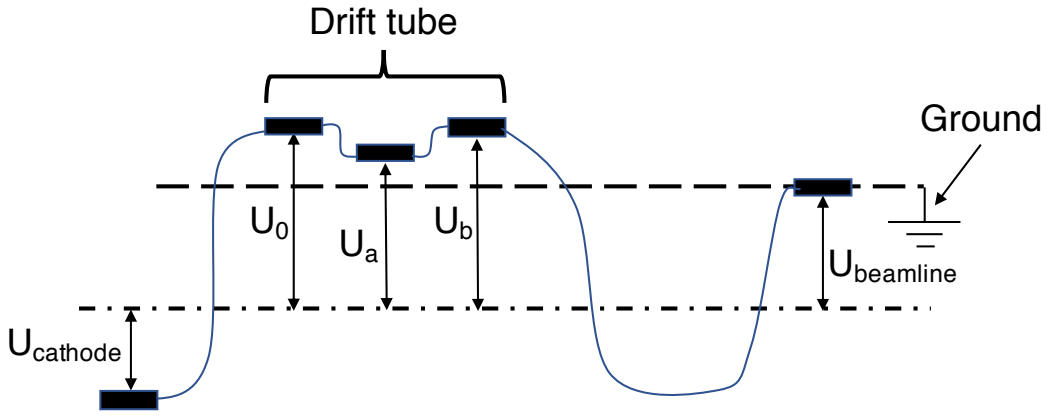

Figure 2.6: Schematic of the potentials in an EBIS. The potential trap that stores the ions during the electron impacts are marked as „drift tube“.

The potential of the third drift tube U_b is fixed at 9 kV and would correspond to a kinetic energy of 288 keV for Xe^{32+}. Therefore, a deceleration of the ions of this irradiation was necessary to compare the kinetic energy effects with the other charge states. This was important especially for the Au nano-islands, where the same target material was irradiated and the nuclear stopping power and it's effects have to be comparable. In general, the kinetic energy of the irradiations amounts to 170-200 keV and nuclear stopping dominates over electronic stopping. In table 2.1 the charge states, kinetic energies, potential energies, fluences and samples are listed. A Wien filter, which is located in front of the target chamber, selects the charge state of the ion beam via charge-over-mass separation.

Charge state	E_{kin} [keV]	E_{pot} [keV]	Fluence [ions/μm^2]	Irradiated sample
Xe^{18+}	171	3.4	750	Au nano-islands
Xe^{25+}	180	8.1	782	Au nano-islands
Xe^{32+}	180	19.1	510	Au nano-islands
Xe^{20+}	190	4.6	600	Bi cluster (CaF_2)
Xe^{35+}	196	25.5	250	Bi cluster (SiO_2)

Table 2.1: Overview of the irradiation plan and setup. E_{kin} follows from equation (2.1), E_{pot} results from the number of missing electrons [31] and the fluence was calculated.

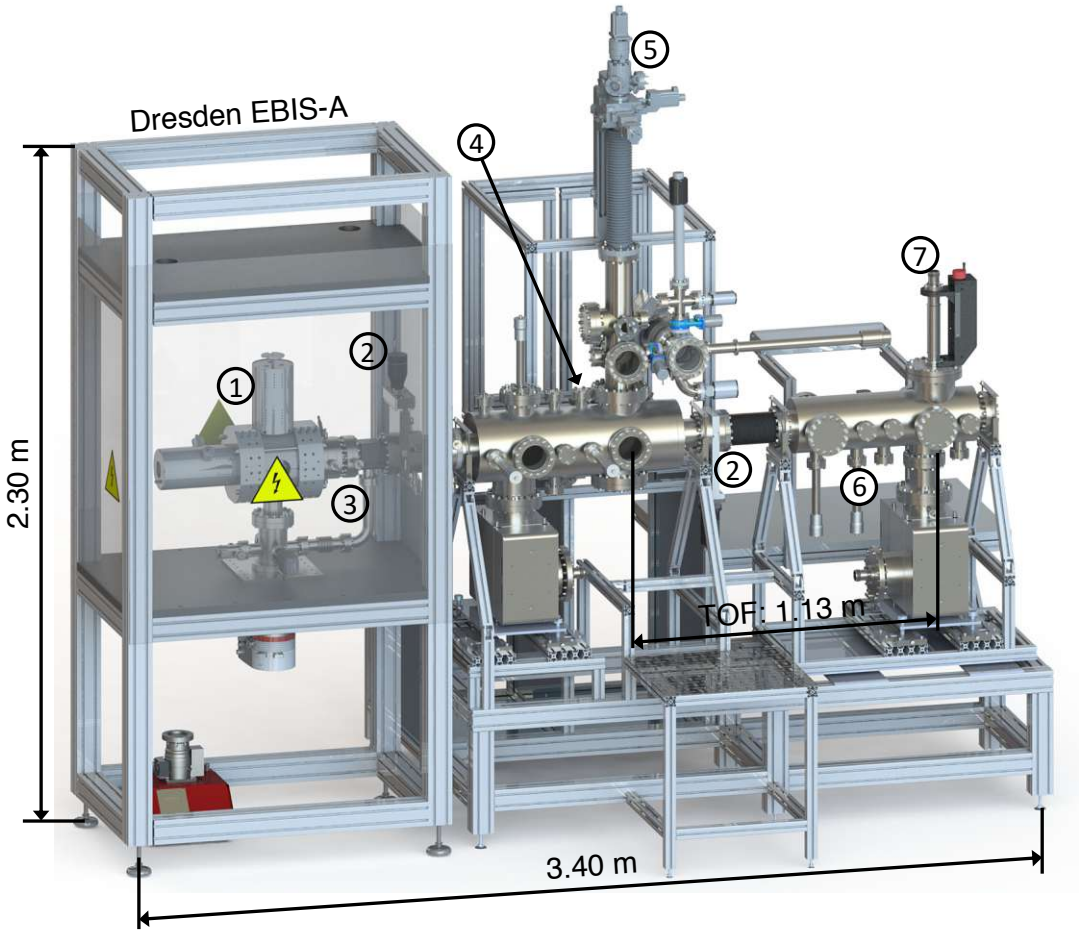

Figure 2.7: Overview of the EBIS used for the irradiations. ①: electron beam ion source ②: shutter ③: Wien filter ④: electron emission statistic setup ⑤: manipulator ⑥: deflection plates ⑦ MCP detector.

2.3 Scanning electron microscopy (SEM)

A SEM uses a focused electron beam to investigate the sample. The different parts can be seen in figure 2.8. The electron beam gets generated by thermionic or field emission and then focused by magnetic lenses. The beam scans the surface with pre-defined steps, generating an image of the sample. Different processes occur when the electrons interact with the sample. Secondary electrons, backscattered electrons, characteristic X-rays and Auger electrons are generated, just to name the most important [32]. The secondary and backscattered electrons are measured with a scintillator detector, whereas the X-rays are characterised with a semiconductor detector. By calibrating the different detectors to a specific energy loss range, a signal for imaging can be selected. Secondary electrons usually have a low energy loss in the range of a few eV to about 50 eV and can be used to determine the surface and surface near region of the sample [33]. The electron beam interacts inelastically with a bound electron from the target and this leads to an emission of this target electron, which can be measured in the detector. The created hole in the electronic shell gets filled by an electron cascade from outer shell electrons and characteristic X-rays are generated additionally.

Another imaging method is the use of the backscattered electrons, which have a higher energy loss up to about 10 keV for a primary electron beam with 20 keV. The origin of backscattered electrons is deeper in the sample, because of the elastic interaction with the target's nuclei. The yield is proportional to the atomic number, because electrons that scatter on heavier elements have a higher probability to be backscattered [34]. A scheme of the electrons and X-ray that can be used for imaging can be seen in figure 2.9.

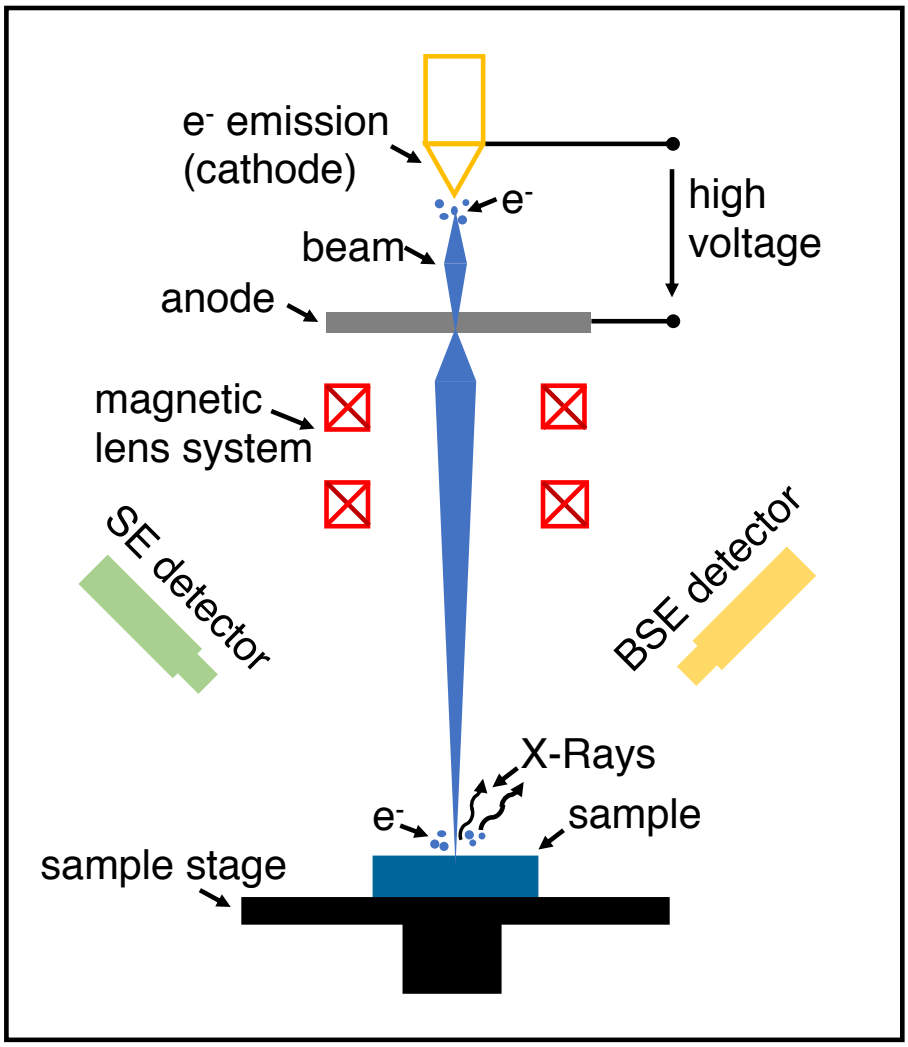

Figure 2.8: Schematic of the working principle of a SEM.

The evaluated SEM images do not contain height information, since the detector measures the electron yield, which is not directly associated with a measurable topographic quantity like in AFM. SEM, however, is not influenced by any tip artefact and therefore the lateral elongation of the Au nano-islands can be measured with higher resolution. Thus, by combining SEM with AFM a high resolution 3D topographical image can be obtained. The same Au nano-islands of a SEM and an AFM measurement were analysed regarding their lateral size and in this way a calculation of the tip artefact was possible. This was important, because the volume of the Au nano-islands is proportional to the lateral length squared and the calculations in chapter 3 were influenced by the tip artefact.

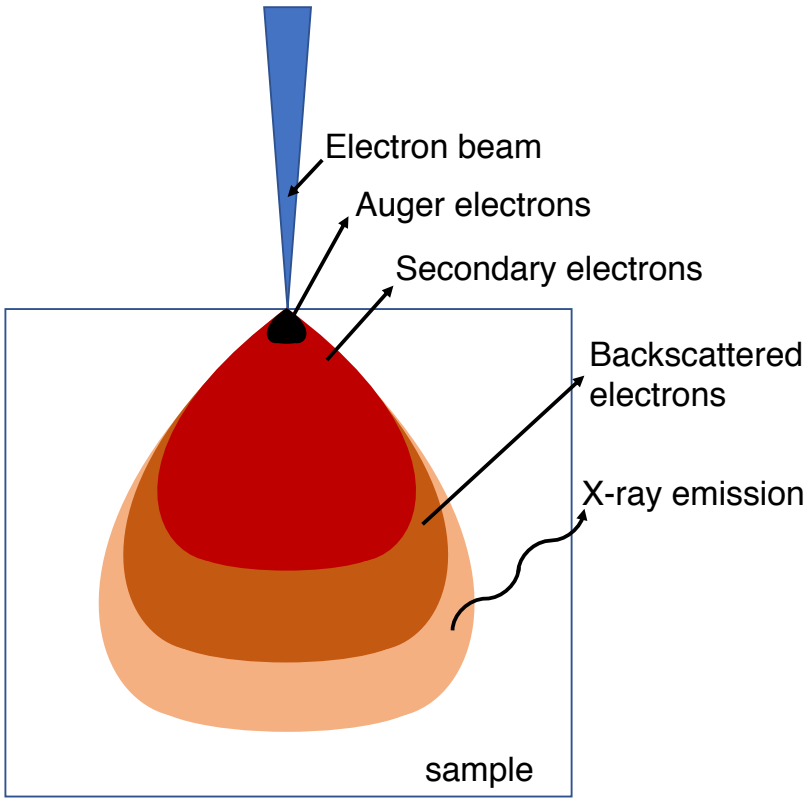

Figure 2.9: Schematic of the electron beam interacting with the sample. Auger, secondary and backscattered electrons are generated and additionally X-rays to name the most important ones.

2.4 Random ion generator

This program was coded in python during this thesis. The program counts the number of ions that hit the Au nano-islands with a specific height threshold. This should give an estimation of how many islands are hit depending on the applied fluence of an irradiation. For this purpose a real AFM image is loaded as ASC-file into the program and in this way a 3D image with x, y and z coordinates is generated. The height threshold for the Au nano-islands is set high enough to distinguish between surface roughness and islands. Subsequently, randomly distributed ions are generated, where the number of ions is determined by the fluence of the irradiation. Now, everytime an island higher than the height threshold is hit, a counter detects this. A scheme of this simulation is given in figure 2.10. However, the program does not consider the potential energy and volume of the Au nano-islands, whereas these parameters only influence the height loss and not the number of islands hit. Concluding, the program should reflect the amount of hit nano-islands to estimate the correctness of the histogram shifts of the irradiations, which is represent by the histograms before an irradiation and after an irradiation. As an example, for a fluence of 780 ions/μm^2 the number of Au nano-islands hit amounts to 55 %. In table 2.2 all used fluences and the simulated amount of Au nano-islands hit is shown.

Fluence [ions\µm^2]	Au nano-islands hit [%]	Irradiation with
1000	71	Xe^{1+}
750	54	Xe^{18+}
780	55	Xe^{25+}
510	36	Xe^{32+}
1060	75	Xe^{40+}

Table 2.2: Table of the simulated fluences and number of Au nano-islands hit.

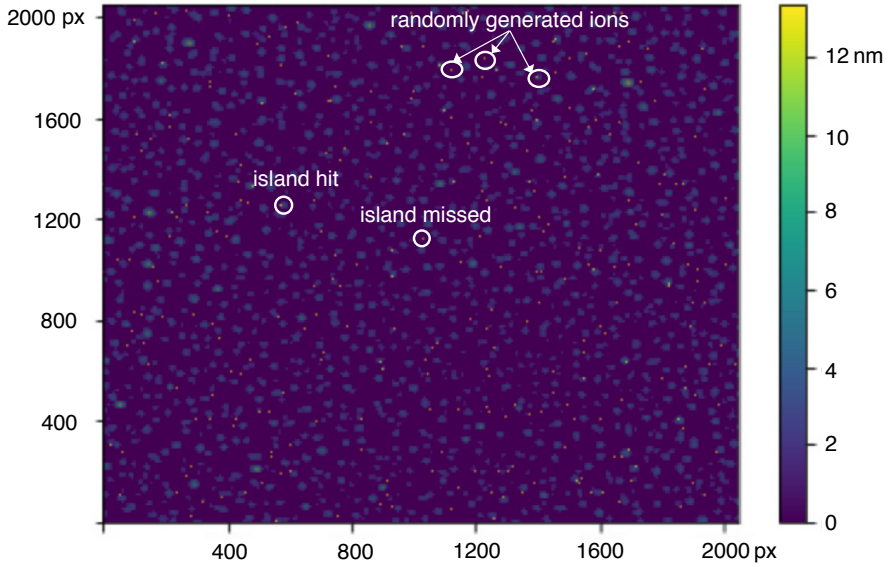

Figure 2.10: Scheme for the evaluation method used in the simulation.

2.5 Transmission electron microscopy (TEM)

A TEM is a microscope that uses electrons, similar to SEM, to obtain images of a certain sample. Considering the wave-particle dualism of electrons, the wavelength of the electrons in a TEM is in the order of picometer. In this way, a sub-nanometer resolution is possible [35]. TEMs are utilised to determine the crystallographic properties, crystallinity, chemical analysis, optical properties and many more [36].
The TEM (Philips TECNAI F20) used for the investigation of the latent tracks made by SHIs was used with acceleration voltages between 60-200 kV [37]. The working principles of a TEM for diffraction pattern (DP) and image mode (IM) are shown in figure 2.11 (a) and (b), respectively. The electrons get emitted from a cathode by thermionic or field emission and are then acceleration towards the anode. After the acceleration the electron beam enters the first magnetic lens systems, namely the condensor system. The electron beam gets deflected according to the lorentz force

$$\vec{F} = -e \cdot (\vec{v} \times \vec{B}), \tag{2.2}$$

where $\vec{F}$ is the force acting on the electrons, e the elemental charge, $\vec{v}$ the velocity of the electrons and $\vec{B}$ the magnetic field that is generated by the coils.

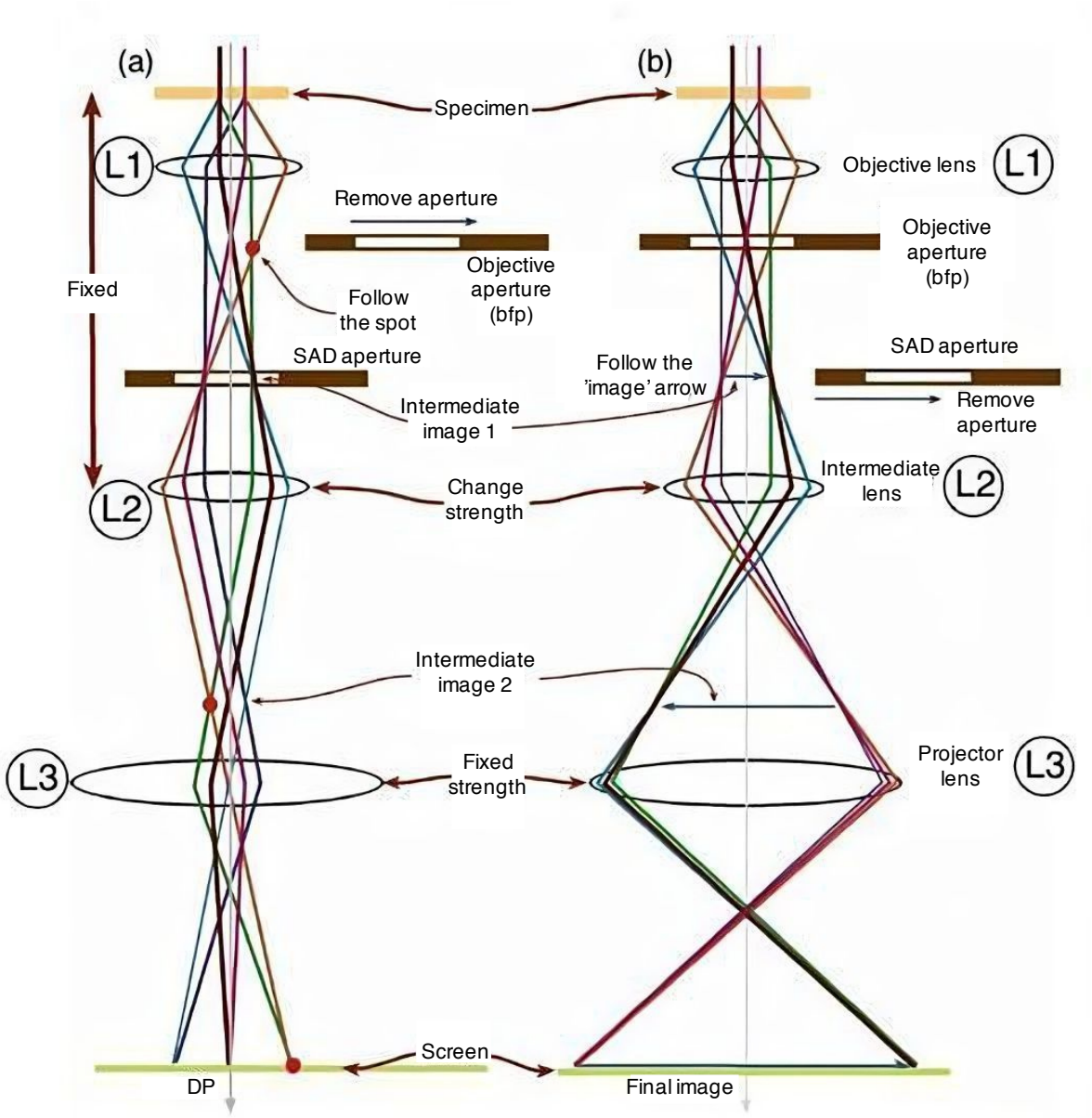

Figure 2.11: Schematic of the working principle of a TEM. The left image (a) shows the setup for diffraction mode and the right image (b) for the image mode. The selection of the DP or IM depends on the strength of the magnetic field of the intermediate lenses. Image adapted and taken out of [38].

The condensor system allows to set the illuminated area on the sample (spot size) and the convergence angle. The spot size defines the intensity of the beam and the convergence angle is set to minimise lens errors, such as chromatic and spherical aberration. The next part is the sample stage, where the electron beam interacts with the sample elastically and inelastically. After the interaction with the sample, the electron beam enters the objective lens system („L1“). Here, a diffraction pattern of the sample is formed in the back focal plane of the objective lens and a magnified image of the sample is generated in the image plane of the objective lens. The electron beam for the formation of the diffraction pattern is shown in figure 2.11 (a) and the formation of the enlarged image is given in figure 2.11 (b). The next lens system, the intermediate lens („L2“), determines which mode, diffraction pattern or image mode, gets magnified onto the fluorescent screen.

The projector lenses („L3“) are only responsible for the magnification of the selected mode.

2.5.1 Sub-imaging and spectroscopy methods used in TEM

Only the imaging techniques that were able to visualise the latent track of the SHI are mentioned in the following chapters. Many more imaging and spectroscopy techniques were used to visualise the damage of the SHI and the discontinuous part of the track, but they did not lead to a useful result.

High-resolution TEM (HR-TEM)

High-resolution TEM offers a microscope method to visualise atomic columns with a resolution of 0.24 nm for the TECNAI F20 [37]. The image is formed by interference of the scattered electron wave and the transmitted electron wave and ends in a phase shift between these two beams. Only electrons that are bragg diffracted in the coulomb field of the atomic nuclei interfere constructively and hence, form the final high-resolution image. The sample for HR-TEM must be as thin as possible, because the probability of inelastic scattering events increases with the sample thickness [38]. However, some electrons scatter inelastically, but are not used for the imaging process, since they end up in incoherent phase shifts, energy loss and very low scattering angles and even may damage the sample due to ionisation processes [38]. By setting the beam alignment, lens errors, convergence angle and defocus (Scherzer focus) properly, visual information of the crystalline structure of the sample can be obtained.

Scanning transmission electron microscopy (STEM)

Scanning transmission electron microscopy uses a focused electron beam that hits the sample and scans the region of interest. After the interaction, the transmitted and diffracted electrons are collected on a detector. Depending on the angle at which the electrons are scattered and detected, different imaging sources are available. Bragg diffracted electrons make up the bright field (BF) and dark field image (DF), whereas high-angle scattered electrons are collected in the high-angle annular dark field (HAADF) detector. The different imaging source can be selected by adjusting the camera length of the detector, that determines the area around the central axis of the detector, where the incoming (scattered) electrons are measured. Hence, by adjusting the camera length, one can select the electrons that one wants to use for the imaging process (Bragg, BF, DF, Rutherford: Z-contrast, mass-to-thickness & HAADF). The HAADF signal contains the Z-contrast imaging mode, that is proportional to the atomic number Z, density of the sample ρ and thickness of the sample t

$$I \propto \rho \cdot t \cdot Z^{3/2} \tag{2.3}$$

and is derived in the course of Rutherford's scattering formula. For STEM the convergence angle must be set properly to minimise the lens errors, since they are proportional to the convergence angle. The different aberrations can be seen in figure 2.12. This is achieved by putting in the right apertures. Furthermore, the optimal focus (Scherzer focus) has to be set, to achieve the minimal point resolution of 0.15 nm for the TECNAI F20 [37].

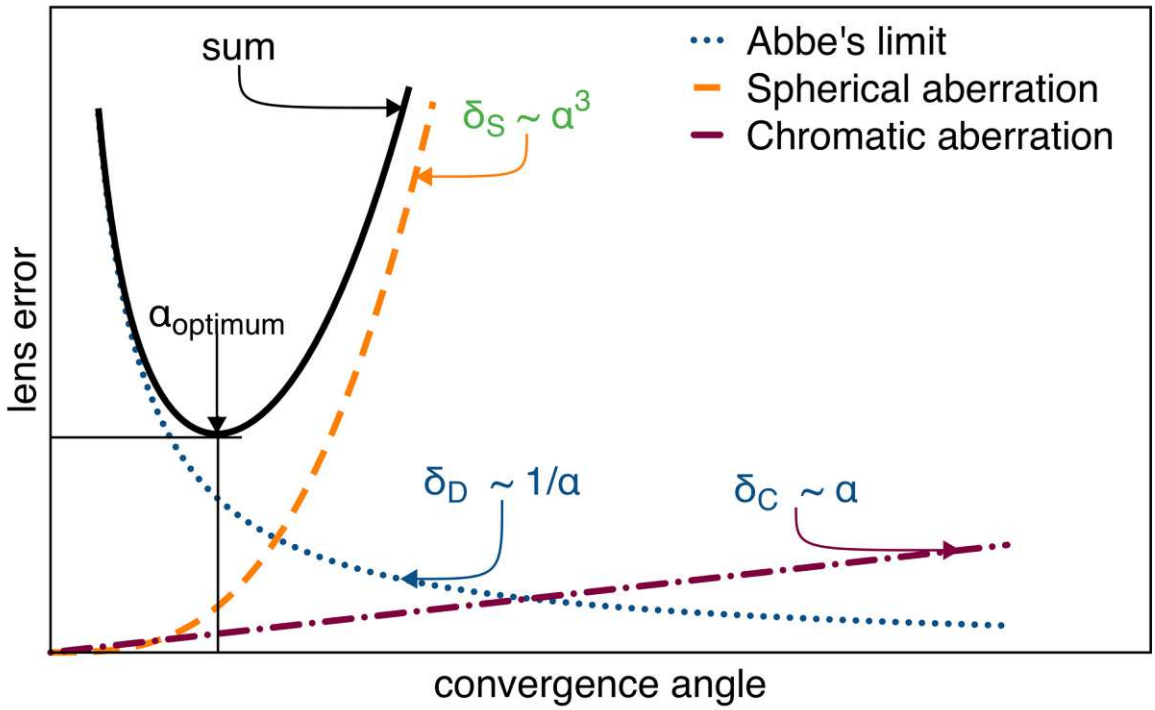

Figure 2.12: Optimum convergence angle that has to be set for STEM and the contributing aberrations to consider.

Electron energy loss spectroscopy (EELS)

Electron energy loss spectroscopy is a versatile tool to determine, e.g. optical properties, electronic structure and chemical composition just to name a few. The electrons transmitted through the sample can be analysed regarding their energy-loss distribution. The interactions include elastic and inelastic scattering events and this determines the scattering angle and the energy lost due to the interaction. Elastic collisions arise from the interaction of the electron beam with the coulomb field of the nuclei in the target and the inelastic collisions contain electron-electron interaction. The electrons are collected in a magnetic prism and measured regarding their kinetic energy. The spectrum in figure 2.13 contains energy losses from 0 eV to about 2 keV and can be divided into different physical processes. The zero-loss peak (ZLP) contains electrons that did not interact with the sample. The low-loss regime covers an energy range of $\sim$ 10 to 100 eV and represents the energy loss due to single and multiple plasmon excitation(s). Here, the optical properties of a sample are represented, because the plasmon is a collective charge oscillation of valence electrons. The high-loss regime can be interpreted in terms of energy loss due

to ionisation of inner shell electrons of an element and represents the fine structure. This regime extends to about 2 keV energy loss. The optical properties, determined by the bandgap of a semiconductor or insulator, differs between rutile (tetragonal unit cell) and amorphous TiO_2 [39]. So, if a phase transition would have happened, the difference could be measured in the plasmon spectrum with EELS. The energy resolution amounts 0.7 eV for the Tecnai F20 when performing EELS, which is limited by the field emission gun that is used in this TEM.

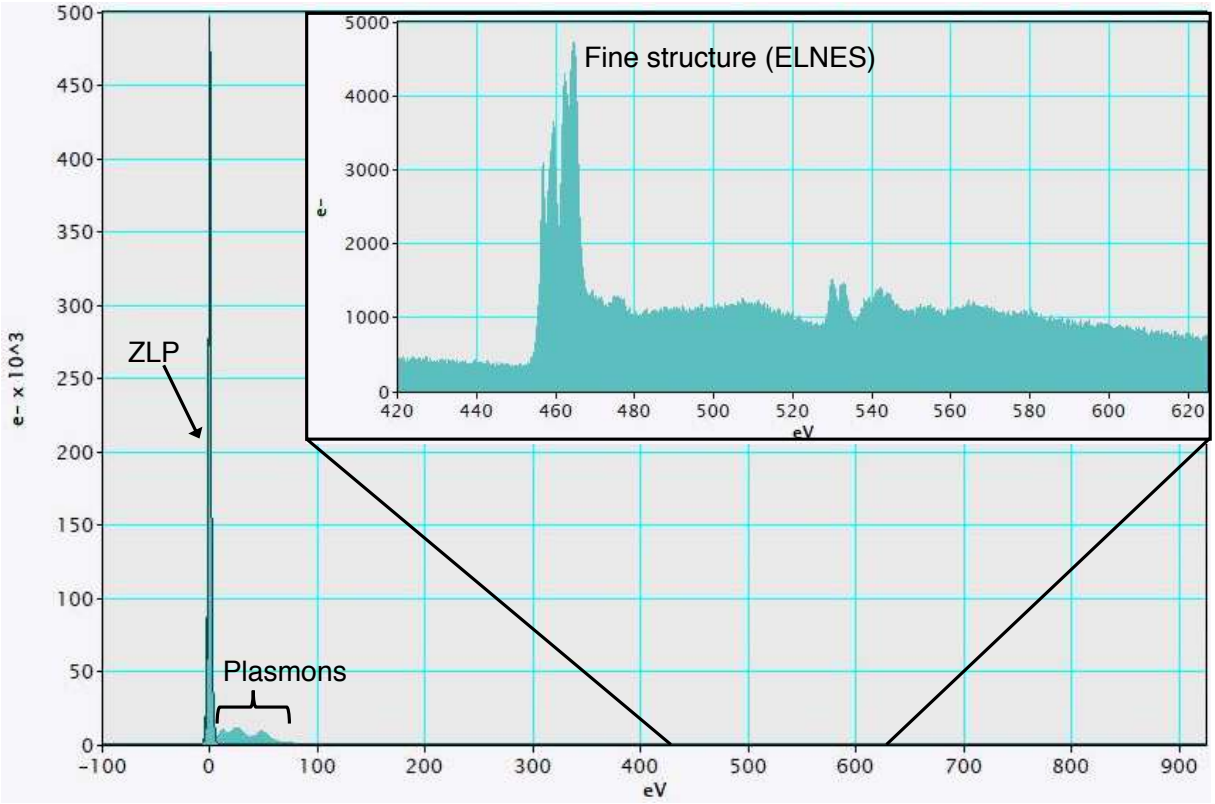

Figure 2.13: EELS spectrum obtained from a TiO_2 sample, which was irradiated with SHIs. The y-axis marks the amount of measured electrons and the x-axis the energy loss of these electrons in eV.

2.6 Samples and sample preparation

2.6.1 Samples for the investigation of HCIs potential effects

Metallic nano-islands and clusters were irradiated to study potential energy effects of HCIs. For this purpose either gold nano-islands and bismuth clusters on insulating substrates were irradiated with HCIs.

Au nano-islands on MoS_2

In the first step of producing Au nano-islands, a MoS_2 monolayer was grown on a silicon wafer with a 290 nm layer of SiO_2 with chemical vapor deposition (CVD), which was obtained by the group of A. Turchanin at the University of Jena [40]. The thickness of 290 nm is of high importance, because with this the monolayered MoS_2 can be optically distinguished from multilayered MoS_2 by a blue-ish colored surface. In CVD a carrier gas containing the atoms that are deposited and a reactant gas are fed into a heated chamber, with the substrate mounted. The chamber is at atmospheric pressure and sulfur (S) and MoO_3 powder with argon as carrier gas was used. At first, the MoO_3 powder and substrate was heated up to 750°C under constant argon flow and after that, the S was heated up to 200°C and transported to the Mo powder, where MoS_2 flakes with a lateral size of up to 20 µm have grown in 10 minutes. The lattice structure of the MoS_2 can be seen in figure 2.14 (a) as top view and in figure 2.14 (b) as trigonal prisma, respectively. In the next step, in a similar process the Au nano-islands were grown on the MoS_2 monolayer at the Jagiellonksi University in Poland by the group of F. Krok [41]. The substrate with MoS_2 flakes on it was put into a UHV chamber with a pressure of 10^{-10} mbar. Two gold monolayers were deposited for 30 minutes at 523 K, checked with a quartz microbalance. The Au nano-islands grow epitaxilly (111) on the MoS_2 monolayer and adhere on it by weak van-der-Waals forces. The Au nano-islands have a lateral length of 25-80 nm and a height of about 7 nm in average and grow as equilateral triangles on the MoS_2 monolayer. The sample was irradiated with Xe^{18+}, Xe^{25+} and Xe^{32+} with similar kinetic energies of 180 keV and similar fluences of 500-780 ions/µm^2.

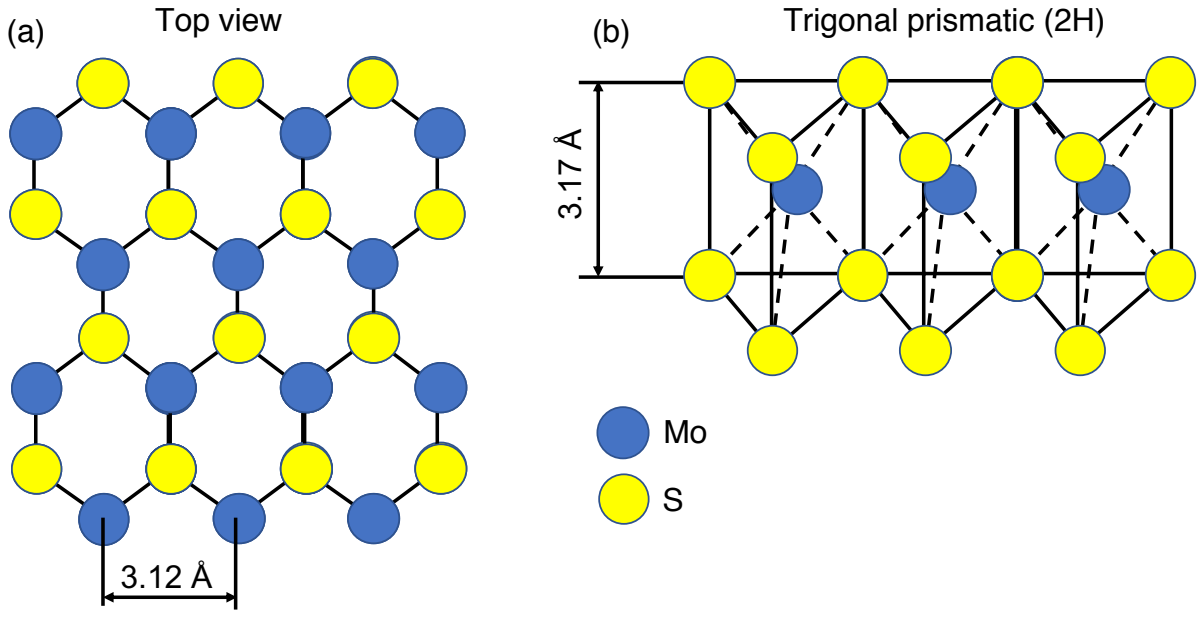

Figure 2.14: Schematic of the lattice structure of 2H-MoS_2. In (a) the top view is visible and in (b) the trigonal prismatic with the corresponding lattice constants.

Bismuth clusters on CaF_2 and SiO_2

The bismuth clusters on CaF_2 and SiO_2 were produced at the University of Innsbruck, by the group of Elisabeth Gruber and Paul Scheier. The deposition of the clusters was performed with a helium-nanodroplet (HND) beam [42]. Helium becomes superfluid at 2.17 K and the doping of the helium is done by laser ablation [43]. The dopants are catched inside the helium-nanodroplet and interact with each other by attractive van-der-Waals forces. The HNDs get produced via supersonic expansion through a small nozzle and are then accelerated onto a sample surface. Upon collision with the surface, the weakly bound molecules inside the HND survive the collision on the surface to some extent without being backscattered [44]. The helium evaporates and the dopants grow on the substrate. Not all samples were used for the irradiation, because the density of the bismuth clusters varies with the deposition time. As a consequence, on some samples the whole surface was covered with bismuth, meaning that the nanodroplets of bismuth clustered together. As a first approach, the samples with the smallest Bi clusters were chosen and irradiated with 200 keV Xe^{35+} and 190 keV Xe^{20+} with a fluence of 250 and 600 ions/μm^2, respectively.

2.6.2 Samples for the investigation of the latent tracks of SHIs

The insulating bulk material TiO_2 was chosen, in order to investigate effects found in recent studies in more detail. Furthermore, an additional measurement with Al_2O_3 was performed to compare the differences between two substrates. A set of TiO_2 was irradiated at the Ruđer Bošković Institute in Zagreb with iodine ions with a kinetic energy in the range of 10 MeV to 38 MeV. To study the formation of the latent track and to visualise the discontinuous part of the track, the sample irradiated with 23 MeV I^{6+} and a fluence of 500 ions/μm^2 was investigated with AFM and TEM. This sample was used to find the settings and techniques of the TEM to visualise the whole part of the track. Another sample was picked, with irradiations close to a proposed threshold of track formation, which is the sample irradiated 13 MeV I^{8+}. The fluence was the same as for the 23 MeV I^{6+} sample. The goal of this experiment was to determine the threshold for the stopping power, where no track is created. Additionally, the stopping power gets enhanced with increasing charge state until the impinging ion reaches it's equilibrium charge state, that is given by equation 1.3 and shown in figure 2.15. The equilibrium charge state ($q_{effective}$ or $q_{equilibrium}$) differs from the charge state when the ion impinges the target's surface. The length at which this occurs and damage can be observed, due to the stopping power being then higher than the heat of fusion (E_{HoF}) of the material, may be visualised with TEM techniques. A measurement with another sample was performed to distinguish differences between different substrates. For this purpose, an Al_2O_3 sample was irradiated with 28 MeV I^{14+} and a fluence of 600 ions/μm^2.

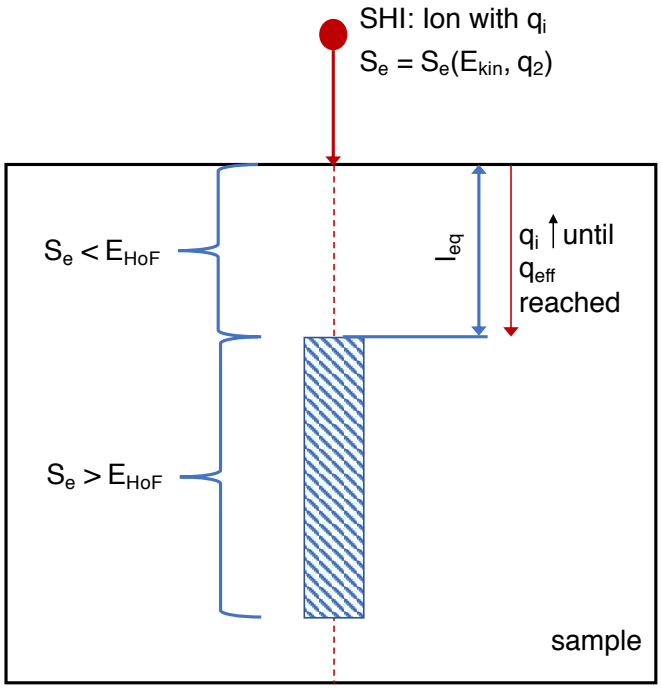

Figure 2.15: A scheme of the enhancement of the stopping power S_e due to the charge state.

3 Results and discussion

3.1 Gold nano-islands on MoS_2

The sample was divided into three subareas and measured with AFM before the irradiations were performed. About 6-8 MoS_2 flakes per subarea were measured and analysed. Within one MoS_2 flake, three 2.5 µm x 2.5 µm AFM images were obtained. In each 2.5 µm x 2.5 µm image about 100 to 150 Au nano-islands were analysed regarding their height and volume. An aperture was built to irradiate only a specific area of the sample and the irradiated areas can be seen as hatched areas in figure 3.1. Furthermore, the charge state used for the irradiations and the applied fluence is visible in this figure.

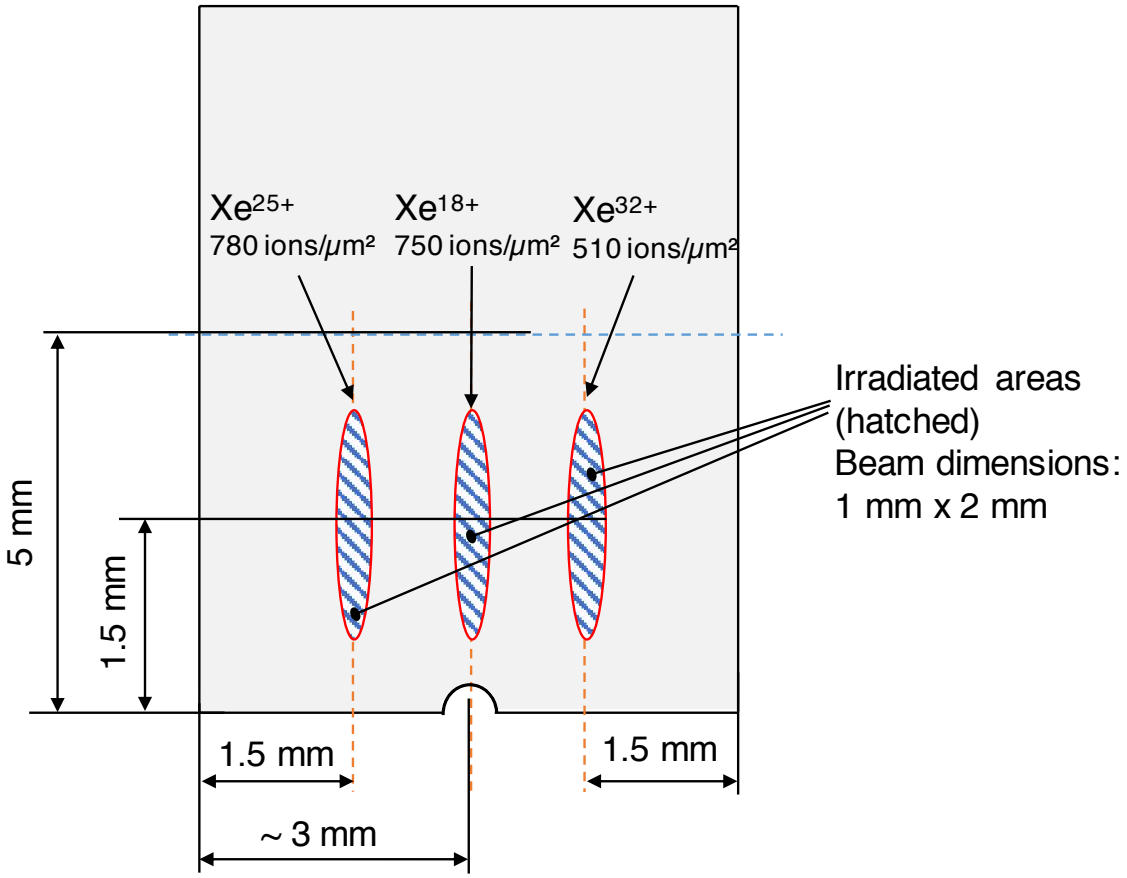

Figure 3.1: Schematic of the sample used for HCI irradiations. Au nano-islands only can be found below the blue dashed line.

The irradiations were performed at the Neutral and Ion Energy Loss Spectrometer (NIELS) facility of the Institute of Applied Physics at TU Wien.

The kinetic energy of the irradiations amount approximately the same value to compare the kinetic energy effects, like nuclear stopping power. To maintain similar kinetic energy for higher charge states the source has to be biased, according to equation (2.1). This method decelerates ions with higher charge states. The sample was mounted on a sample holder and transported into the target chamber, which had a base pressure of about $1 \cdot 10^{-8}$ mbar. The beam was analysed with a delay-line microchannel plate detector (MCP). To minimise the background and enhance the ion current, electrostatic lenses were used to focus the beam. Also a beam steerer was used to correct beam misalignment. The sample was placed in the path of the beam and with the desired fluence, the irradiation time was calculated. To determine the fluence, which is the number of ions per area, the beam current, beam area and irradiation time is used. After the irradiation series the sample was put again into AFM and the same MoS_2 flakes were measured. Within some of the MoS_2 flakes the same Au nano-islands were found after the irradiation, providing a crucial one-to-one comparison for the irradiated islands.

Results for Xe^{1+}

The irradiations were performed at the Helmholtz-Zentrum Dresden-Rossendorf with an Standard Ion Implanter, where the sample was irradiated with single charged xenon ions with a kinetic energy of 180 keV and a fluence of 1000 ions/μm^2. This irradiation indicates if single charged ions, or the kinetic energy, can alter the nano-islands. Figure 3.2 shows no changes due to the irradiation with Xe^{1+}, which is probably due to the limited resolution of the AFM. In the past, craters with a diameter of approximately 5 nm were found [9, 10], which cannot be resolved with this AFM.

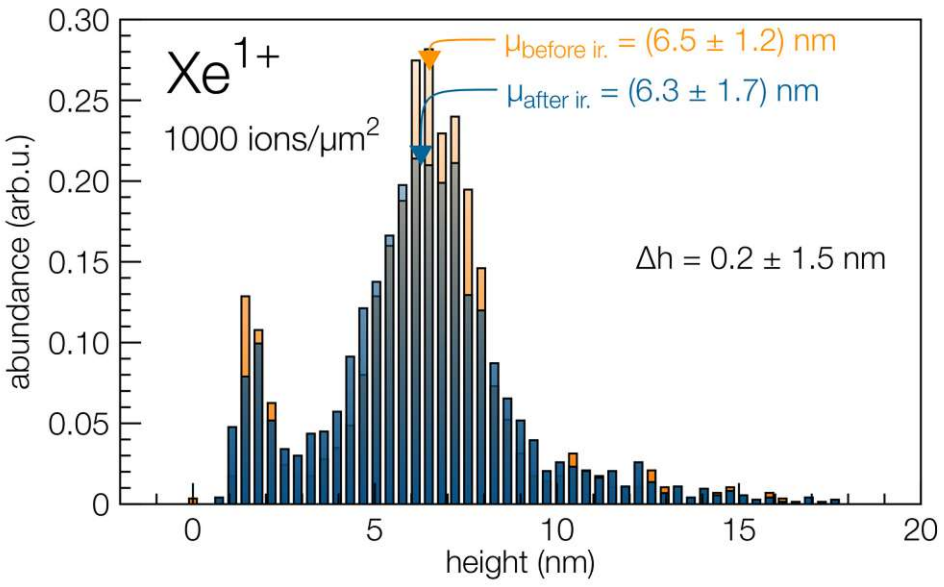

Figure 3.2: Histogram representing the AFM measurement after the irradiation with Xe^{1+}, which indicates no changes due to the irradiation.

Results for Xe^{18+}

Figure 3.3 shows the height before and after the irradiation with Xe^{18+}. The height loss amounts (0.5 ± 1.3) nm and the standard deviation of the distribution is higher than the mean value for the height loss, thus a height loss can not be determined unambiguously. Figure 3.4 (a) and figure 3.4 (b) show the AFM images before and after irradiation, respectively. No height changes can be determined visually with these two images. The AFM image after irradiation appears slightly darker than before irradiation. This may be due to surface roughness or different leveling of the analysis software, that can be triggered by different artefacts of the AFM measurement, like line leveling, debris on surface or tip artefact [45].

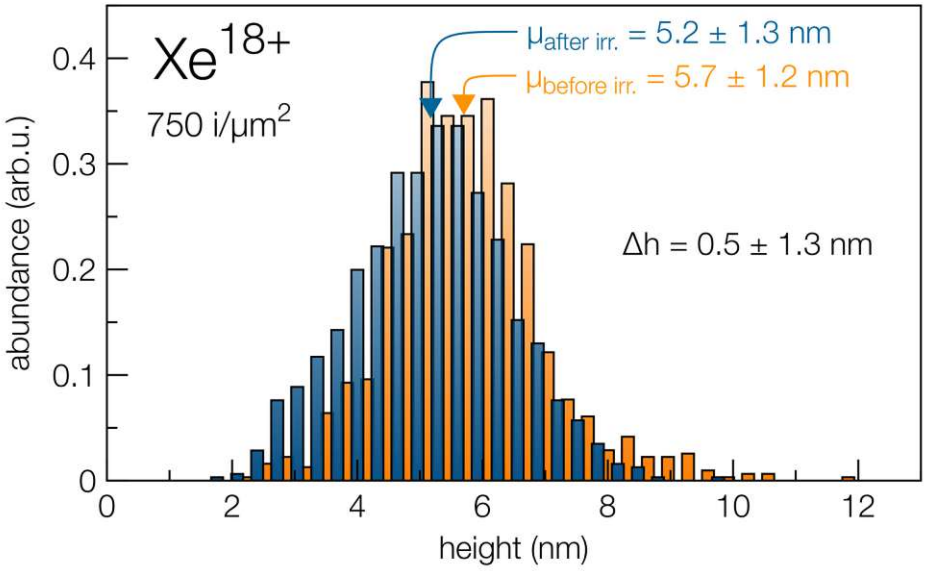

Figure 3.3: Result of the irradiated Au nano-islands with Xe^{18+}. A height loss of approximately (0.5 ± 1.3) nm was observed.

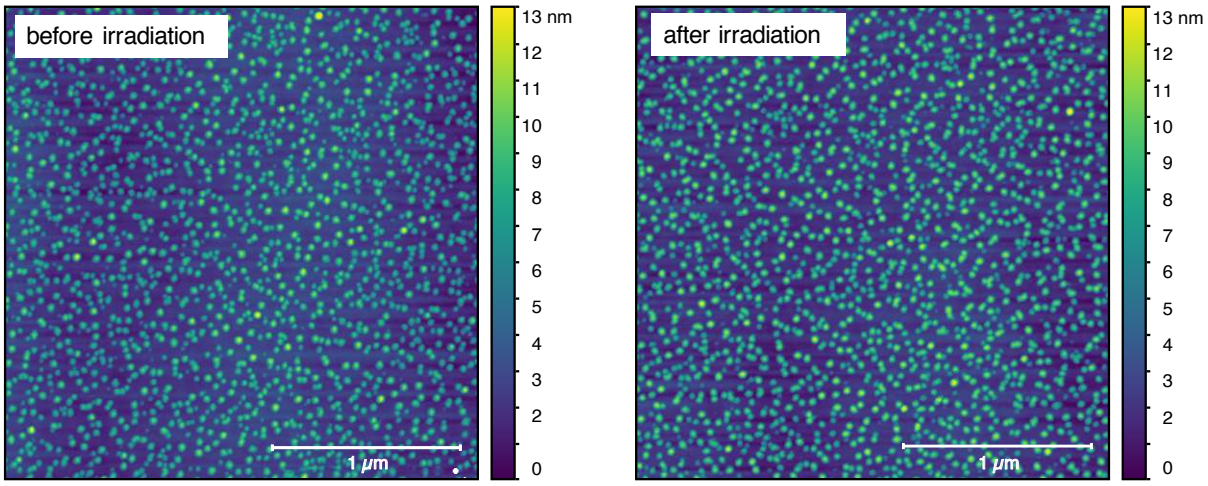

(a) (b)

Figure 3.4: In (a) the AFM image before the irradiation and in (b) after the irradiation with Xe^{18+} is shown.

Results for Xe^{25+}

The irradiation with Xe^{25+} yields a height loss of (1.8 ± 1.5) nm and can be seen in figure 3.5 and the histogram shift was checked with the program for the number of Au nano-islands hit. For a fluence of 780 ions/μm^2 the number of Au nano-islands hit amounts to 55% and fits approximately with the histogram shift in figure 3.5, that amounts to the islands, which were altered due to the irradiation. The program includes a height threshold of the raw ASC-file, which may influence the amount of Au nano-islands hit. This was checked and deviations of about 3 % for the number of Au nano-islands hit were observed, when the height threshold was set to be 1 nm instead of 2 nm.

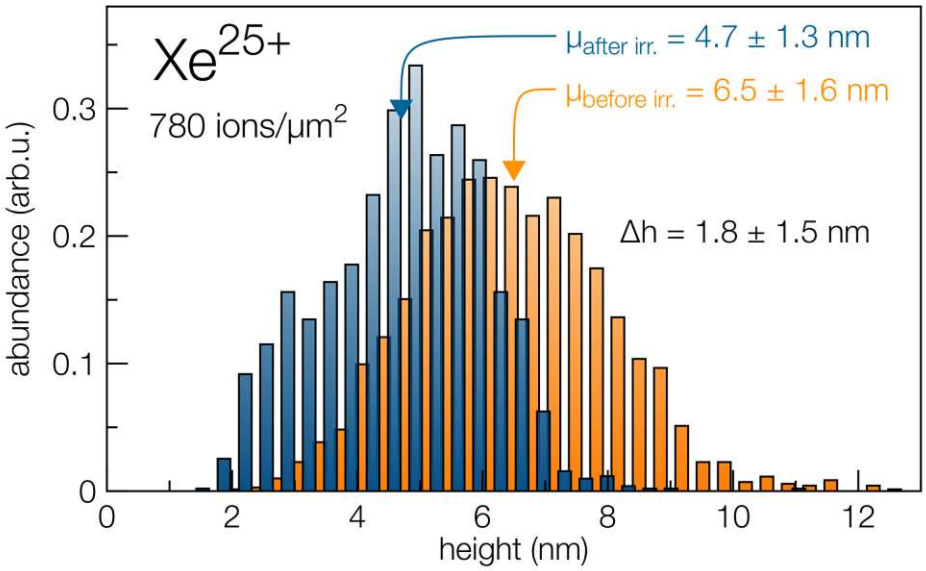

Figure 3.5: Result of the irradiated Au nano-islands with Xe^{25+}. Due to the higher fluence more Au nano-islands were effected and more height loss was found due to the higher potential energy.

The change of the height can be seen optically in figure 3.6 (a) and figure 3.6 (b), by comparing the Au nano-islands (seen as colored spikes) of both images. The height of the Au nano-islands is represented by a color scale and is for the tallest islands yellow-ish. After the irradiation with Xe^{25+} less yellow-ish Au nano-islands spikes can be seen, resulting in a reduction of height.

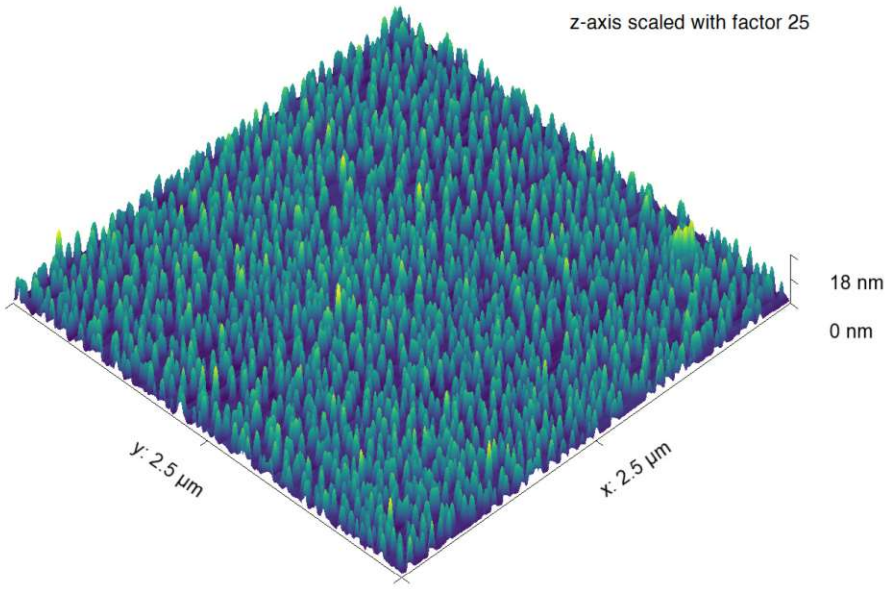

(a)

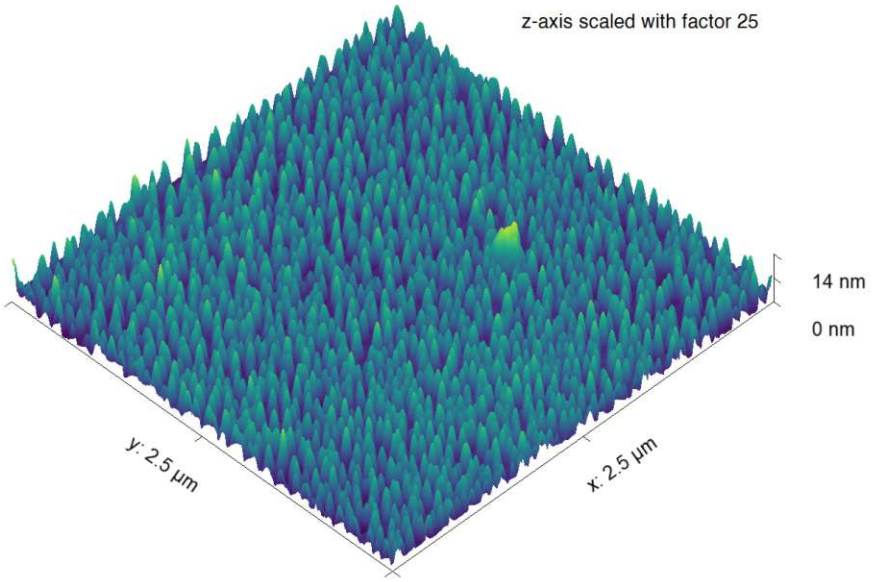

(b)

Figure 3.6: Both images are 3D plots made with Gwyddion [46] and the z-axis is scaled by a factor of 25 to compare the height of the Au nano-islands. In (a) the AFM image before irradiation and in (b) the AFM image after irradiation is shown and a difference in the height can be seen in these two images.

For this charge state a one-to-one comparison was achieved, because the same Au nano-islands were found on an AFM image before and after irradiation, that can be seen in figure 3.7 (a) and figure 3.7 (b), respectively. The Au nano-islands in figure 3.7 (b) appear bigger, because a different tip was used and subsequently, the effect of the tip convolution differs. Additionally, like in the 3D images the heights of the Au nano-islands after irradiation appear smaller than before irradiation.

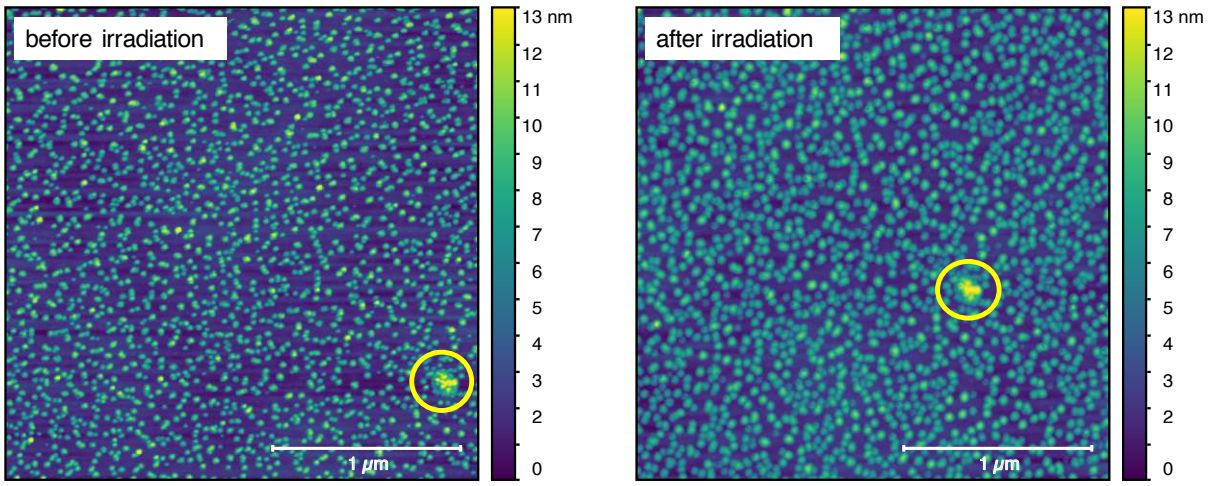

(a) (b)

Figure 3.7: In (a) the AFM image before the irradiation and in (b) after the irradiation with Xe^{25+} is shown. The yellow circles mark the spot that was used for the identifaction of the same spot before and after irradiation.

For the one-to-one comparison 104 Au nano-islands were compared with each other before and after irradiation, giving a one-to-one height loss characterisation and a volume threshold, where islands seem to be more effected by the potential energy of the HCI. The plot in figure 3.8 represents this one-to-one measurement. The radii of the circles amount the height loss for an island and the color represents the volume which was measured before the irradiation with AFM. The islands with the highest change in height can be found in the lower left of figure 3.8. In this figure three data points were corrected, because tip artefacts caused a big reduction in height for the largest islands, which is incosistent with previous measurements. In conclusion, the highest height change experienced nano-islands with a small volume up to about 1800 nm^3. At higher volumes the nano-islands seem to be less effected by the potential energy of the HCI. The right y-axis refers to a recalculated volume, where the tip artefact is already corrected. This was achieved by additional SEM measurements and one-to-one comparison of the edge length of the Au nano-islands between SEM and AFM measurement. The evaluation was obtained with Gwyddion and about 50 nano-islands were compared with each other. The difference in the edge length between AFM and SEM amounts to a factor of 1.79, about which the AFM measured islands are bigger and can be seen in figure 3.9. This value was taken and the volume of the Au nano-islands was recalculated. The recalculated volume threshold can be taken for the evaluation of how much energy one Au atom gains due to the deposited potential energy. Considering the heat of fusion for gold, which amounts 12.55 kJ/mol and the atomic volume of gold being 58.9 atoms/nm^3, one can calculate the energy for heat of fusion per Au atom being 130 meV/atom. The corresponding volume for 130 meV/atom amounts to about 1000 nm^3, which is the volume threshold for complete melting of the nano-island.

By comparing this volume threshold of 1000 nm^3 with the measured volume threshold of 1800 nm^3, where nano-islands seem to be less effected by the HCI in terms of height loss, a theoretical approach supports the result. Additional approximations were made, such as 100% energy retention in the nano-island.

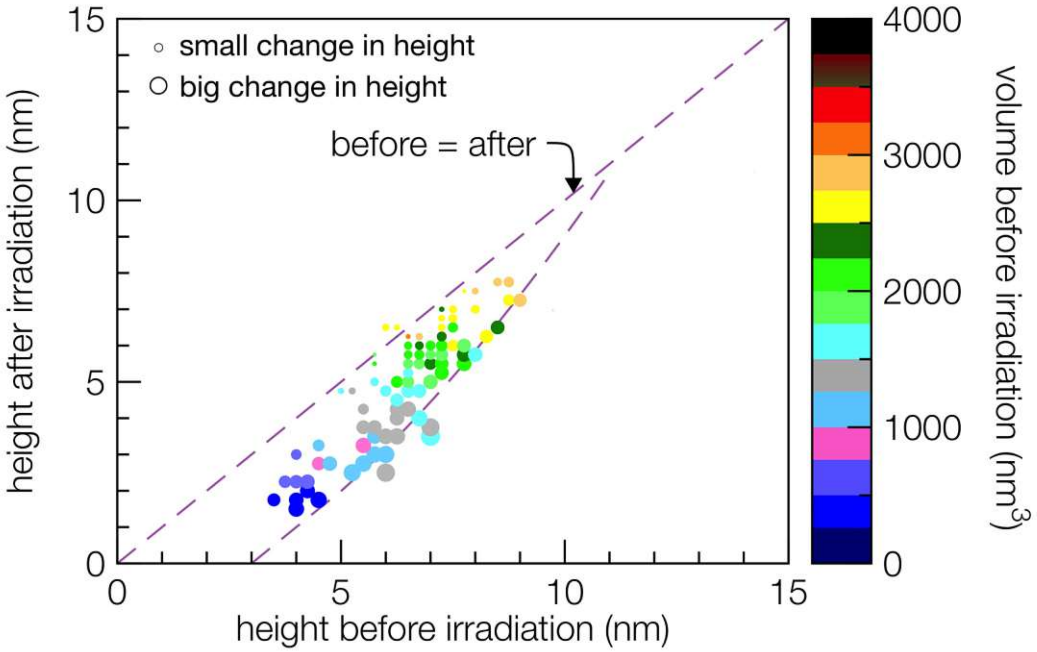

Figure 3.8: Plot for the one-to-one comparison of the Au nano-islands. The found volume threshold amounts 1800 nm^3 and is given by the color scale, where higher volumes seem to be less effected in terms of height loss due to the HCI irradiation.

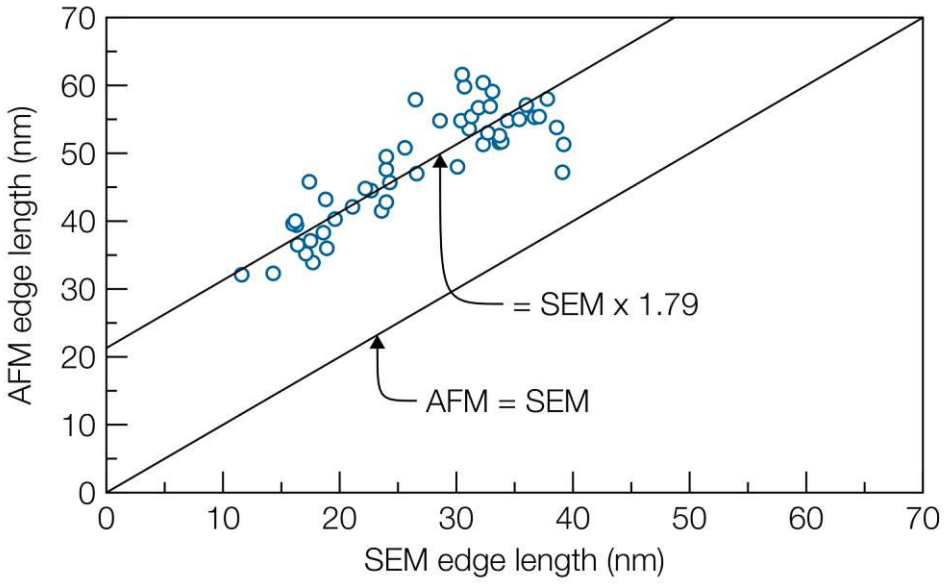

Figure 3.9: Comparison of the edge lengths between AFM and SEM measurement. The AFM edge lengths appear bigger by a factor of 1.79.

Results for Xe^{32+}

The Xe^{32+} irradiation was performed with a lower applied fluence of 510 ions/μm^3 compared to the other charge states. This was due to a beam drift caused by pressure instabilities and subsequent thermal instabilities in the NIELS setup. The kinetic energy of this irradiation was 180 keV. Despite the lower fluence, about 36 % of the nano-islands were hit due to the irradiation when evaluated with the program for the number of hit Au nano-islands. The blue histogram in figure 3.10 is shifted towards lower heights by a factor of approximately 36 % with regards to the yellow histogram. Therefore, the simulation and the experiment is in agreement. This figure illustrates the height loss for this charge state too and amounts (1.4 ± 1.2) nm.

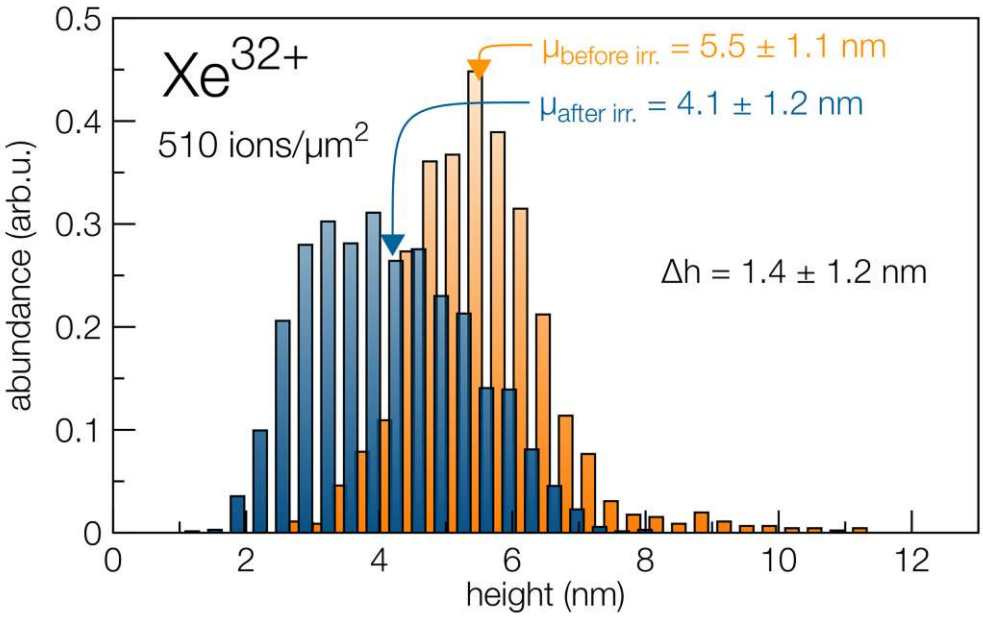

Figure 3.10: Result for the Xe^{32+} irradiation. The histogram shifts towards lower heights.

In figure 3.11 (a) and figure 3.11 (b) the non-irradiated and irradiated AFM images are shown, respectively. Figure 3.11 (b) may seem brighter, meaning higher islands, but they appear also bigger caused by the tip artefact. Another point may be the evaluation software, that levels the surface a bit differently for image artefacts of the AFM. A too high setpoint, integral gain or scan speed can influence the measurement and evaluation in terms of worn AFM tips.

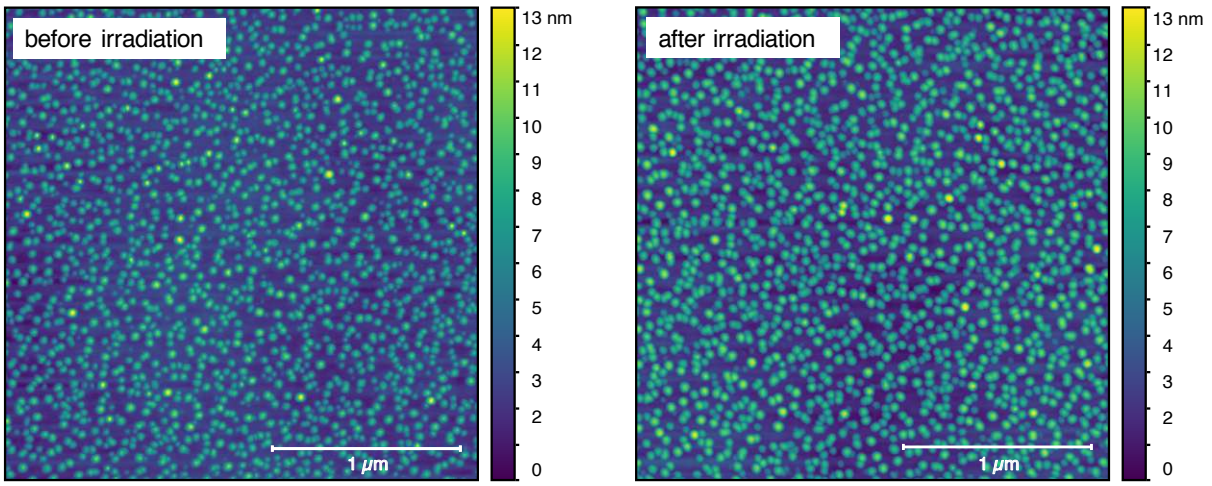

(a) (b)

Figure 3.11: In (a) the AFM image before the irradiation with Xe^{32+} is shown. In (b) after the irradiation. The different contrast is due to AFM artefacts and (surface) leveling of the software.

Results for Xe^{40+}

This irradiation series was performed by my colleague Gabriel Szabo in his diploma thesis [47]. This irradiation has the highest potential energy of 38.5 keV and was performed in our group. Figure 3.12 represents the height loss due to the irradiation and yields the highest amount of height loss of (2.3 ± 2.4) nm. The volume distribution of this sample was rather high and the maximum volume amount about 35.000 nm^3. The other samples have volumes of maximally 15.000 nm^3. The comparison between these mean values for the volumes can be seen in figure 3.13, whereas the Xe^{40+} is outstanding for the mean volume and deviation.

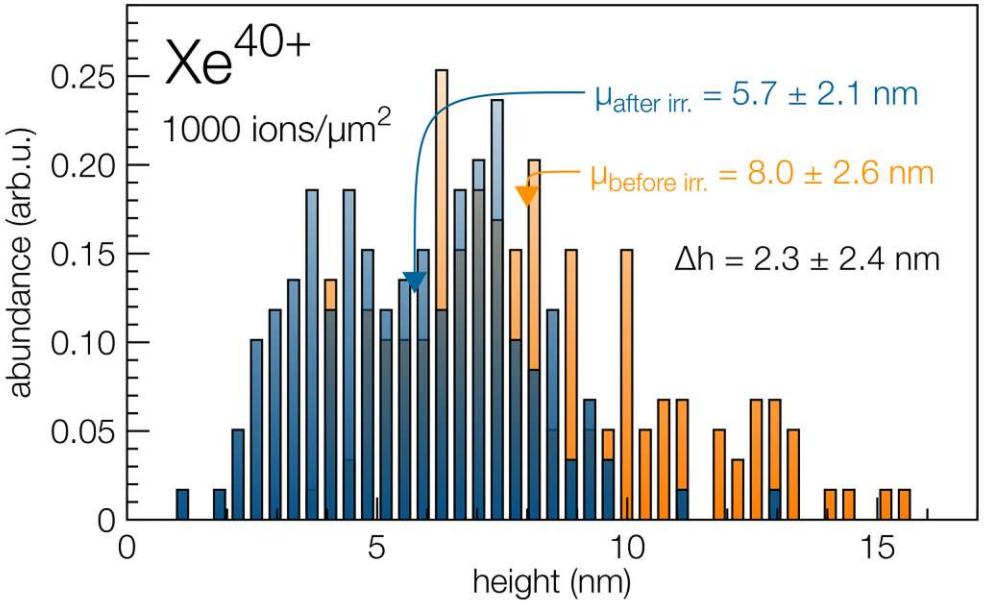

Figure 3.12: Histograms of the Xe^{40+} irradiation.

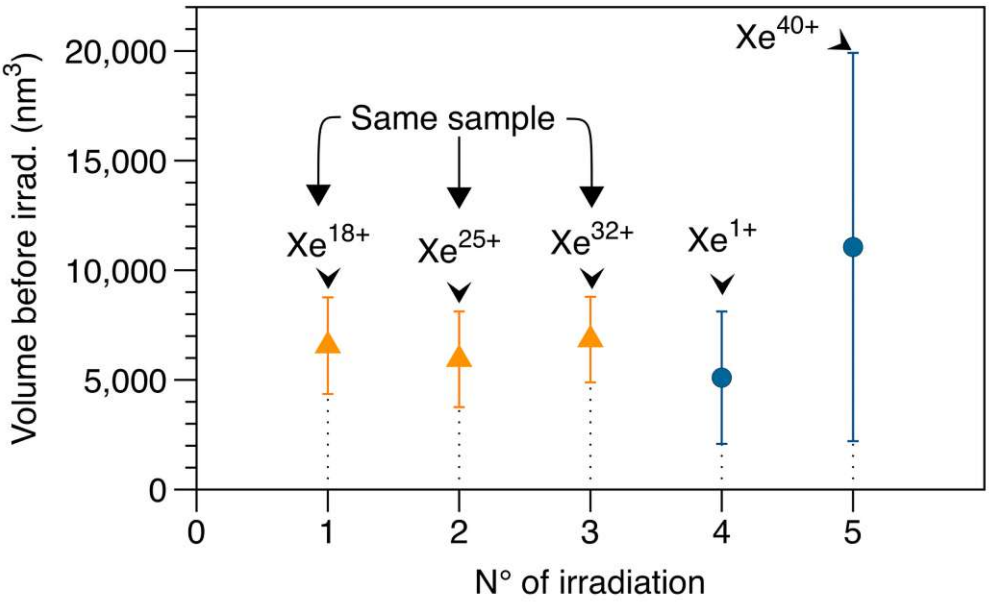

Figure 3.13: Comparison of the volume between the irradiations. The Xe^{40+} has a very high standard deviation, due to large islands found with low abundance and the bigger tip being used for this measurement.

Figure 3.14 represents the outcome of this experiment, where the mean height loss over the potential energy of the HCI is shown. The data fits an increasing linear regression of the height loss, which is consistent with the observations made. The outstanding data point is the Xe^{25+} irradiation, that yields a too high height loss for the potential energy deposited in the Au nano-islands. The applied fluence was higher compared to the Xe^{32+} irradiation, resulting in more Au nano-islands that were hit due to the irradiation. In this way, more hit Au nano-islands were analysed with the software for evaluation and the mean value for height loss for this charge state gets larger. Another point that may influence the data for this irradiation is the height and volume distribution before irradiation, which are slightly higher than for the other charge states. A selection-bias might also influence the evaluation in terms of choosing more smaller nano-islands for the analysis resulting in a higher height loss, since smaller nano-islands seem to be more effected by the potential energy, which is represented by the one-to-one comparison. Although a selection bias was not found to exist within one evaluated AFM image, it could be decisive for a whole xenon irradiation when more than 2000 Au nano-islands were evaluated and not 100. The error bars are large, because not every nano-island was hit during the irradiation, but a charge state dependence can be observed.

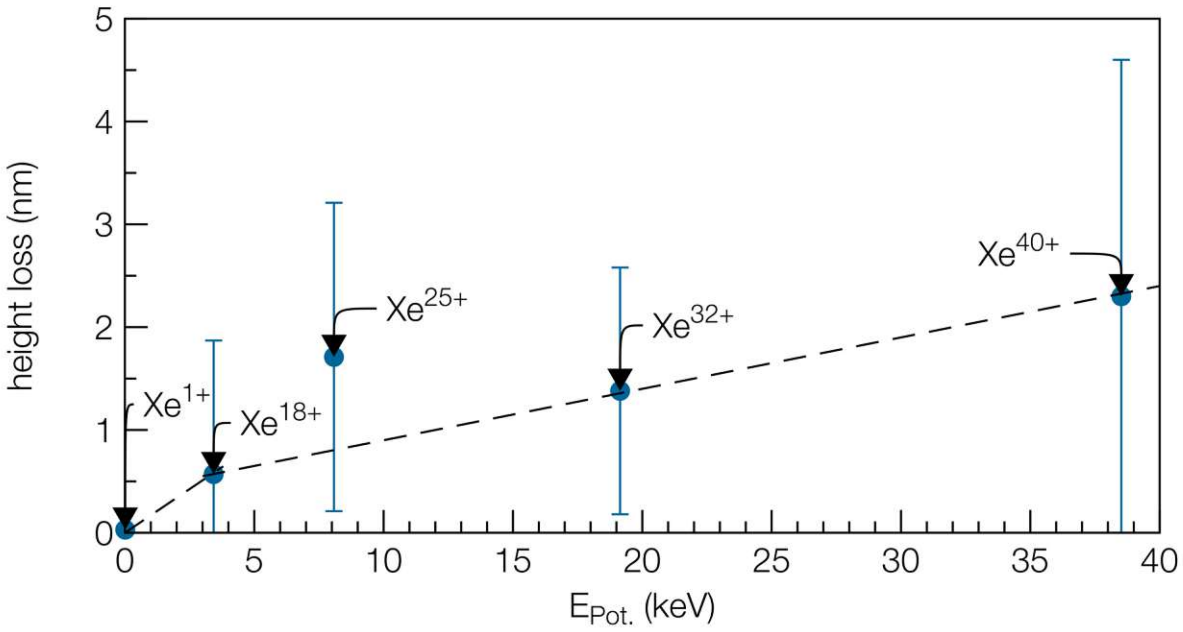

Figure 3.14: Measured height loss over the potential energy. An increase of the height loss is visible with increasing potential energy of the HCI.

The found height loss and the interaction of a slow HCI with a small confined metallic nano-islands is described as follows. The potential energy of the impinging HCI gets deposited in the first few layers [24] of the metallic nano-island, where the electronic subsystem gets excited. Although electronic processes occur on a faster timescale, the excited electron system „stores“ the potential energy long enough to couple to the lattice. Additionally, the kinetic energy of the HCI gets transferred to the lattice via elastic ion-nuclei scattering and results in heating and sputtering. A simulation of the range of the ion and the transferred energy to recoils can be seen in figure 3.15 (a) and figure 3.15 (b), respectively and was simulated with TRIM [13]. It was found that the nuclear stopping power can get enhanced by the potential energy of an ion by a factor of up to 3 [48]. Due to the combination of potential energy and kinetic energy effects and the cross-correlation between these, the nano-islands erode and a reduction in height can be measured.

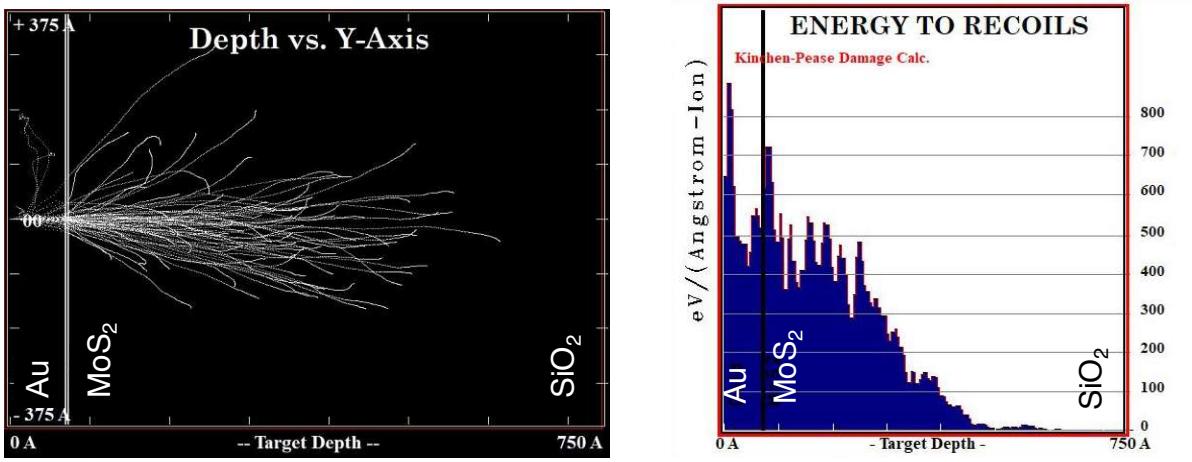

(a) (b)

Figure 3.15: In (a) the trajectories of 180 keV Xe in Au, MoS_2 and SiO_2 are shown. The mean projected range is 34 nm and the mean lateral straggle is 13 nm. In (b) the energy transferred to the recoils is shown. This simulation was obtained with TRIM [13].

3.2 Bismuth clusters on CaF_2 and SiO_2

The manufacturing process for the bismuth clusters was performed with a ultracold helium beam at the Universität Innsbruck by the group of Paul Scheier [42]. For this study, the substrates CaF_2 and SiO_2 were deposited with bismuth for 30 minutes and two hours, respectively. Both samples were pre-heated to remove residual particles on the surface before the samples were covered with bismuth. In the case of CaF_2, pre-heating causes a fluoridation of the surface, which was found to be more stable in ambient conditions [47].

The CaF_2 sample was irradiated with 190 keV Xe^{20+} and a fluence of 600 ions/μm^2. The irradiation of CaF_2 led to an estimated height loss of (0.3 ± 0.7) nm and can be seen in figure 3.16. The difference in height before and after irradiation is too small to be attributed to the potential energy of the ion and is linked to the uncertainty of the measurement.

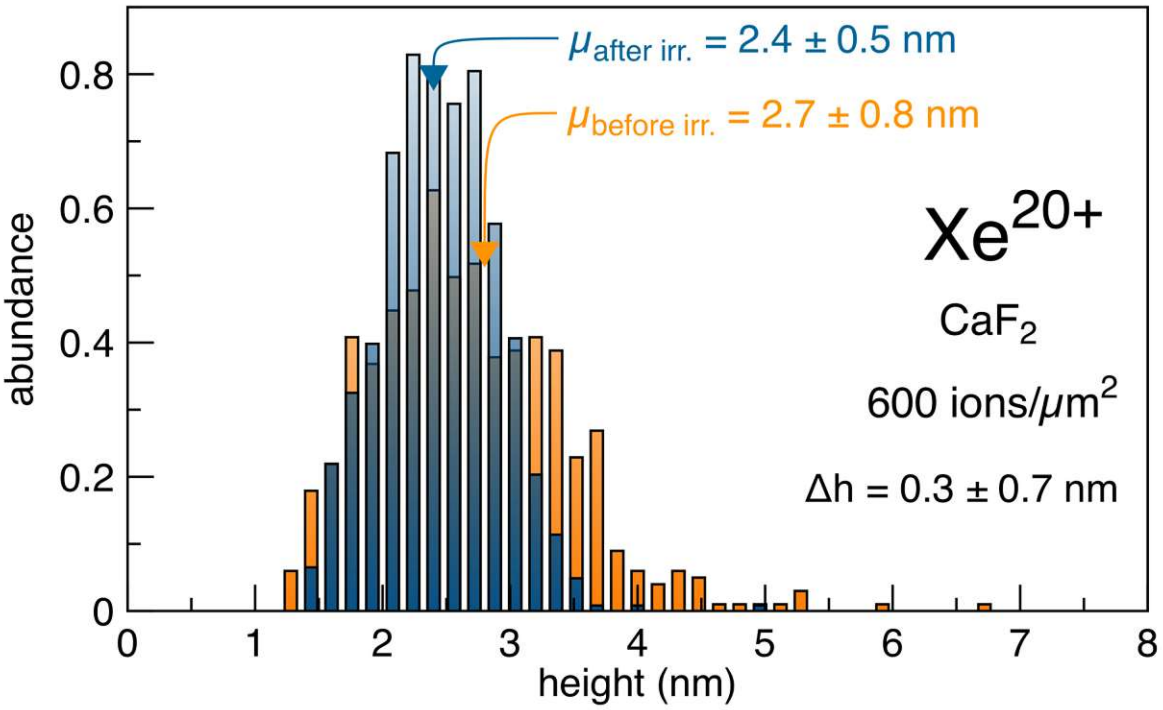

Figure 3.16: Comparing the height of the bismuth cluster before and after irradiation for the CaF_2 sample with 30 minutes deposition time of the bismuth clusters.

Figure 3.17 (a) and figure 3.17 (b) show the AFM images of the not irradiated and irradiated CaF_2 sample, respectively. The bismuth clusters are deposited in a very tight order, that may influence the dissipation of the potential energy of the ion, since they cluster together over larger areas. The size of the bismuth clusters appear bigger in figure 3.17 (a) due to a different field of view and a different standard tip was used. The tip radius determines the tip artefact, where the radius for this measurement was in the range of 7-12 nm.

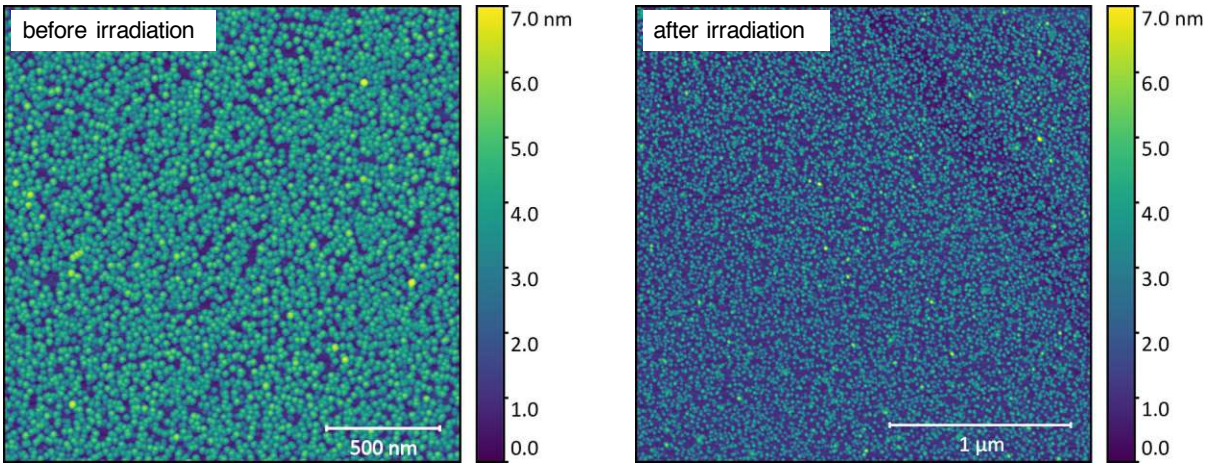

(a) (b)

Figure 3.17: In (a) the AFM image before the irradiation with Xe^{20+} is shown. In (b) after the irradiation.

The SiO_2 sample was irradiated with 200 keV Xe^{35+} and a fluence of 250 ions/μm^2. The difference in height for the SiO_2 sample amounts (0.3 $\pm$ 1.2) nm. The deposition time is higher than for the CaF_2 sample and the bismuth clusters on SiO_2 are about 500% bigger in their lateral size than the bismuth clusters on CaF_2, when figure 3.17 (b) gets compared with figure 3.20.

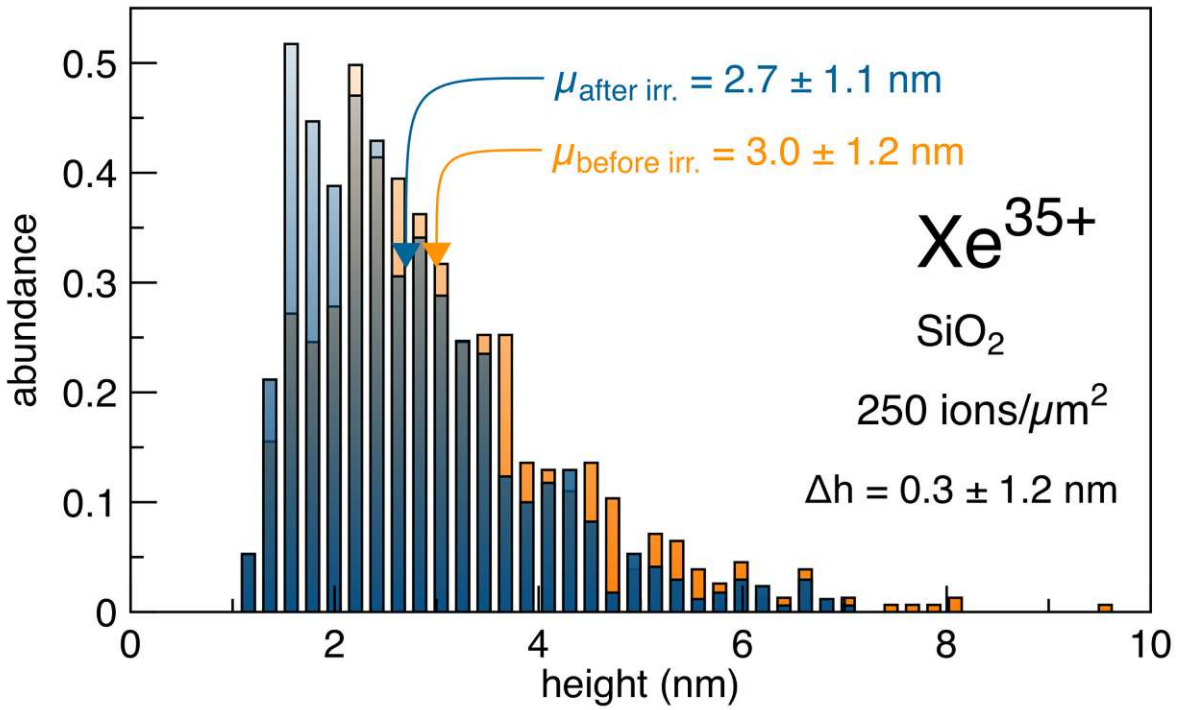

Figure 3.18: Comparing the height of the bismuth cluster before and after irradiation for the SiO_2 sample with two hours deposition time for the bismuth clusters.

Even though a higher charge state was used for this irradiation, the potential energy may not be enough to alter the bismuth clusters in regards of their height. Although the potential energy effect for the bismuth clusters is not visible for this sample, the nanostructuring of the substrate can be observed in figure 3.20, which indicates that an irradiated spot was measured. HCIs can cause nanostructuring of the surface of insulators and is well studied [6, 20]. By comparing the figure 3.19 before irradiation and figure 3.20 after irradiation, different structures between the yellow bismuth clusters can be seen and appear as bubbles with different heights. Although the fluence was not enough to create so many bubbles, they differ in their height between 2.2 nm and 0.9 nm in figure 3.20. The bubble-like structures with a height of about 2.2 nm might be due to the ion impact on the SiO_2 substrate that caused nano-hillocks, whereas the smaller bubbles with a height of 0.9 nm might be the surface roughness of SiO_2. The surface roughness before and after irradiation differs, because of a different tip that was used. Both images are obtained with AFM and the amplitude retrace signal was used to generate these images. The amplitude signal reflects the error in the feedback loop of the AFM. When the tip begins to scan the edge of an object, the amplitude changes and gets fed into the feedback loop and regulates it back to zero.

The amplitude signal acts as an topographical gradient detector. The higher the amplitude signal, the higher the gradient of the edge. Note that the height scale in an amplitude retrace does not reflect the measured „physical“ height of an object, it does only detect the deflection of the cantilever when the tip encounters an object.

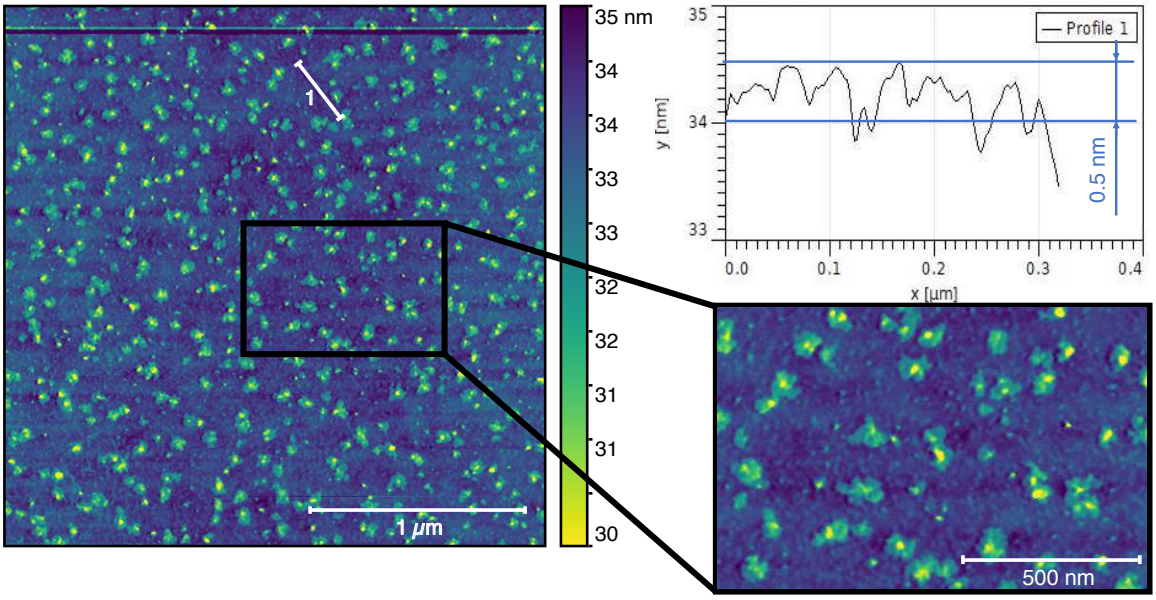

Figure 3.19: AFM amplitude retrace (AR) image of the not irradiated SiO_2 sample with two hours deposition time. The right upper image is a surface analysis of the white profile line „1“. The lower right image is a zoomed-in image of the black rectangle.

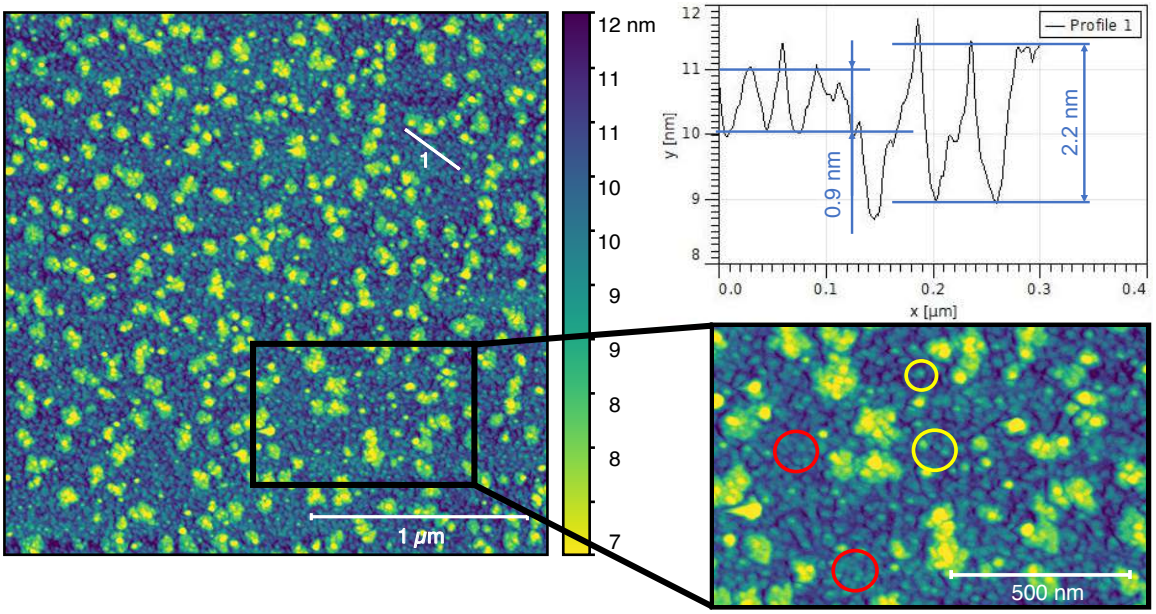

Figure 3.20: AFM (AR) image of the SiO_2 sample. The upper right image is a surface analysis of the white profile line „1“. The lower right image is the zoomed-in image. The yellow circles mark the bubbles with heights of about 2.2 nm and the red circles mark the smaller bubbles with 0.9 nm.

3.3 Latent tracks in TiO_2 and Al_2O_3

The second part of this thesis was to determine the damage profile of SHIs in insulating targets. The idea was to determine the length, where the ion strips off electrons until the equilibrium charge state is reached and the stopping power is enough to produce a latent track in the substrate. The distance at which this occurs may be measured by using various TEM techniques. For this purpose several samples and two different materials were investigated.

23 MeV I^{6+} on TiO_2

The first goal was to achieve settings for the TEM at which latent tracks can be observed. For this purpose AFM images of the different samples were obtained and a sample was chosen, where hillocks can be seen clearly. Figure 3.21 (a) represents the AFM measurement and in figure 3.21 (b) hillocks with about (0.9 to 1.3) nm in height can be seen.

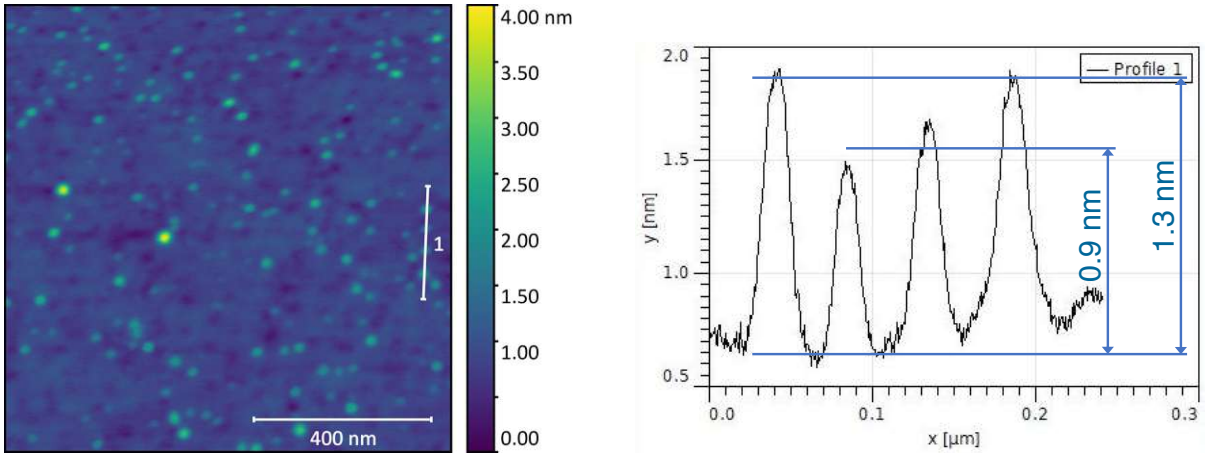

(a) (b)

Figure 3.21: In (a) the AFM image of the TiO_2 sample is shown, which was irradiated with 23 MeV I^{6+}. In (b) the evaluation of the line profile „1 “of image (a) is visible.

The next step was the preparation of the sample with the FIB milling machine. An area was chosen and a carbon protective layer was sputtered on top of the surface. The next step was to set up the dimensions of the lamella and the first milling process started. The dimension can be seen in figure 3.22 (a). The lamella was finally cut out of the sample and attached on a TEM grid, where the thinning process started. The finished lamella must be suitable for the investigation with TEM and must not exceed a thickness of a few hundred nanometers, to transmit the electron beam without too many undergoing inelastic processes. The finished first lamella with different thicknesses can be seen in figure 3.22 (b). Additionally, the carbon protective layer and TiO_2 substrate is shown.

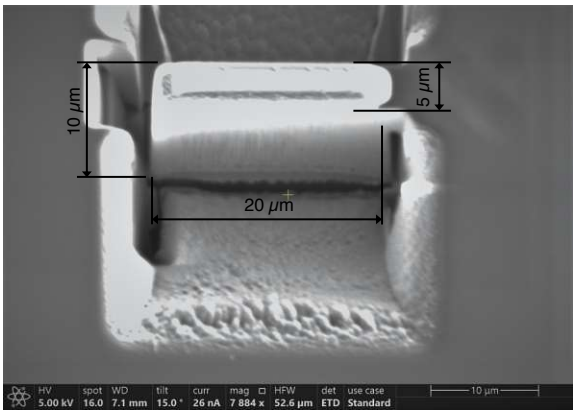

(a)

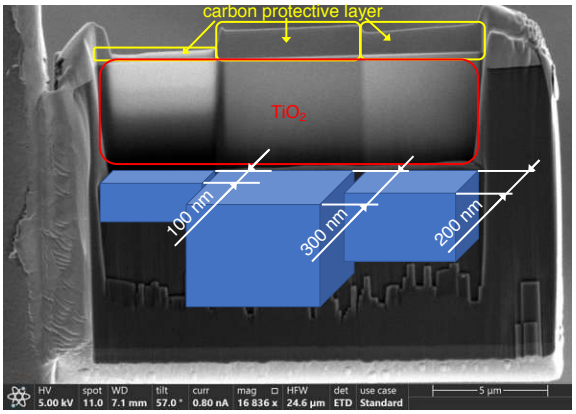

(b)

Figure 3.22: In (a) the dimensions of the lamella before the thinning process can be seen and in (b) the finished lamella, which was then put into the TEM.

The lamella was put into the TEM and the latent tracks were found with HR-TEM at the thinnest subarea with 100 nm thickness. The damage profile of the SHI below the surface has a conical shape and on top of the surface a hillock is located. The tracks found can be seen in figure 3.23 marked with yellow ellipses. Although a nano-hillock is located on top of a latent track, only the track can be seen, because of different values for the objective lens.

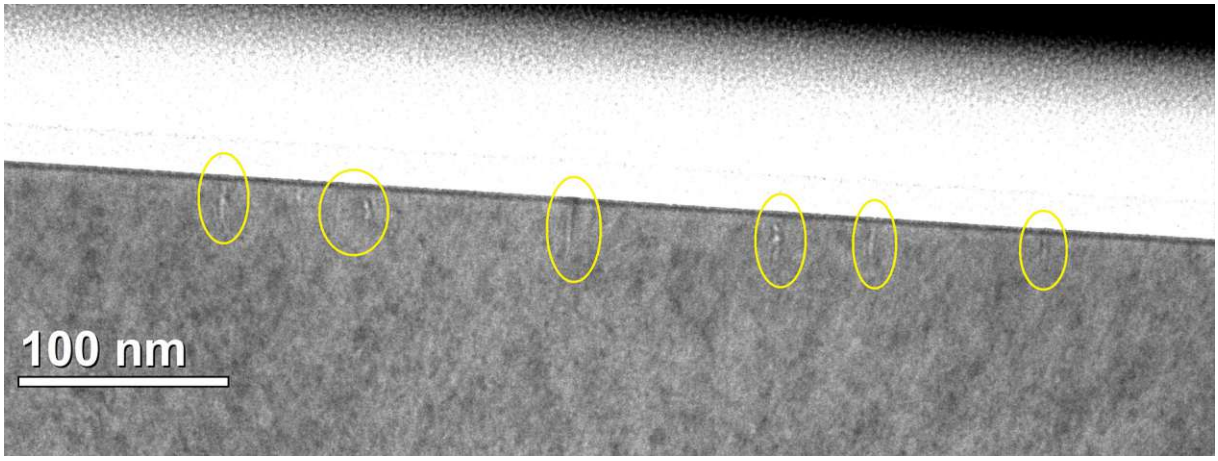

Figure 3.23: Tracks found with HR-TEM and marked with yellow ellipses.

Figure 3.24 represents the dimensions of the latent tracks, which amount to (20 - 30) nm in length and about (1.5 - 3) nm in diameter.

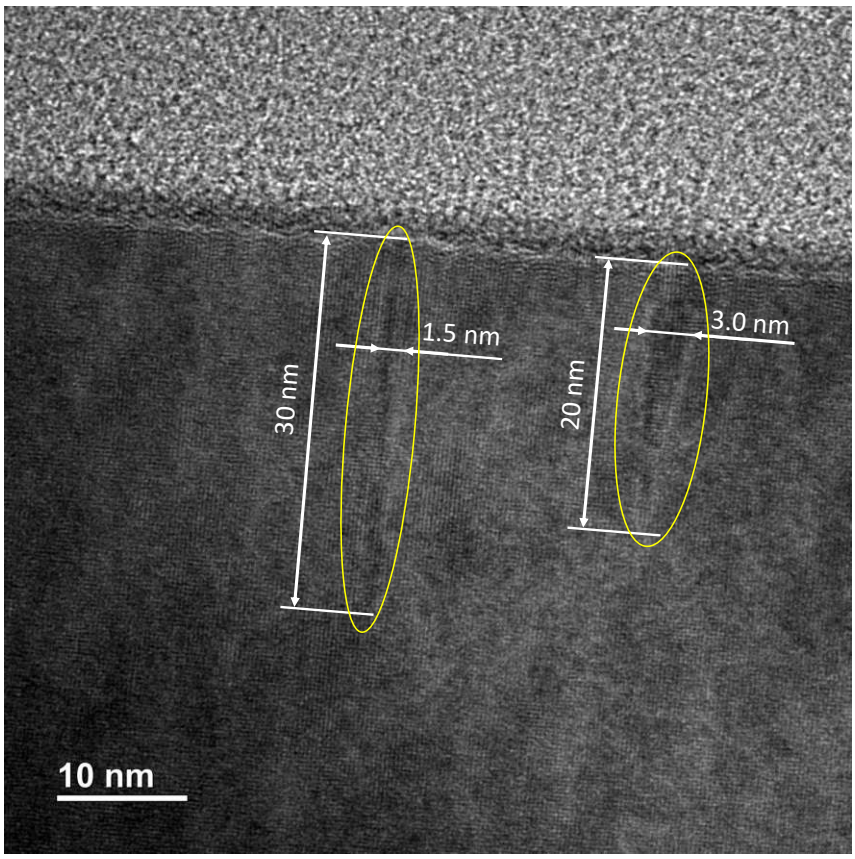

Figure 3.24: HR-TEM image of two latent tracks marked with yellow ellipses. The upper part of the image represents the (amorph) carbon protective layer, whereas the lower and darker part of the image illustrates the substrate.

The next step was to visualise the discontinuous part of the track, that begins after the conical shape and reaches micrometer deep into the substrate, which was simulated with SRIM [17]. For this purpose different TEM techniques were used, since HR-TEM was not sufficient enough. The lattice may have undergone a transition from rutile TiO_2 to amorphous TiO_2 and this may be measured in the bandgap of the two different lattice structures. Electrons in the valence band can be excited, allowing transitions into the conduction band by overwhelming the bandgap and they can be excited with an electron beam and the de-excitation happens via photons in the UV wavelength region. The cathodoluminescence method was used for this purpose, but no significant differences in the spectrum were observed. Since the detection threshold of the detector is limited at 300 nm and the wavelength of the emitted photons is also in this region, the signal can not be distinguished form the background to get valuable results.

After the HR-TEM imaging and cathodoluminescence technique, STEM was used as imaging method. The focused electron beam interacts with the sample and by adjusting the camera length of the TEM, different physical mechanisms, such as elastic and inelastic scattering, can be selected. The higher the value for the camera length, the more elastic processes are detected, e.g. Rutherford scattering for mass-to-thickness ratio or Z-contrast. The latent tracks of the SHI were not visible in normal STEM mode and as a consequence, the position of the track was saved by using HR-TEM mode.

Figure 3.25 and figure 3.26 use the bragg diffracted electrons at different camera lengths, at 200 mm and 680 mm respectively. No tracks were visible in these two images. This may be due to the small volume the latent track occupies compared to the thickness of the lamella, or because a strong defocus of the objective lens is needed like in HR-TEM.

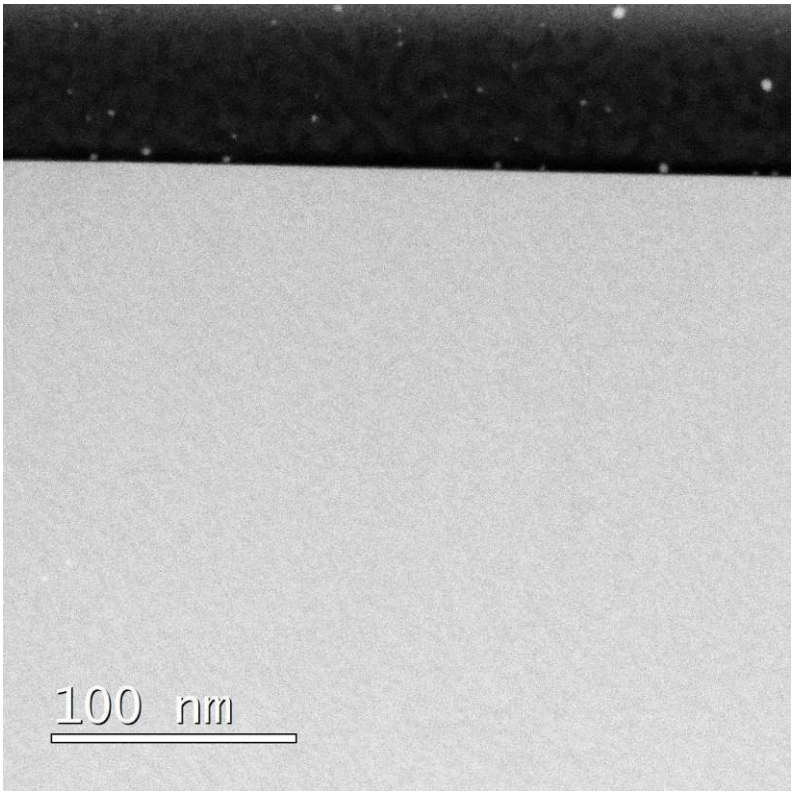

Figure 3.25: Bragg contrast in STEM mode. The camera length amounts 200 mm, collecting only a few bragg diffracted electrons at a small angle on the detector.

The Z-contrast is the next imaging mode, or camera length, that was used to visualise the latent tracks. The image can be seen in figure 3.27. The Z-contrast is proportional to the atomic number of the atoms in the measured area and is given by (2.3). This ansatz may measure the implanted iodine ions in the latent track, but unfortunately no track was visible.

The last contrast method that was used in STEM mode, was the dark field (DF) imaging mode. This mode uses the inelastically scattered electrons for imaging and the unscattered fraction of the electron beam gets cancelled out. This is achieved by switching the area of the detector in STEM mode and the dark field image appears. In figure 3.28 the latent tracks can be seen on the left side of the image, marked with a white ellipse. Even though this technique was able to visualise the latent track, the discontinuous part still remained unseen.

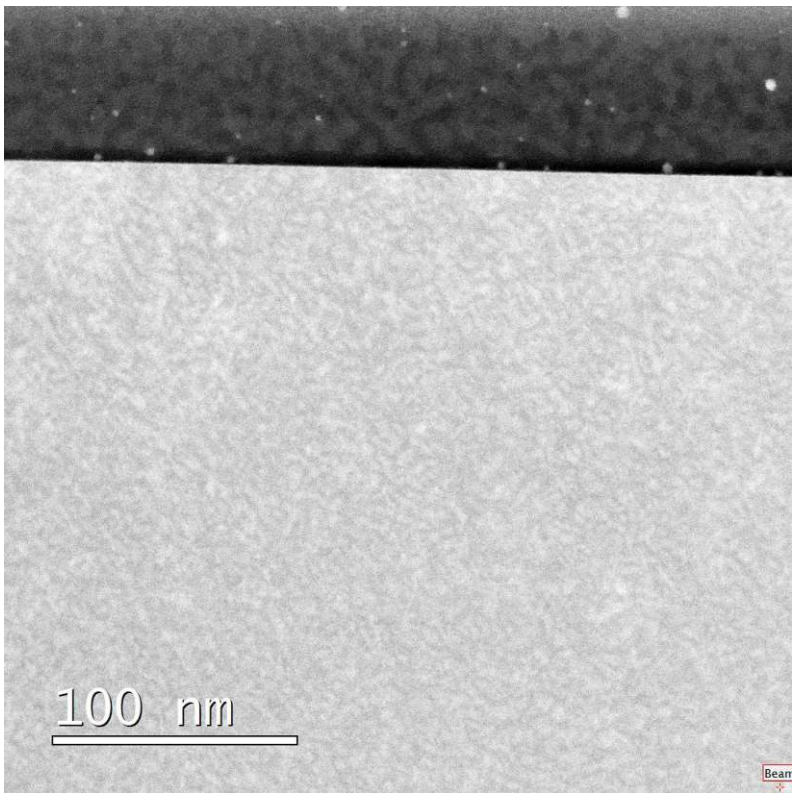

Figure 3.26: Bragg contrast in STEM mode with a camera length of 680 mm. Although more bragg diffracted electrons at a wider angle are collected, no difference can be observed.

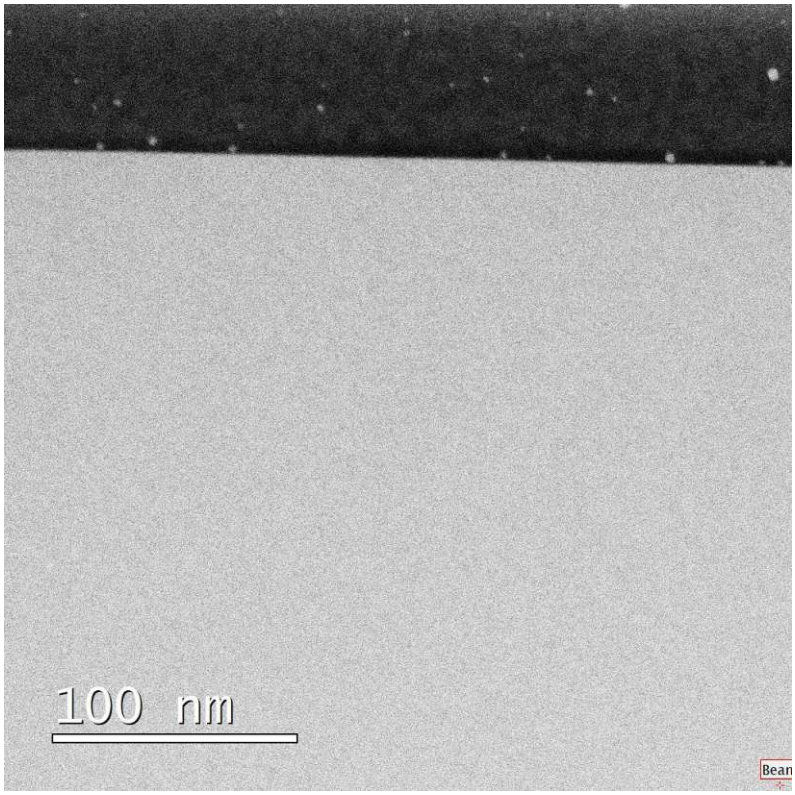

Figure 3.27: Z-contrast in STEM mode. This setting collects elastically scattered electrons (Rutherford) and the signal is proportional to the atomic number.

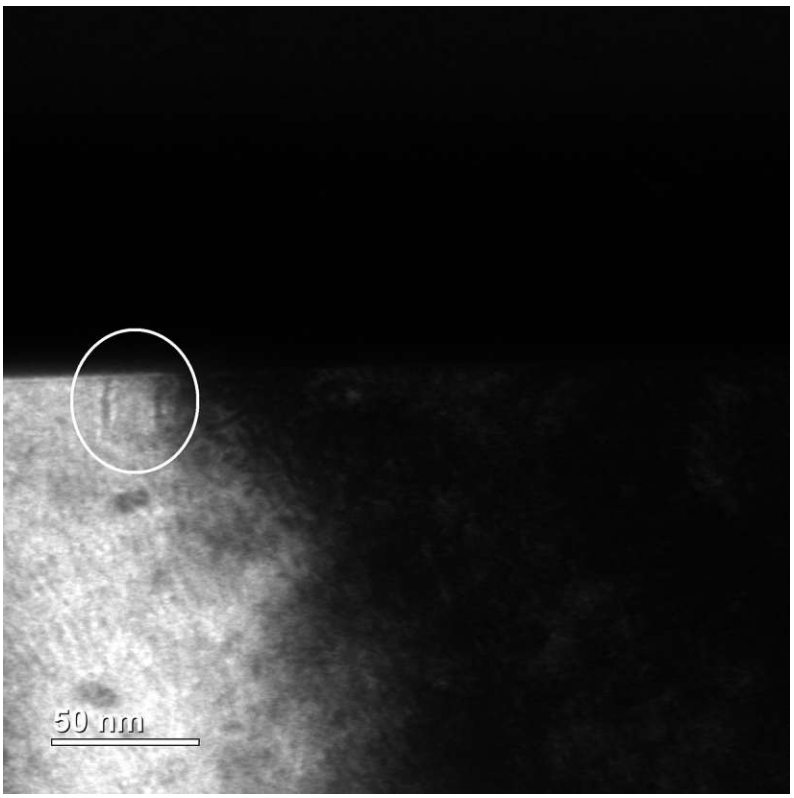

Figure 3.28: Dark field image, where the tracks can be seen inside the white ellipse.

The different imaging methods of TEM and STEM were able to visualise the track partly, but the discontinuous part was still unseen. As next step, another spectroscopy method of TEM was used, namely electron energy loss spectroscopy (EELS). This method is used in STEM mode, so the location of the tracks had to be approached like mentioned above.

For EELS two different tracks were measured that can be seen in figure 3.29, with the left track examined first. The zero-loss peak (ZLP) region of the EELS spectra does not deliver useful information, but the plasmon excitation and energy loss near edge structure (ELNES) may be able to visualise differences between the track and the substrate in the EELS image. Another reason why the ZLP was not used is because only elastically forward scattered electrons at a very small angle are detected and they do not provide any useful information about the interaction inside the specimen. The plasmon excitation represents the electronic structure of the sample and small differences can be measured. The ELNES region is used to determine the elemental composition of the specimen and one spectrum of this was evaluated, but no differences in the fine structure was found.

Additionally, two different selected area profiles were obtained, one vertically and one horizontally. The focused electron beam scans the selected area pixel by pixel and generates an image that contains the single and multiply excited plasmon peaks. These peaks were fitted with gaussian distributions and compared with each other, to visualise any differences in the image/spectra. An example of this plasmon spectra is given in figure 3.30.

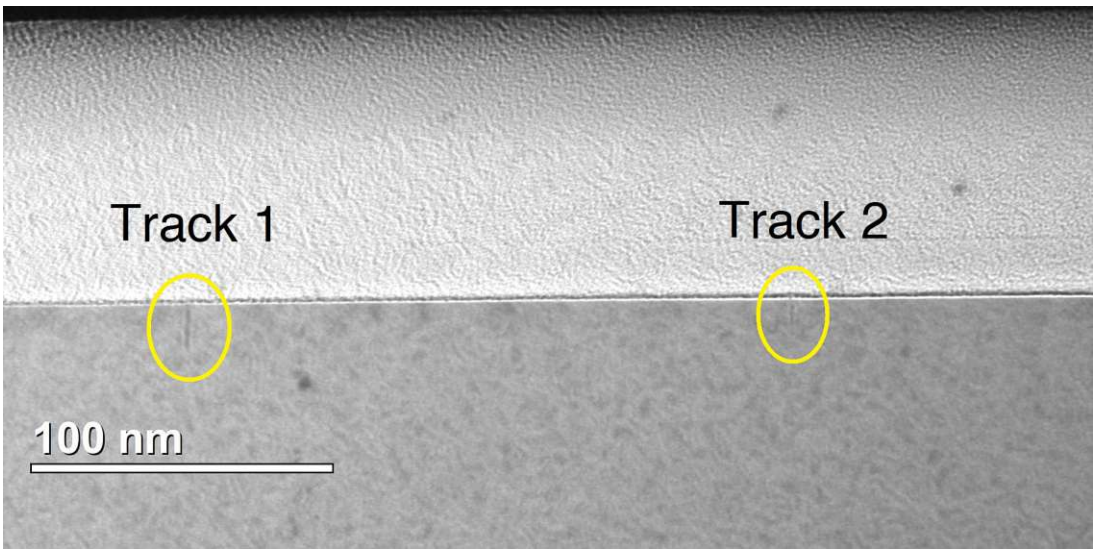

Figure 3.29: HR-TEM image of the two tracks, that are marked with yellow ellipses and that were investigated with EELS.

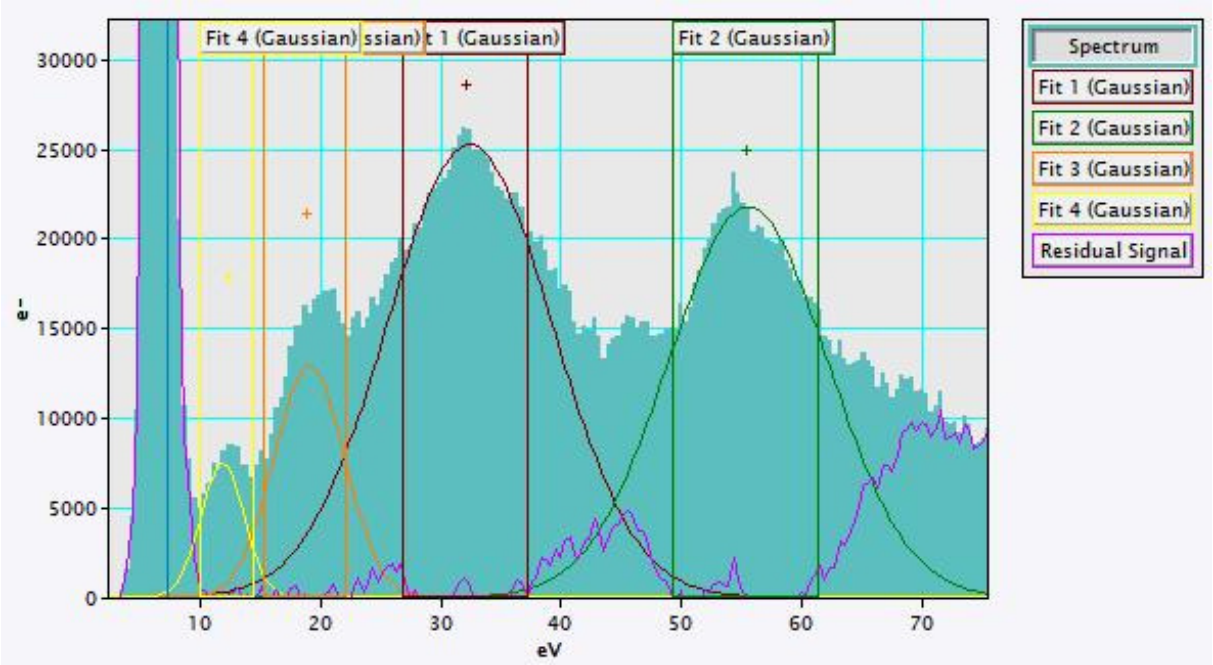

Figure 3.30: Plasmon spectrum with four fitted gaussian profiles. The y-axis represents the number of electrons and the x-axis the energy loss in eV. The first peak is the ZLP with the highest intensity. The first plasmon peak refers to the excitation of surface plasmons and is therefore smaller than the others. The other three peaks are multiply excited plasmons.

First, a vertical profile was selected in STEM mode, where the track was visible in HR-TEM. Figure 3.31 (a) shows the selected area profile around the latent track. Figure 3.31 (b) the corresponding plasmon spectra, where the highest gaussian peak was compared with the others and no track was visible. Figure 3.31 (c) is the high angle annular dark field (HAADF) image of the selected area. The track was visible in this image, but the discontinuous part was still not visualised.

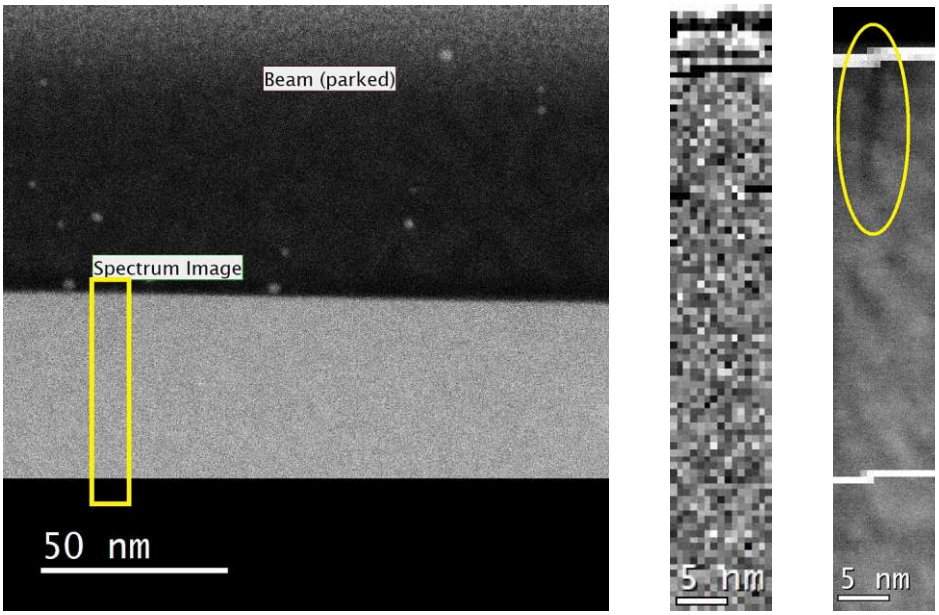

(a) (b) (c)

Figure 3.31: In (a) the selected area profile is visible as yellow rectangle. Figure (b) is the fitted and compared plasmon peak and don't show any track. In (c) the HAADF image is shown with the latent track inside the yellow ellipse.

The next step was to investigate a horizontal profile of the same track. The same approach was used to distinguish differences in the plasmon spectrum. Figure 3.32 (a) shows the selected area profile used for this experiment. In figure 3.32 (b) the evaluated plasmon spectrum of the EELS measurement is presented, but again no track is visible. The HAADF image of this area profile is shown in figure 3.32 (c) and shows the latent track marked with the yellow ellipse.

The next step was the investigation of the right track, that can be seen as „Track 2" in figure 3.29. Since this experiment shows the same results, it is presented only briefly. The same approach was used as for the left track. First, a vertical and then a horizontal area profile was used for EELS and the plasmon spectra compared and the HAADF image evaluated. Figure 3.33 (a) and figure 3.33 (b) show the latent track in the HAADF image, but does not show the discontinuous part.

The final conclusion of these measurements and evaluating the intensity of the HAADF signal in equation (2.3) gives the result, that the conical shapes of the tracks are voids. This can be concluded from the fact, that the HAADF signal is proportional to the thickness, density and atomic number. When the intensity is calculated next to a track and one time on a track, a difference of 3% in the density and thickness can be calculated. This results in the assumption that these tracks are voids, where no material is left inside.

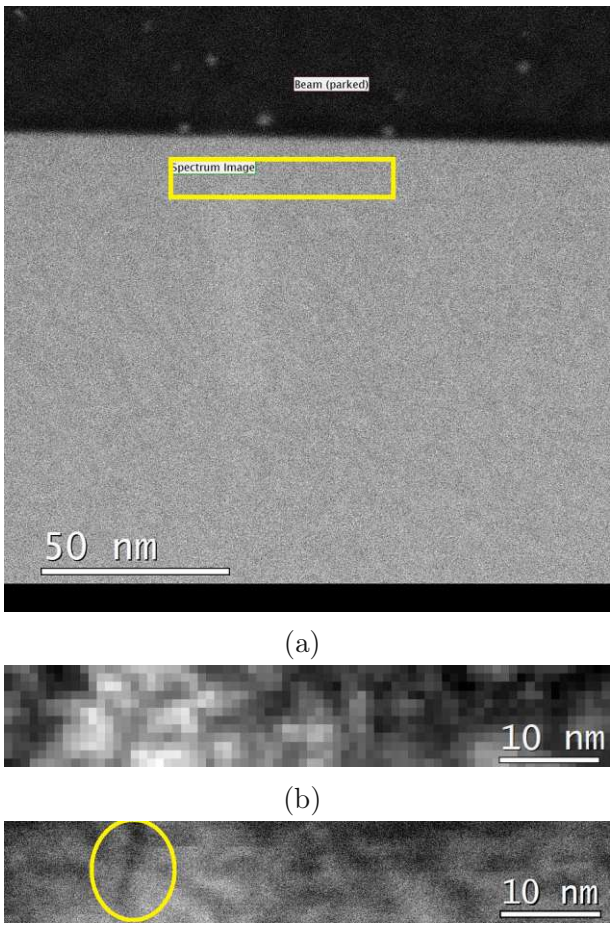

(a)

(b)

(c)

Figure 3.32: Investigation of the latent track with a horizontal selected area profile marked by the yellow rectangle in (a). In (b) the evaluated EELS spectrum and in (c) the corresponding HAADF image is presented, where the latent track is also visible inside the yellow ellipse.

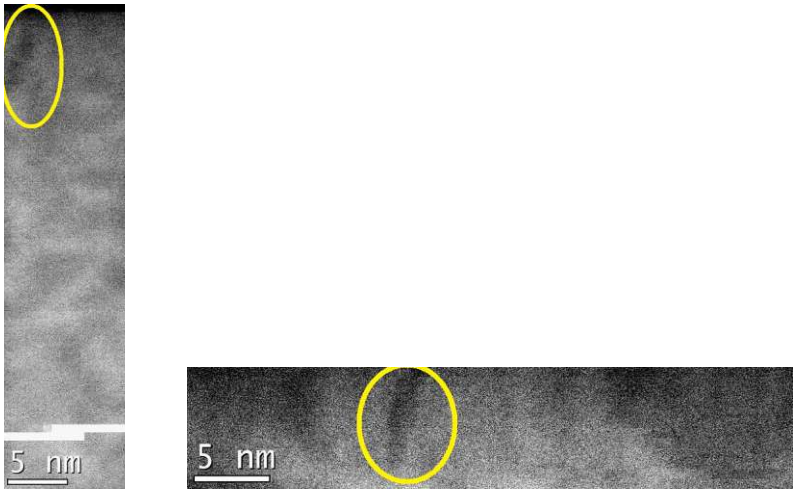

(a) (b)

Figure 3.33: (a) shows the HAADF image of the right track with a vertical selected area profile, whereas in (b) the horizontal area profile is shown. The tracks are marked with the yellow ellipses.

A simulation program was used to determine displacements of an HR-TEM image, where a track was located. The ion impact generates displacements of lattice atoms along it's trajectory, whereas these may be visualised with this software. Although no color scale was plotted, strong displacements and strains are blue and black, whereas the area where nothing happened is green. Figure 3.34 (a) and figure 3.35 (a) show the area, where the analysis was performed. The field of view amounts (44 x 44) nm and the location, where the track is located, is marked with the yellow ellipse. The displacements were calculated by the software in the x and y direction, that is represented by the figure 3.34 (b) and figure 3.34 (c), respectively. Although the track was visible in HR-TEM, no track can be seen in these images.

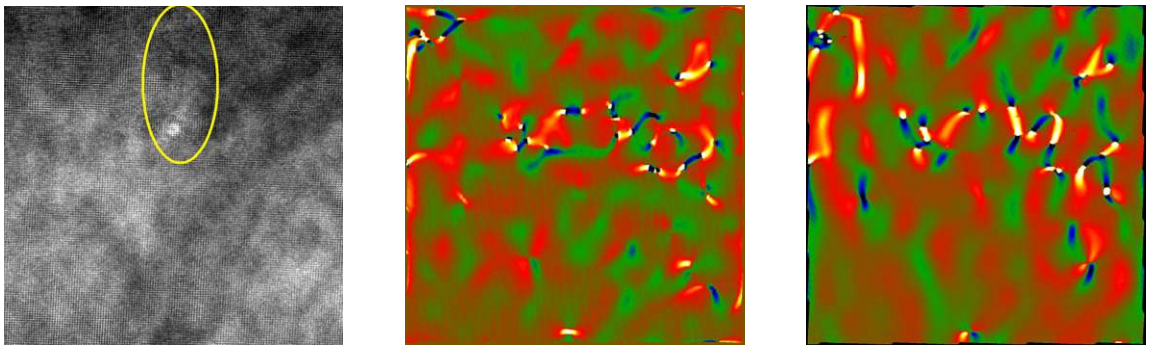

(a) (b) (c)

Figure 3.34: In (a) the area can be seen, where the displacements were evaluated. In (b) and (c) the displacement in x and y direction are shown respectively.

Furthermore, the heating around around the ion impact might leave lattice tensions behind, when cooled down and is represented by the strain tensor. The strain tensor in x and y direction was evaluated by the software and plotted and are shown in figure 3.35 (b) and figure 3.35 (c), respectively. No latent track was visualised with the evaluation of the stress. This might be due to the small volume the latent track occupies compared to the thickness of the lamella.

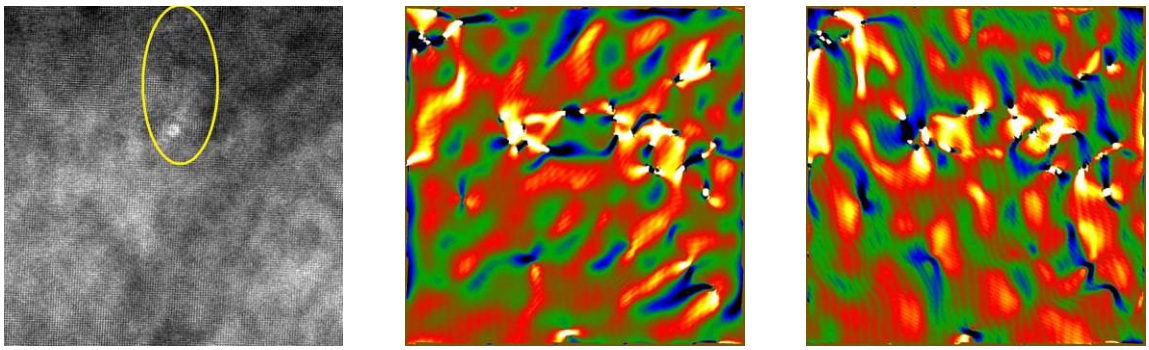

(a) (b) (c)

Figure 3.35: In (a) the area can be seen, where the strain tensor were evaluated. In (b) and (c) the stress in x and y direction is shown respectively.

13 MeV I^{8+} on TiO_2

The next sample has a lower kinetic energy of 13 MeV instead of 23 MeV and therefore a lower electronic stopping power. This was used, to get closer to the threshold where no latent track is created due to the kinetic energy, but the potential energy enhances the stopping power up to a point where damage is done to the substrate. For this purpose the 13 MeV iodine^{8+} sample was prepared with the FIB ion milling machine and a lamella was cut out for the investigation for TEM. The same approach was used for the 23 MeV sample. First, HR-TEM images with a strong defocus were used to visualise the latent tracks and then STEM/EELS was performed to distinguish differences in the plasmon spectrum and HAADF image.

Figure 3.36 (a) shows the surface topography obtained with AFM. The yellow dots indicate either nano-hillocks due to the irradiation, or contamination from the air after the irradiation. A line profile analysis was made with Gwyddion and is shown in figure 3.36 (b). The investigation with HR-TEM should clarify whether these dots are nano-hillocks or contamination.

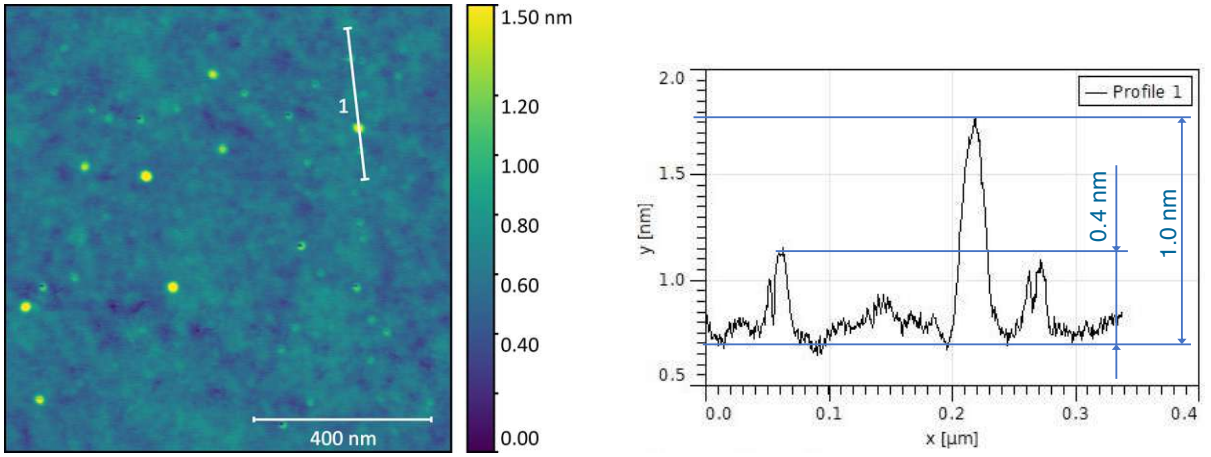

(a) (b)

Figure 3.36: In (a) the AFM image of the TiO_2 sample is shown, which was irradiated with 23 MeV I^{8+}. In (b) the evaluation of the line profile „1 “of image (a) is visible.

After transferring the sample into the TEM, the first high resolution images were obtained. The whole length of the lamella was investigated to find any latent tracks underneath the surface. In figure 3.37 a large field of view was used to visualise any inhomogeneities underneath the surface, but unfortunately no tracks were clearly visible. Figure 3.38 has a smaller field of view and atomic resolution may help to see latent tracks. In neither of these two images were latent tracks clearly visible, although they are only examples of a series of images. Although HR-TEM was not able to visualise the latent tracks, STEM/EELS was performed on a large area, where it was not clear, whether the sample drift caused distortion in the image, or there are latent tracks. Since HAADF images show the latent track, this method was also used after obtaining the EELS spectrum.

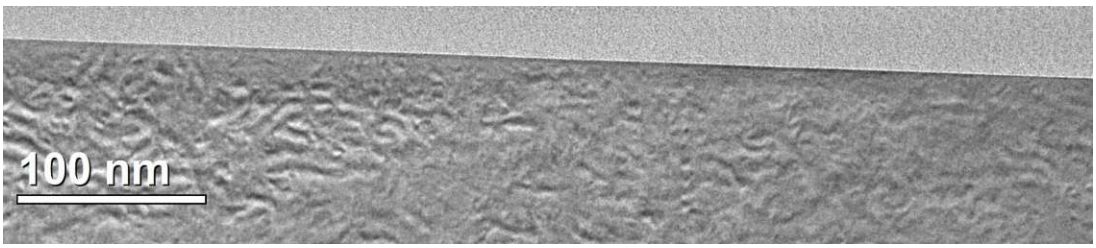

Figure 3.37: HR-TEM image of the 13 MeV TiO_2 sample with a large field of view.

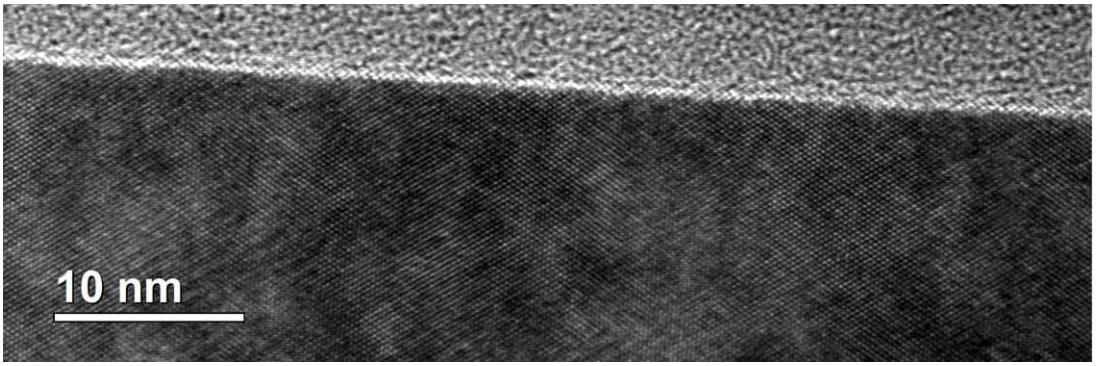

Figure 3.38: HR-TEM image with a small field of view to achieve atomic resolution.

In figure 3.39 (a) the rectangle shows the selected area profile and amounts 600 nm in length. Figure 3.39 (b) shows the corresponding plasmon spectrum, which is again compared with the other plasmon peaks to determine differences. Lastly, in figure 3.39 (c) the HAADF image of this area is presented, but unfortunately this method was also not able to visualise the latent tracks for this sample.

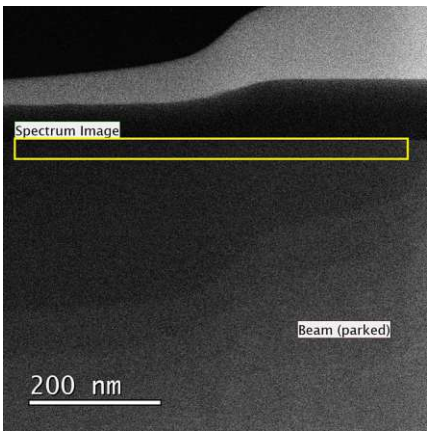

(a)

(b)

(c)

Figure 3.39: In (a) the yellow rectangle marks the area, where EELS was performed in STEM mode. In (c) the evaluated and fitted plasmon spectrum is shown and in (c) the HAADF image.

The last method used were the inelastically scattered electrons that are used to form the dark field image, since this method was also successful for the 23 MeV TiO_2 sample. Figure 3.40 and figure 3.41 show the dark field images of the 13 MeV sample. Also the dark field images show no latent tracks, although these two images are only examples of a series of dark field images obtained from the sample.

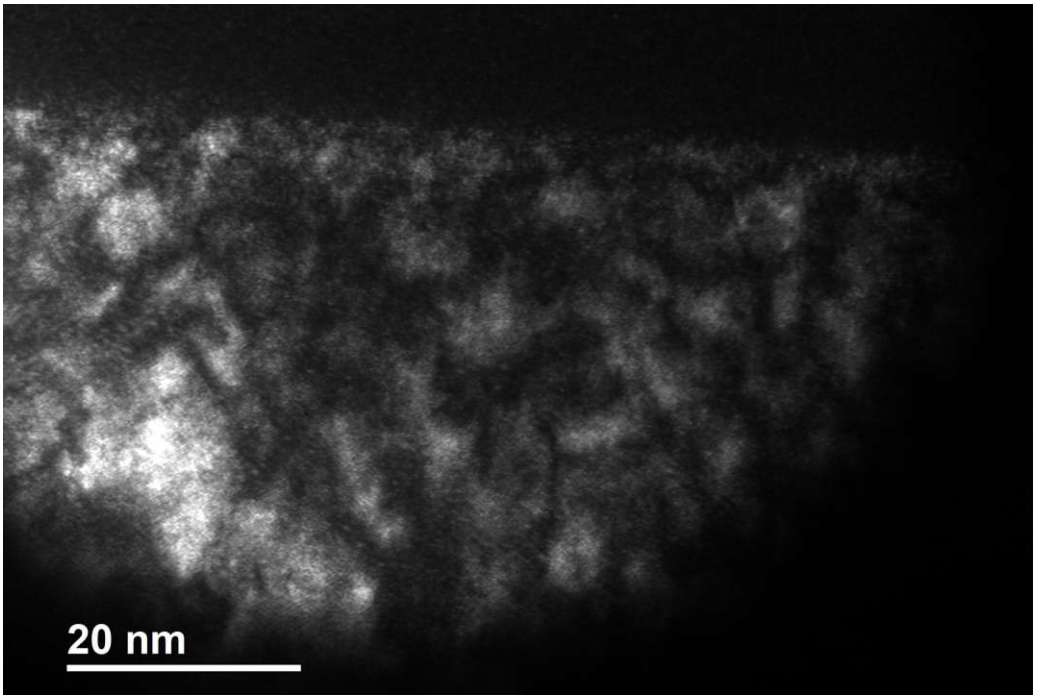

Figure 3.40: Dark field image of the 13 MeV sample.

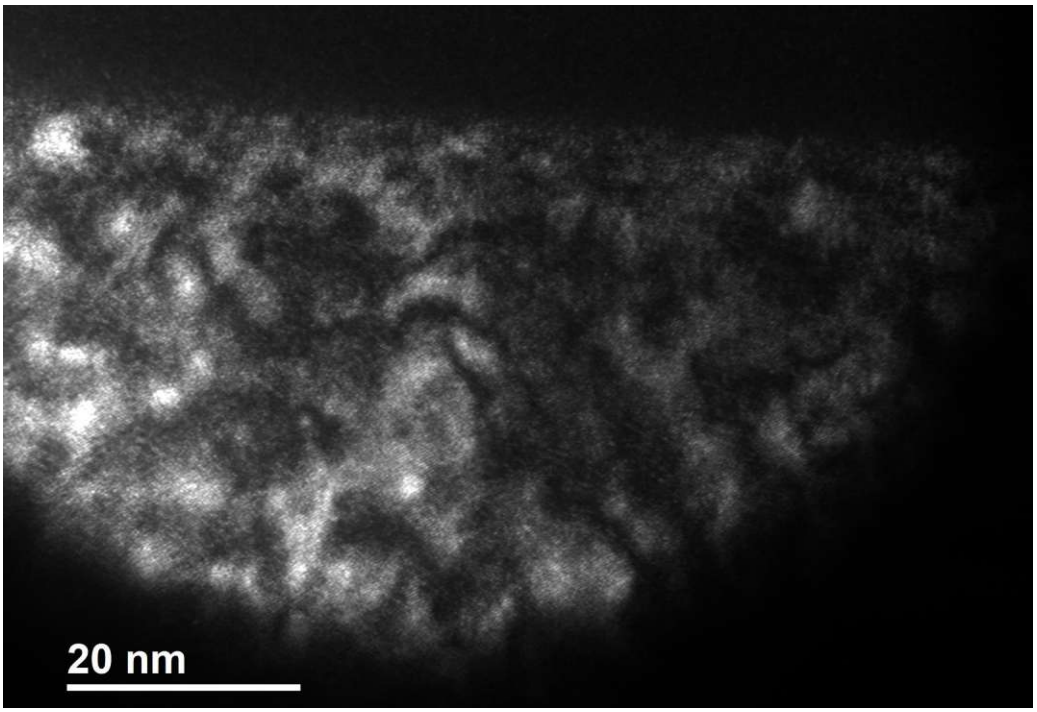

Figure 3.41: Dark field image on an other spot of the sample.

28 MeV I^{14+} on Al_2O_3

This sample was used as reference sample for the swift heavy ion irradiation experiments. Since the stopping power is material dependent, because of the amount of atoms the ion passes by, the value for aluminium dioxide (Al_2O_3) differs slightly. The electronic stopping power for 23 MeV iodine on TiO_2 amounts to 514.7 eV/Angstrom and for 28 MeV iodine on Al_2O_3 the electronic stopping power amounts to 510.3 eV/Angstrom. The more significant difference between these samples are the charge states used for irradiation. The TiO_2 was irradiated with 23 MeV I^{6+} and the Al_2O_3 with 28 MeV I^{14+} resulting in a difference of the potential energy of about 1.659 keV. Therefore, the irradiation of Al_2O_3 brings more potential energy in the surface near region and enhances the electronic stopping due to complex charge exchange mechanisms [21].

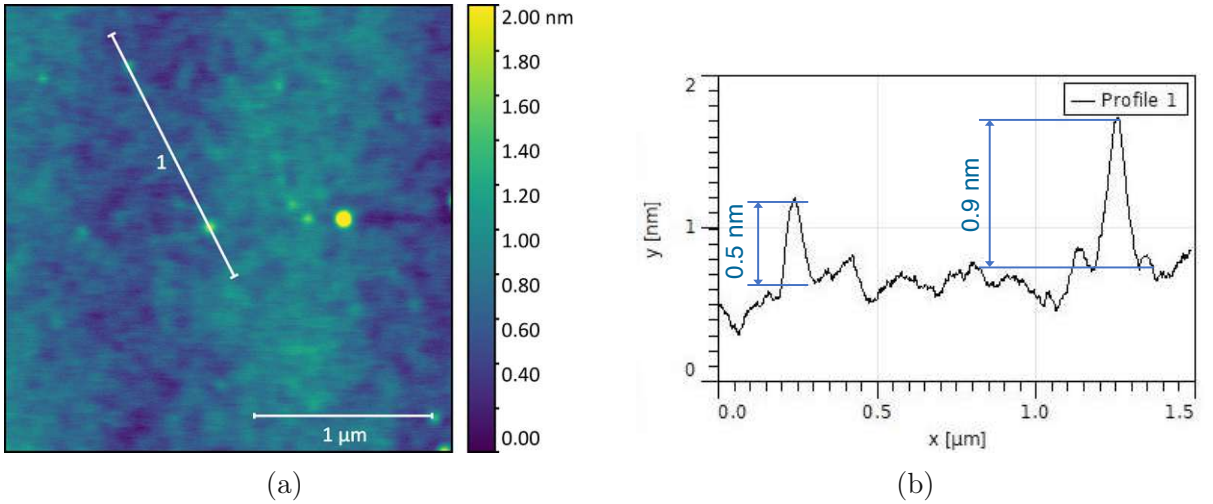

(a) (b)

Figure 3.42: In (a) the AFM image of the Al_2O_3 sample is shown, which was irradiated with 28 MeV I^{14+}. In (b) the evaluation of the line profile „1 “of image (a) is visible.

The preparation with the FIB milling machine was not as straight forward as for the TiO_2 sample, because the Al_2O_3 amounts to 9 on the Mohs scale, whereas TiO_2 amounts to 6. The Mohs scale refers to the hardness of a mineral. When the lamella gets thinned to about 50 nm, the internal stress bends the lamella and in the middle a hole appeared. We are interested in the surface near region, where no visible damage with SEM was seen, so the sample was put into the TEM and investigated with HR-TEM and STEM/EELS.

In figure 3.43 two tracks can be seen inside the yellow ellipses obtained with HR-TEM. The sample looks different than the TiO_2 and has no sharp interface between the carbon protective layer and the surface of the Al_2O_3. Maybe the sputter coater before the FIB milling, or the carbon layer deposition of the FIB machine was not successful. The lower half of the image contains unusual structures and may be due to the hole that appeared during the thinning process with the FIB machine.

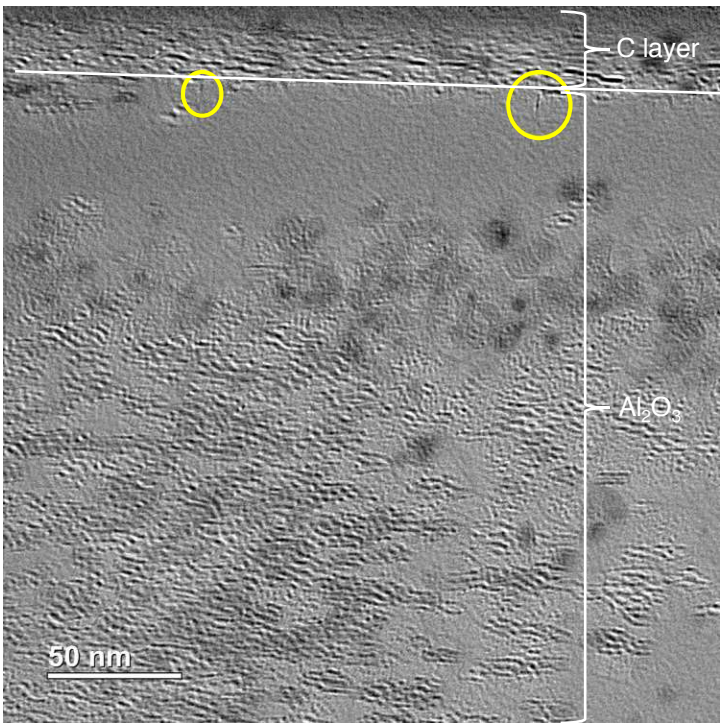

Figure 3.43: HR-TEM image of the Al_2O_3 sample. Two tracks can be seen in the upper part of the image, marked with yellow ellipses.

Another spot was found, where a track was suspected and can be seen in figure 3.44. An EELS measurement coupled with the HAADF image should verify this assumption, because a track this deep in the substrate may not occur, but as mentioned the interface between the carbon protective layer and the Al_2O_3 is not clearly visible. However, the difference between the carbon layer of the sputter coater and the FIB machine can not be observed in this image and the carbon and Al_2O_3 is not distinguishable with a sharp interface.

Figure 3.45 (a) shows the selected area profile, where EELS was performed. In figure 3.45 (b) the evaluated plasmon spectrum is shown, but no differences can be detected. Last, in figure 3.45 (c) the HAADF image of the EELS measurement is shown, but as no track can be seen with this technique it is unlikely that this is a track made from SHIs.

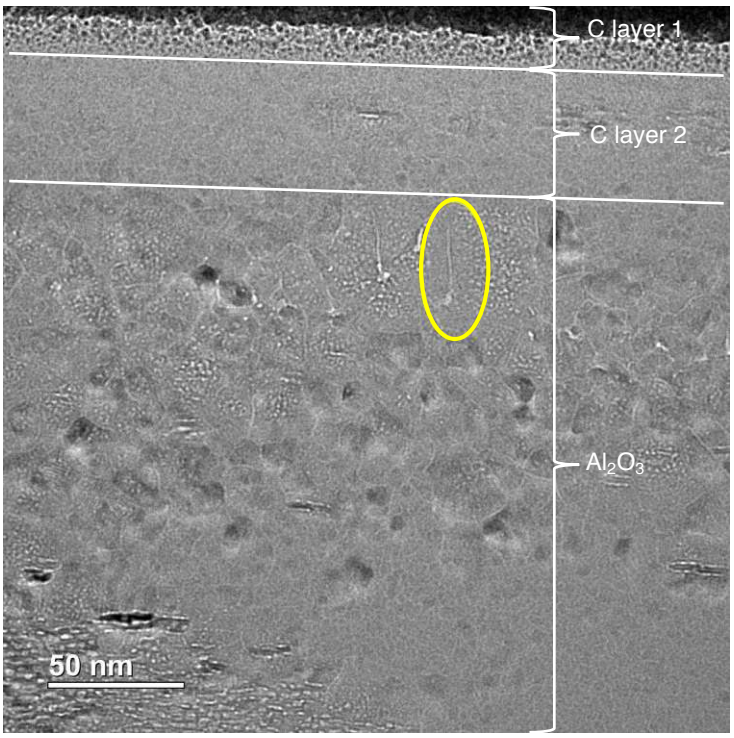

Figure 3.44: Another HR-TEM image, where a track is seen, but can also result from the tension of the lattice due to the thinning with the FIB. Two carbon protective layers are on top of the Al_2O_3 surface, one with high density and another one with lower density as protection for the thinning process.

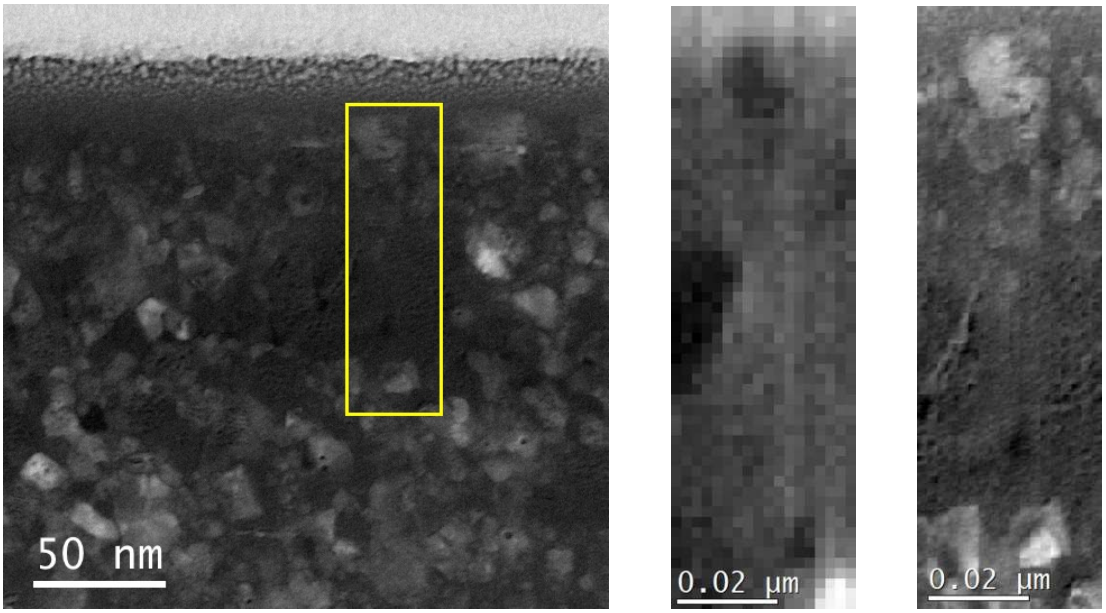

(a) (b) (c)

Figure 3.45: In (a) the yellow rectangle marks the area, where EELS was performed in STEM mode. In (b) the evaluated and fitted plasmon spectrum is shown and in (c) the HAADF image.

Additionally, dark field images in HR-TEM and HAADF images in STEM mode were performed and can be seen in figure 3.46 and figure 3.47, respectively. The yellow ellipses in figure 3.46 mark the spots, where tracks might be, but since they were not observed

with HR-TEM it can not be clearly determined that this are latent tracks. Additionally, the yellow line marks the interface between the carbon layer and the Al_2O_3 substrate and it is not a sharp line as for the TiO_2 samples.

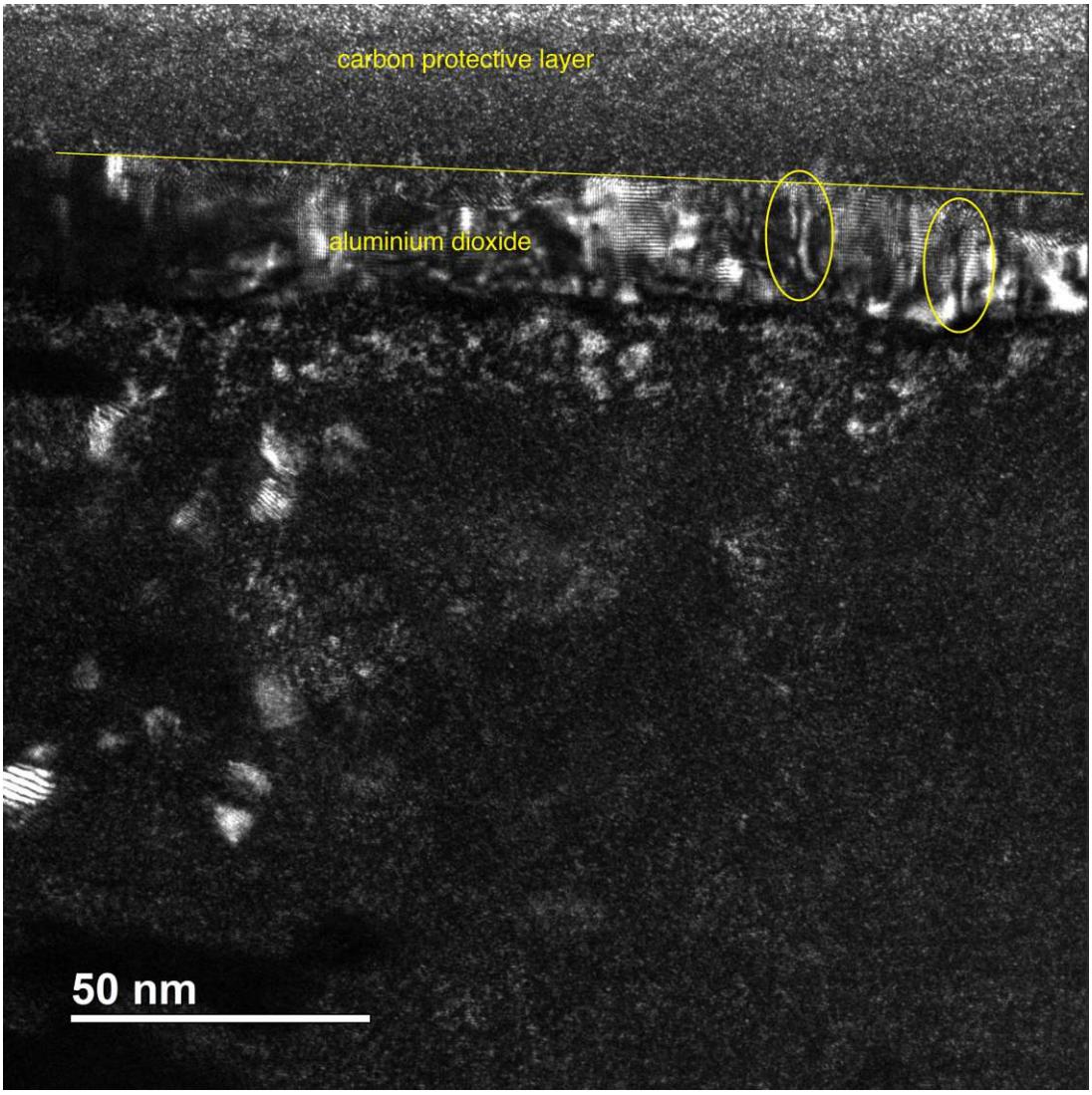

Figure 3.46: Dark field image of the Al_2O_3 sample. Due to the bad quality of the lamella and material, tracks are difficult to recognise or to qualify.

Lastly, in figure 3.47 the HAADF image in STEM mode can be seen, where elastic scattered electrons at wide angles are collected on the detector. This image shows a larger area, but is not as sensitive as the HAADF image used in EELS. Unfortunately, no meaningful conclusion can be made from this image, because the lamella was not well suited for TEM.

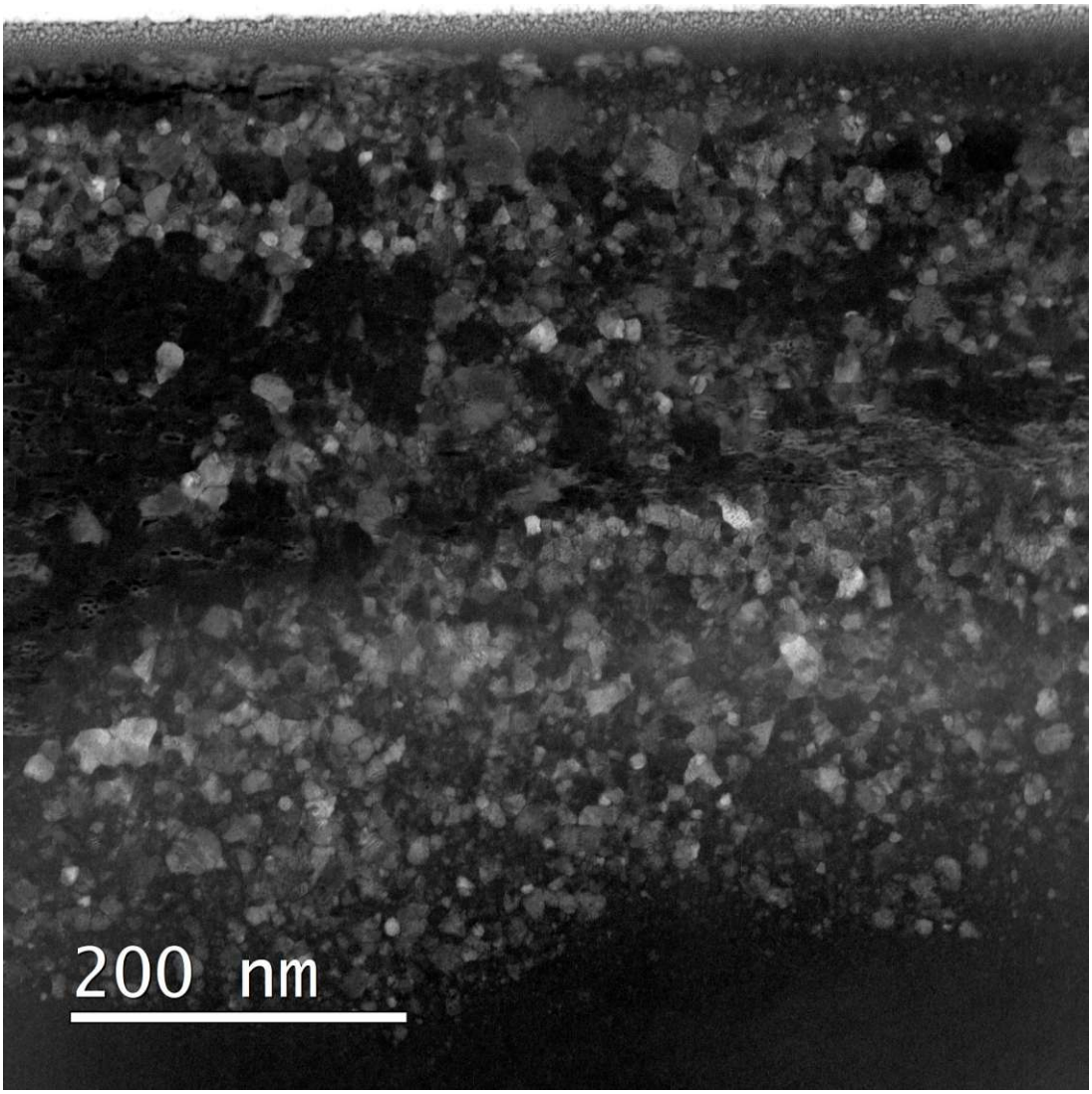

Figure 3.47: A HAADF image performed in STEM mode, that shows a bigger area than with EELS.

4 Conclusion and outlook

In this thesis two main applications of ions were investigated. On the one hand, slow HCIs were used to alter Au nano-islands on a MoS_2 monolayer and on the other hand, SHIs were used to induce latent tracks and damage inside a target.

HCIs on Au nano-islands and Bi nano-clusters

The measurements and results in chapter 3 have shown that the potential energy of HCIs is sufficient enough to trigger modifications in geometrically confined metallic nano-islands. This modifications manifest themselves in erosion of the metallic nano-island, by combining the nuclear stopping power, which triggers recoils and collision cascades and the potential energy, which enhances the nuclear stopping by transferring the energy from the electrons to the lattice when the metallic target is geometrically confined. Since different charge states were used, starting with Xe^{1+} up to Xe^{40+}, it was shown that the height loss is dependent on the potential energy. Kinetic energy effects can be ignored, since the Xe^{1+} irradiation did not yield a significant height loss of the Au nano-islands, whereas the Xe^{40+} yields the highest height loss of these islands with the same initial kinetic energy. An additional one-to-one evaluation of not irradiated and irradiated Au nano-islands gives a value for the volume threshold, where smaller islands are eroded more due to the potential energy of the HCI. This volume threshold was measured with AFM and is influenced by the tip radius, which was corrected with SEM measurements which are not prone to this tip artefact. In summary it can be said that potential energy effects on metallic nano-sized objects can be measured in terms of height change and also a charge state dependence was found.

For the bismuth clusters on CaF_2 and SiO_2 the results are not as promising as for the Au nano-islands. The height loss that was measured, may not describe any potential energy effect at all, but other aspects have to be considered. The density of the bismuth clusters on the CaF_2 sample was way too high and a geometric confinement was not given. The bismuth clusters on the SiO_2 sample were way too big in their lateral size to geometrical confine the potential energy of the HCI. Further measurements with samples with smaller islands are needed to observe or exclude an effect of the potential energy of the HCI and hence highlighting the possibility to erode metallic nano-clusters with HCIs.

Latent tracks of SHIs

The idea of this experiment was to visualise the latent track and the discontinuous part. Various TEM techniques were used, whereby the EELS experiment is very sensitive to differences in the optical properties of a semiconductor or insulator. The amorphization of TiO_2 extends from the surface micrometer deep into the target [12]. With EELS no differences were found, which would be associated with a transition fromn rutile to amorphous TiO_2, which also changes the refractive index of the material. The other techniques, such as cathodoluminescence, dark field imaging, STEM, HAADF, mass-to-thickness contrast and Z-contrast did also not show a discontinuous part. Although the resolution or detection limit of these techniques exceeds most methods to visualise single atoms, single atomic defects are very difficult to measure. The lamella has a thickness of 50 nm and the diameter of the track amounts to about 2 nm and the lattice constant for TiO_2 is a = b = 0.4584 nm. So, defects occupy about four lattice planes, whereas the thickness of the lamella amounts about 110 lattice planes. To detect such small differences maybe other, more precise techniques have to be used. A technique that may be sufficient enough to detect these small errors in the lattice is monochromatic EELS, that can distinguish the ZLP from the phonon spectrum and give a more exact plasmon spectrum with a energy resolution of 10 to 100 meV [38] instead of 300 meV for the Tecnai F20 TEM. Although the intended feature was not observed, the damage profile of the SHI was resolved very well. The typical conical shape was visualised with different TEM techniques and furthermore, an evaluation of the HAADF signal showed that these latent tracks are empty or voids.

Danksagung

Zum Abschluss dieser Arbeit möchte ich mich bei all jenen bedanken, die mich am Weg dieser Arbeit und dieses Studiums unterstützt haben. Ohne diese Hilfe wäre all dies nicht möglich gewesen.
Vor allem bei:
Dir lieber *Richard*. Ohne dich wäre diese Arbeit nicht entstanden. Du hast mich in diese Gruppe aufgenommen und gelehrt, wie man wissenschaftlich arbeitet, unterstützt und immer wieder Feedback gegeben wie man manches anders angehen kann und hast mich in die richtige Richtung geleitet. Auch wenn Messungen nicht funktioniert haben, es immer wieder Probleme gab, hast du lösungsorientiert mit mir gearbeitet und zum Umdenken von Problemen aufgerufen.

Auch bei dir *Gabriel* möchte ich mich herzlich bedanken. Am ersten Tag hast du mich in die Gruppe integriert, geleitet und mich ermutigt. Du hast zahlreiche Stunden geopfert um mir zu helfen, zuzuhören oder einfach zu plaudern. Vieles lief nicht so wie erwartet und auch dann hast du mich motiviert, wenn ich den Kopf in den Sand gesteckt habe. Ohne deine Unterstützung wäre vieles in dieser Arbeit nicht so gelaufen. Vor allem der sehr freundschaftliche Umgang miteinander hat mich sehr erstaunt und begeistert.

Bei dir *Fritz*, für deine angenehme aber auch professionelle Leitung der Arbeitsgruppe. Nicht nur universitär sorgst du stets für einen Zusammenhalt in der Gruppe, sondern auch mit den gemeinsamen Gruppenausflügen und anschließendem Beisammensein. In den Meetings konnte jede Fragestellung diskutiert werden, aber auch wenn mal ein dringender Rat notwendig war, konnte man den jederzeit einholen bei dir.

Und natürlich bei den Kollegen der Arbeitsgruppe *Anna*, *Matthias*, *David* (ehem.), *Christian*. Man teilte gemeinsame Freuden, Erfolge aber auch Niederlagen in einem freundschaftlichen Umfeld. Der Umgang untereinander war faszinierend für mich, ein solches Kollegium zu finden ist ein Privileg. Das gemeinsame Kreuzworträtseln zu Mittag, die Freude in den Augen wenn es Kuchen gab und die Ausflüge mit der Arbeitsgruppe zu unternehmen waren entspannend und brachten einander näher.

Auch bei den Mitarbeitern von USTEM, bei Ihnen *Hr. Stöger-Pollach*, *Sabine* und anderen. Ihr habt mich bei den Messungen tatkräftig unterstützt und durch euch habe ich meine Faszination für TEM bekommen. Für die vielen investierten Stunden zur Proben-

präparation und Messzeit am Mikroskop. Ihr wart stets sehr zuvorkommend und allzeit hilfsbereit. Vielen Dank für eure Untersützung beim Thema der SHI!

Zu guter Letzt, möchte ich mich bei meiner Familie, Freundin und Freunde bedanken. Bei meiner Mutter *Ulrike*, die mich während meines Studiums nicht nur finanziell unterstützt hat, sondern auch, dass ich nicht aufgeben soll und „durchbeißen“ soll, ganz nach dem Motto: *Augen zu und durch*.
Bei meiner Freundin *Lisa*, die im vergangen Jahr immer ein offenes Ohr hatte, wenn es mal nicht so lief. Die mich ermutigt hat, mich motiviert hat und an mich geglaubt hat auch wenn ich es nicht tat. Du hast die Zeit während des Studienabschlusses sorgenfreier gemacht und mich mit deinem Lachen und deiner Fürsorge stets liebevoll auf andere Gedanken gebracht. Du hast mich auch daran erinnert, wenn es genug war und hast mir unbewusst Ruhephasen eingebaut. Auch für meinen zukünftigen Weg hast du mich selbstbewusster gemacht und durch deinen Glauben an mich, dass ich es schaffen kann, vertraue ich nun selbst mehr darauf.
Auch bei euch *Dominic*, *Sarah*, *Hannes*, *Stefan* die mich auf andere Gedanken gebracht haben und stets für ein Gespräch offen waren, wenn alles den Bach hinunterzulaufen schien.
Abschließend auch bei dir *Ralph*. Als Klassenvorstand während der HTL-Zeit warst du ein Vorbild für uns junge Schüler. Du hast nicht nur an jeden einzelnen von uns geglaubt, du hast auch versucht, uns auf das Leben und eine Karriere vorzubereiten. Erst dir verdanke ich meinen Werdegang, da du mich damals ermutigt hast überhaupt zu studieren und einen universitären Weg zu bestreiten.

Bibliography

[1] J. W. Mayer and O. J. Marsh. "Ion Implantation in Semiconductors". In: Applied Solid State Science 1 (1969). Ed. by Raymond Wolfe. 239.

[2] U. Linz. *Ion beam therapy Fundamentals, technology, clinical applications*. Springer. Springer Berlin, Heidelberg, 2012.

[3] J.E.E. Baglin. "Ion beam nanoscale fabrication and lithography—A review". In: *Applied Surface Science* 258 (2012). 4103.

[4] L.A. Giannuzzi and F.A. Stevie. "A review of focused ion beam milling techniques for TEM specimen preparation". In: *Micron* 30 (1999). 197.

[5] R. Wilhelm, A. El-Said, F. Krok, R. Heller, E. Gruber, F. Aumayr, and S. Facsko. "Highly charged ion induced nanostructures at surfaces by strong electronic excitations". In: *Progress in Surface Science* 90 (2015). 377.

[6] A. S. El-Said, R. Heller, W. Meissl, R. Ritter, S. Facsko, C. Lemell, B. Solleder, I. C. Gebeshuber, G. Betz, M. Toulemonde, W. Möller, J. Burgdörfer, and F. Aumayr. "Creation of Nanohillocks on CaF_2 Surfaces by Single Slow Highly Charged Ions". In: *Physical Review Letter* 100 (2008). 237601.

[7] F. Aumayr, S. Facsko, A. El-Said, C. Trautmann, and M. Schleberger. "Single ion induced surface nanostructures: a comparison between slow highly charged and swift heavy ions". In: *Journal of Physics: Condensed Matter* 23.39 (2011). 393001.

[8] M. Karlušić, M. Jakšić, Henning Lebius, B. Ban-D'etat, R. Wilhelm, R. Heller, and M. Schleberger. "Swift heavy ion track formation in SrTiO 3 and TiO2 under random, channeling and near-channeling conditions". In: *Journal of Physics D: Applied Physics* 50 (2017). 205302.

[9] S. Donnelly and R. Birtcher. "Heavy ion cratering of gold". In: *Phys. Rev. B* 56 (1997). 13599.

[10] P. Satyam, J. Kamila, S. Mohapatra, B. Satpati, D. Goswami, B. Dev, R. Cook, L. Assoufid, J. Wang, and N. Mishra. "Crater formation in gold nanoislands due to MeV self-ion irradiation". In: *Journal of Applied Physics* 93 (2003). 6399.

[11] S.E. Donnelly and R. C. Birtcher. In: *Phil. Magazine A* 794 (1999). 133.

[12] P. Zhai, S. Nan, L. Xu, W. Li, Z. Li, P. Hu, J. Zeng, S. Zhang, Y. Sun, and J. Liu. "Fine structure of swift heavy ion track in rutile TiO2". In: *Nuclear Instruments and Methods in Physics Research Section B: Beam Interactions with Materials and Atoms* 457 (2019). 72.

[13] J. Biersack and L. Haggmark. "A Monte Carlo computer program for the transport of energetic ions in amorphous targets". In: *Nuclear Instruments and Methods* 174 (1980). 257.

[14] A.B. Wittkower and H.D. Betz. "Equilibrium-charge-state distributions of energetic ions (Z > 2) in gaseous and solid media". In: *Atomic Data and Nuclear Data Tables* 5 (1973). 113.

[15] W. Wesch and E. Wendler. *Ion Beam Modification of Solids*. Springer. Springer Cham, 2016.

[16] A. A. Correa. "Calculating electronic stopping power in materials from first principles". In: *Computational Materials Science* 150 (2018). 291.

[17] J. F. Ziegler, M.D. Ziegler, and J.P. Biersack. "SRIM – The stopping and range of ions in matter (2010)". In: *Nuclear Instruments and Methods in Physics Research Section B: Beam Interactions with Materials and Atoms* 268 (2010). 1818.

[18] W. Busza and A. S. Goldhaber. "Nuclear stopping power". In: *Physics Letters B* 139 (1984). 235.

[19] C. Länger, P. Ernst, M. Bender, D. Severin, C. Trautmann, M. Schleberger, and M. Dürr. "Single-ion induced surface modifications on hydrogen-covered Si(001) surfaces—significant difference between slow highly charged and swift heavy ions". In: *New Journal of Physics* 23 (2021). 093037.

[20] J. M. Pomeroy, A. C. Perrella, H. Grube, and J. D. Gillaspy. "Gold nanostructures created by highly charged ions". In: *Phys. Rev. B* 75 (2007). 241409.

[21] A. Arnau, M. Peñalba, P.M. Echenique, and F. Flores. "A charge state approach to the stopping power of ions in solids". In: *Nuclear Instruments and Methods in Physics Research Section B: Beam Interactions with Materials and Atoms* 69 (1992). 102.

[22] F. Herfurth, Z. Andelkovic, W. Barth, W. Chen, L. Dahl, S. Fedotova, P. Gerhard, M. Kaiser, O. Kester, H-J. Kluge, N. Kotovskiy, M. Maier, B. Maaß, D. Neidherr, W. Quint, U. Ratzinger, A. Reiter, A. Schempp, Th. Stöhlker, H. Vormann, G. Vorobjev, and S. Yaramyshev. "The HITRAP facility for slow highly charged ions". In: *Physica Scripta* T166 (2015). 014065.

[23] E Gruber, R Wilhelm, R Pétuya, V Smejkal, R Kozubek, A Hierzenberger, B Bayer, I Aldazabal, A Kazansky, F Libisch, A Krasheninnikov, M Schleberger, S Facsko, A Borisov, A Arnau, and F Aumayr. "Ultrafast electronic response of graphene to a strong and localized electric field". In: *Nature communications* 7 (2016). 13948.

[24] A. Niggas, S. Creutzburg, J. Schwestka, B. Wöckinger, T. Gupta, P. Grande, D. Eder, J. Marques, B. Bayer, F. Aumayr, R. Bennett, and R. Wilhelm. "Peeling graphite layer by layer reveals the charge exchange dynamics of ions inside a solid". In: *Communications Physics* 4 (2021). 180.

[25] A. S. El-Said, R. Wilhelm, R. Heller, M. Sorokin, S. Facsko, and F. Aumayr. "Tuning the Fabrication of Nanostructures by Low-Energy Highly Charged Ions". In: *Phys. Rev. Lett.* 117 (2016). 126101.

[26] M. Toulemonde, E. Paumier, and C. Dufour. "Thermal spike model in the electronic stopping power regime". In: *Radiation Effects and Defects in Solids* 126 (1993). 201.

[27] B. Bhushan. "Springer Handbook of Nanotechnology". In: *Springer-Verlag Berlin Heidelberg* (2010). 1964.

[28] P. Eaton and P. West. *Atomic Force Microscopy*. OUP Oxford, 2010.

[29] Olympus. *240AC-NA*. URL: `https://www.opustips.com/en/AFM-Tip-240AC-NA.html`. (accessed: 03.10.2022).

[30] Nanosensors. *SSS-FM*. URL: `https://www.nanosensors.com/supersharpsilicon-force-modulation-mode-afm-tip-SSS-FM`. (accessed: 03.10.2022).

[31] Dreebit. *Ionization Energy Database*. URL: `https://www.dreebit-ibt.com/ionization-energy-database.html`. (accessed: 08.09.2022).

[32] K.D. Vernon-Parry. "Scanning electron microscopy: an introduction". In: *III-Vs Review* 13 (2000). 40.

[33] H. Seiler. "Secondary electron emission in the scanning electron microscope". In: *Journal of Applied Physics* 54 (1983). R18.

[34] G. E. Lloyd. "Atomic number and crystallographic contrast images with the SEM: a review of backscattered electron techniques". In: *Mineralogical Magazine* 51.359 (1987). 3.

[35] C. Hetherington. "Aberration correction for TEM". In: *Materials Today* 7 (2004). 50.

[36] C.Y. Tang and Z. Yang. "Chapter 8 - Transmission Electron Microscopy (TEM)". In: (2017). Ed. by N. Hilal, A. F. Ismail, T. Matsuura, and D. Oatley-Radcliffe. 145.

[37] Ernst Ruska-Centre for Microscopy and Spectroscopy with Electrons. "FEI Tecnai G2 F20". In: *Journal of large-scale research facilities* 2 (2016).

[38] C. B. Carter D. B. Williams. "Transmission Electron Microscopy". In: *Springer-Verlag* (2009).

[39] U. Diebold. "The surface science of titanium dioxide". In: *Surface Science Reports* 48 (2003). 53.

[40] A. George, C. Neumann, D. Kaiser, R. Mupparapu, T.r Lehnert, U. Hübner, Z. Tang, A. Winter, U. Kaiser, I. Staude, and A. Turchanin. "Controlled growth of transition metal dichalcogenide monolayers using Knudsen-type effusion cells for the precursors". In: *Journal of Physics: Materials* 2 (2019). 016001.

[41] F. Trillitzsch, R. Guerra, A. Janas, N. Manini, F. Krok, and E. Gnecco. "Directional and angular locking in the driven motion of Au islands on MoS_2". In: *Phys. Rev. B* 98 (2018). 165417.

[42] A. Mauracher, O. Echt, A.M. Ellis, S. Yang, D.K. Bohme, J. Postler, A. Kaiser, S. Denifl, and P. Scheier. "Cold physics and chemistry: Collisions, ionization and reactions inside helium nanodroplets close to zero K". In: *Physics Reports* 751 (2018). 1.

[43] Y. Takahashi, K. Sano, T. Kinoshita, and T. Yabuzaki. "Spectroscopy of alkali atoms and molecules in superfluid helium". In: *Phys. Rev. Lett.* 71 (1993). 1035.

[44] P. Martini, S. Albertini, F. Laimer, M. Meyer, M. Gatchell, O. Echt, F. Zappa, and P. Scheier. "Splashing of Large Helium Nanodroplets upon Surface Collisions". In: *Phys. Rev. Lett.* 127 (2021). 263401.

[45] M C Strus, A Raman, C-S Han, and C V Nguyen. "Imaging artefacts in atomic force microscopy with carbon nanotube tips". In: *Nanotechnology* 16 (2005). 2482.

[46] D. Nečas and P. Klapetek. "Gwyddion: an open-source software for SPM data analysis". In: *Central European Journal of Physics* 10 (2012). 181.

[47] G. Szabo. *Heavy ion cluster interaction with CaF2 and slow highly charged ion interaction with metallic nano-islands.*

[48] R. Wilhelm and W. Möller. "Charge-state-dependent energy loss of slow ions. II. Statistical atom model". In: *Phys. Rev. A* 93 (2016). 052709.